

AD-A177 654

AIR FORCE INSTITUTE OF TECHNOLOGY



AIR UNIVERSITY
UNITED STATES AIR FORCE

SPECTRAL METHODS FOR GLOBAL ATMOSPHERIC FLOW
APPLIED TO THE MODIFIED AFIT FALLOUT PREDICTION MODEL

THESIS

Darrell Palmer

First Lieutenant, USAF

AFIT/GNE/PH/86-14

DTIC FILE COPY

SCHOOL OF ENGINEERING

DTIC
ELECTE

MAR 13 1987

WRIGHT-PATTERSON AIR FORCE BASE, OHIO

This document has been approved
for public release and sales
distribution is unlimited.

87 3 12 080



SPECTRAL METHODS FOR GLOBAL ATMOSPHERIC FLOW
APPLIED TO THE MODIFIED AFIT FALLOUT PREDICTION MODEL

THESIS

Darrell Palmer
First Lieutenant, USAF
AFIT/GNE/PH/86-14

Distribution Statement A is correct for
this report. It has been published in open
literature: Journal of Geophysical Research,
Volume 90, No. D6, Oct. 1985
Per Mr. Charles J. Bridgman, AFIT/ENP,
Thesis Chairman

Accession For	
NTIS GRA&I	<input checked="" type="checkbox"/>
DTIC TAB	<input type="checkbox"/>
Unannounced	<input type="checkbox"/>
Justification	
By	
Distribution/	
Availability Codes	
Dist	Avail and/or Special
A-1	

AFIT/GNE/PH/86-14

SPECTRAL METHODS FOR GLOBAL ATMOSPHERIC FLOW
APPLIED TO THE MODIFIED AFIT FALLOUT PREDICTION MODEL

THESIS

Presented to the Faculty of the School of Engineering
of the Air Force Institute of Technology
Air University
In Partial Fulfillment of the
Requirements for the Degree of
Master of Science

by

Darrell Palmer, B.S.
First Lieutenant, USAF

October 1986

Approved for public release; distribution unlimited

Preface

This study originated when Major Tom Hopkins (my acting branch chief) brought his dissertation research model to this office, ASD/ENSSS, where he was permanently assigned after receiving his Ph.D. in Nuclear Engineering from AFIT. A request from the B-1B Program Office tasked our office to investigate the survivability (through mission completion) of fleet aircraft flying through radioactive dust clouds generated by a massive nuclear strike from U. S. weapons over the threat area. This essentially requires defining the free-field environment (due to fratricide) resulting from the threat of nuclear generated dust clouds. In the attempt to perform this analysis, different stages of development and validation to the research model are being made. One such validation compares predicted particle transport of a non-nuclear generated dust cloud to actual experimental data. I incorporated the joint research Hopkins and I made (on the job) of the non-nuclear validation to the research model into this thesis.

I would like to thank Tom Hopkins for his continued advice and expertise as my branch chief and comrade. Particular thanks to Professor Charles J. Bridgman, my thesis advisor, for his prolonged guidance in technical and personal areas throughout my thesis. Thanks to my co-workers Jeff Brown and Chris Zimmerman for their help in the validation. Finally, thank you to Kathy, Antony and Angelo who have endured my 2-1/2 year short tour at AFIT as a part-time student.

Table of Contents

	Page
Preface	ii
List of Figures	v
List of Tables	vii
Abstract	viii
I. Introduction	1
Fallout Models	1
Input Winds	2
Output Spectral Winds	3
Background	3
Organization of Report	5
II. Spectral Methods for Atmospheric Modeling	7
Modeling Equations	7
Equations of Motion in Spectral Form	9
Summary	22
III. Hotline Locator Model	23
Particle Size Distribution	25
Initial Stabilized Cloud	26
Layered Atmosphere	29
Fall Mechanics in a Layered Atmosphere	31
Wind Shear	36
Spatial Distribution of Stabilized Cloud	37
Cloud Deviations	43
Summary	44
IV. Validation	45
Direct Course HE Test	45
Test Description	45
Direct Course Test Results	48
Particle Size Spectrometers	52
AFGL Validation	55
Spectral Winds	56
Initial Particle Size and Filter Analysis	61
Direct Course HE Cloud Analysis	64
Pancake Cloud	64
Lateral Expansion	65
Mass Fraction Distribution	67
Results	69
Statistical Comparison	70

Discussion and Summary	72
V. Summary, Conclusions and Recommendations	96
Spectral Coefficient Wind Generator.....	96
Particle Transport Using Spectral Winds in a Hotline Locator Model	96
Direct Course Analysis	97
Recommendation	97
Appendix A: AFGL Model	99
Appendix B: Fast Fourier Transforms	105
Appendix C: Direct Course Mass Fraction	107
Appendix D: User's Guide for AFGL	112
Bibliography	113
Vita	116

List of Figures

Figure	Page
II-1 Spectral Heights	12
II-2 Spectral Rhomboidal Truncation	13
II-3 Gaussian Grid	18
III-1 Freeze Frame Cloud Axis	24
III-2 Linear Average Wafer Center Heights for Delfic Initial Particle Sizes	28
III-3 Model Spectral Height Comparisons	30
III-4 Height Versus Particle Fall Time	35
III-5 Three-Dimensional Gaussian Cloud Model	40
III-6 Unexpanded Gaussian Quadrant	41
III-7 Fully Expanded Three Dimensional Gaussian Cloud	42
IV-1 Direct Course Tower	47
IV-2 Direct Course Cloud Width Measurements	51
IV-3 Interpolated Direct Course Wind Field (1000 mb)	57
IV-4 Interpolated Direct Course Wind Field (850 mb)	58
IV-5 Interpolated Direct Course Wind Field (700 mb)	59
IV-6 Interpolated Direct Course Wind Field (500 mb)	60
IV-7 Linear Regression to Direct Course Cloud Width Measurements	66
IV-8 Mass Histogram Comparison (Pass 7)	74
IV-9 Mass Histogram Comparison (Pass 8)	75
IV-10 Mass Histogram Comparison (Pass 9)	76
IV-11 Mass Histogram Comparison (Pass 10)	77
IV-12 Mass Histogram Comparison (Pass 11)	78
IV-13 Mass Histogram Comparison (Pass 12)	79

List of Figures (continued)

Figure	Page
IV-14 Mass Histogram Comparison (Pass 13)	80
IV-15 Mass Histogram Comparison (Pass 14)	81
IV-16 Mass Histogram Comparison (Pass 15)	82
IV-17 Mass Histogram Comparison (Pass 16)	83
IV-18 Mass Histogram Comparison (Pass 17)	84
IV-19 Mass Histogram Comparison (Pass 18)	85
IV-20 Mass Histogram Comparison (Pass 19)	86
IV-21 Mass Histogram Comparison (Pass 20)	87
IV-22 Mass Histogram Comparison (Pass 21)	88
IV-23 Mass Histogram Comparison (Pass 22)	89
IV-24 Mass Histogram Comparison (Pass 23)	90
IV-25 Mass Histogram Comparison (Pass 24)	91
IV-26 Mass Histogram Comparison (Pass 25)	92
IV-27 Mass Histogram Comparison (Pass 26)	93
IV-28 Mass Histogram Comparison (Pass 27)	94
IV-29 Direct Course Cloud Center Comparison	95
C-1 Direct Course Mass Fraction Distribution	110

List of Tables

Table	Page
II-1 Gauss-Legendre Weights and Angles	19
IV-1 Direct Course Cloud Measurements	49
IV-2 Direct Course Accumulated Mass Summary	50
IV-3 Direct Course Aircraft Parameters	52
IV-4 OAP-2D-C Micron Channel Ranges	53
IV-5 FSSP Micron Channel Ranges	54
IV-6 Direct Course Initial Particle Sizes	62
IV-7 Fractional Errors of Direct Course Mass Histograms	71
IV-8 Absolute Errors of Direct Course Center Axis	72
C-1 Direct Course Mass Fraction per Particle Size	111

ABSTRACT

This investigation predicted the airborne spatial distribution of a high explosive generated dust cloud. A comparison of predicted cloud center positions to experimental data collected from an aircraft flying through the dust cloud center at various times and altitudes was also studied.

The analysis was accomplished using a model received from the Air Force Geophysics Laboratory (model called AFGL) which produces global complex spectral coefficients. Spectral coefficients were applied as inputs into a modified AFTT fallout prediction model (called REDRAM) to predict dust mass/m³ of air per μm of dust diameter which resulted from a single continuous horizontal pass through the cloud at a fixed time and altitude. The results validated the spectral wind fallout model by showing general agreement of predicted values to that of experimental results. The significance of the validation shows that spectral methods can realistically predict particle transport using a spectral wind fallout model.

SPECTRAL METHODS FOR GLOBAL ATMOSPHERIC FLOW
APPLIED TO THE MODIFIED AFIT FALLOUT PREDICTION MODEL

I. Introduction

Fallout Models

When a nuclear bomb is detonated in the atmosphere, a vaporous mixture of radioactive materials forms. This mixture contains vaporized dirt and debris that is drawn into the rising fireball, along with radioactive fission fragments, decay products and unfissioned bomb fuel. As the vapors condense, solid particles form a nuclear cloud. The cloud cools and becomes stable, thereby causing the radioactive particles to fall from the cloud. During their fall, the particles are transported by ambient winds, thus allowing radioactive fallout to land away from the detonation point.

Two general classes of fallout codes are used to predict radioactive fallout from nuclear bursts. Discrete codes, such as DELFIC, the Defense Land Fallout Interpretive Code (24), represent fallout particles from the initial stabilized cloud as discrete monosized groups which are modeled as a series of discrete vertical wafers within the initial stabilized cloud. Fallout is computed by tracking each wafer as it falls and is transported through the atmosphere to the ground. This model can use three-dimensional multiple windfield profiles to predict particle transport as the wafers descend. Smearing codes, such as WSEG, Weapon Systems Evaluation Group (26) or the AFIT code, smear or deposit fallout footprints by using analytic solutions to equations that approximate cloud dynamics. The WSEG model fails to account for fractionation, variations in activity particle-size distributions, realistic settling rates and varying winds.

The AFIT fallout prediction model (7) is also a smearing code, but unlike WSEG, accounts for variation in activity size, fractionation, and uses realistic settling rates.

However, this model is limited to a constant wind assumption that transports airborne particles.

Hopkins (16) modified the AFIT model to calculate fallout footprints using both volumetric cells and smearing techniques. His model REDRAM tracks particle size histories in a discretized atmosphere as functions of space and time. REDRAM uses an empirical relation derived from the Cloud Rise Module in DELFIC to predict the initial stabilized distribution (16). Spectral coefficients from a global wind interpolator model AFGL and McDonald-Davies fall mechanics are used to predict the hotline (points of peak activity downwind from the burst) on the ground from particle transport of the initial, stabilized cloud. These grounded particles are used in another code Hopkins wrote (SMRSHR) which analytically smears the activity along the hotline to compute dose rate contours.

Hopkins' codes have significant advantages over DELFIC in that they are simple to use, they have fast run times, and they use spectral winds. Thus, REDRAM provides an inexpensive method for accurately predicting hotline locations anywhere on the globe at large distances from the burst. It is especially more accurate than constant wind codes because it uses variable winds to realistically predict particle transport.

Input Winds

The variable winds derived in REDRAM are produced from input winds which are used in a spectral coefficient generator model AFGL. These input winds are observed twice daily by atmospheric probes (radiosondes or rawinsondes) that are released at midnight and/or midday Greenwich Mean Time (GMT) from about 1,415 stations around the world. Balloons, which carry temperature, humidity, and pressure sensors (at various pressure levels), are tracked by radar or radio direction finding devices, and their lateral displacement by the wind is measured and recorded. Data from each station is communicated to a data network, usually by teletype, then to a central collecting station,

and rebroadcast on international communication networks. The National Meteorological Center (NMC) receives this data and treats it for application to their numerical weather forecasting models.

Output Spectral Winds

Relevant subroutines were extracted from a large forecasting model used at the Air Force Geophysics Laboratory, Hanscom Air Force Base. These subroutines were merged into a model called AFGL which interpolates inputted global gridded wind data in spherical coordinates using fast Fourier transforms in longitude and Gauss-Legendre quadrature in latitude to produce complex spectral coefficients. The coefficients are used in the truncated spherical harmonic expansions to compute variable winds (called spectral winds) anywhere in the atmosphere.

Background

In the past, numerical solutions to a full set of meteorological equations, or "primitive" (13) equations, were used in numerical modeling of the large-scale atmospheric flow. These solutions were too complex to perform routinely so different numerical schemes were employed for atmospheric modeling.

In any numerical integration of the hydrodynamic equations governing atmospheric fluid flow, predictions of certain time-dependent scalar or vector fields are required. The mathematical procedure which is used for this purpose is affected by the manner in which these fields are represented numerically. The fields may be represented as discrete functions on a mesh which covers the physical space of a desired problem, or the fields may be represented by coefficients of an expansion in orthogonal functions. In the latter case, the field representation is in the "expansion coefficient domain" (referred to as spectral domain). The spectral domain can be thought of as representing "spectrally," the expansion coefficients for the transport fields of planetary motion in "wave-number space."

Merilees (21) showed that the hydrodynamical equations could be transformed explicitly into the spectral domain in terms of spherical harmonics. Although spectral methods (field expansion coefficients in orthogonal functions) offered several advantages for use in meteorological predictions, they still proved too costly to use on an operational basis. Flattery (13) used Hough functions (the eigenfunctions of Laplace's tidal equation) to make spectral predictions practical by using a simplified version of the primitive equations. This simplified version of equations governs the linear behavior of the atmosphere (which is in a basic state of rest). By doing this, Flattery showed that Hough functions could be used to predict spectral meteorological analysis directly from observed data.

Robert (28) used the observed data of a series of 500-mb. charts, covering both hemispheres, to provide the initial conditions for a spectral barotropic model. This spectral model used functions equivalent to spherical harmonics, with the stream field represented by a truncated series.

Robert's model consisted of 500-mb. global analyses of the geopotential as input. The stream functions were generated from a linear balance equation. Merilees (21) used the linear balance equation to convert the spectral versions of the geopotential into equivalent stream functions. Forecasts of the stream functions were then prepared using a barotropic model developed by Bolin (4) and Cressman (8). Finally, the linear balance equation was inverted to produce a forecast of the geopotential.

The results of Robert's model produced reasonably good global forecasts. These results left little doubt as to the future of atmospheric spectral type simulations compared with the existing classical models (6) that represented the hydrodynamic meteorological variables in space and time on a finite difference grid.

Orszag (25) used a transform method developed for the fast calculation of vector-coupled sums appearing in the spectrally truncated vorticity equation. The method involved

expansions in surface spherical harmonics. This method succeeded because it was much faster to transform the spectral representation to physical space, multiply the physical-spaced functions, and inverse transform back to the spectral representation, than to evaluate the vector-coupled sums directly in spectral form.

Sela (31) used the transform method of Orszag to represent all prognostic variables by a spherical harmonic series. He applied his model so that variable resolutions were easily achieved, while still producing an efficient code. He accomplished this by assigning all variables pertaining to resolution symbolic characters that were easily replaced by specific values. The resulting codes, together with specialized fast Fourier transform routines produced competitive time integrations (compared to the classical finite difference method).

Selas' model represents the bulk of a model received from the Air Force Geophysics Laboratory (named AFGL) and is used extensively here as a technical reference for the AFGL model.

In summary AFGL inputs the measured winds at irregular discrete locations and outputs the spectral coefficients necessary to predict the variable winds at any arbitrary space point in the atmosphere.

This report investigates the use of these spectral coefficients when applied to a fallout model to predict the airborne spatial distribution of a high explosive generated dust cloud. Predicted values are then compared to experimental observations. The agreement between the predictions and the measurements is considered to be a validation of the spectral wind transport method.

Organization of Report

Chapter II describes modeling equations to AFGL and how spectral coefficients are derived. The hotline locator model that derives spectral winds to transport particles from the initial, stabilized cloud is presented in Chapter III. Chapter IV shows results of a

validation analysis using data from a non-nuclear high explosives test at White Sands Missile Range (code name Direct Course).

Appendix A explains the subroutines of AFGL and what they do. Appendix B presents Fast Fourier Transform methods used as subroutines in AFGL to compute spectral-to-physical domain calculations. Appendix C describes how the mass fraction per particle size was obtained for Direct Course. A Users' Guide to AFGL is contained in Appendix D.

II. Modeling Equations

The method of spectral representation consists of expanding the hydrodynamical variables of a particular model in terms of a set of orthogonal functions of the spatial coordinates. The model equations then transform into an infinite set of ordinary differential equations in which the independent variable is time and the dependent variables are the coefficients of the components in the expansions.

In this model, the equations will be considered in their derived form. The two equations of motion considered are the vorticity and the divergence equations.

Vorticity is a measure of the rotational flow of air in the earth's atmosphere. In order to understand this quantity, it is necessary to think of the atmosphere vertically and to consider what happens in a region where the air flows together (converges) at a level near the ground, then rises as a consequence of the convergence and spreads out (diverges) at some higher level, usually in the upper troposphere; that is, eight to 10 kilometers above ground.

The air that is converging near the ground is rotating with the earth, as is the rest of the atmosphere; but as it is drawn inward into a smaller area during the convergence, its rate of rotation will increase in a way similar to that in which the rate of rotation of a weight twirled on the end of a string increases as the string is pulled in and the angular momentum of the weight is converged. The region of convergence thus appears as an area of increased rotation of the winds. This increase in the rotation is the same as the rotation of the earth, counterclockwise in the Northern Hemisphere and clockwise in the Southern Hemisphere.

By Helmholtz' theorem any horizontal wind field may be represented as the sum of a rotational field and a divergent field as (15):

$$\underline{V} = \underline{V}_\psi + \underline{V}_\chi \quad \underline{V}_\psi = \hat{k} \times \nabla\psi \quad \underline{V}_\chi = \nabla\chi \quad (2.1)$$

where

ψ = The scalar stream function for the rotational part of the wind

χ = The scalar velocity potential for the divergent part of the wind

\hat{k} = The vertical unit vector

∇ = The horizontal gradient operator

From these definitions it follows that the vertical nonlinear component of relative vorticity, ζ , and the horizontal nonlinear divergence, D , are given by (15):

$$\zeta = \hat{k} \cdot \nabla \times \underline{V} = \nabla^2 \psi \quad \text{and} \quad D = \nabla \cdot \underline{V} = \nabla^2 \chi \quad (2.2)$$

where ∇^2 is the Laplacian operator

Robert (27) noted that the components u and v of the wind field constitute pseudo-scalar fields on the globe, and were not well suited to the scalar spectral expansions. He suggested the variables

$$U = u \sin \theta \quad \text{and} \quad V = v \sin \theta \quad (2.3)$$

would be more appropriate for global spectral representation, where θ denotes colatitude and u and v denote the zonal (west-east) and meridional (south-north) velocity components.

Then Eq. (2.1) can be rewritten as:

$$\underline{V} = \hat{k} \times \nabla\psi + \nabla\chi = (U/\sin \theta) \hat{i} + (V/\sin \theta) \hat{j} \quad (2.4)$$

where \hat{i} and \hat{j} are the horizontal unit vectors.

The two U, V components of Eq. (2.4) become (5)

$$U = -\frac{\sin \theta}{a} \frac{\partial \psi}{\partial \theta} + \frac{1}{a} \frac{\partial \chi}{\partial \lambda} \quad (2.5)$$

$$V = \frac{1}{a} \frac{\partial \psi}{\partial \lambda} + \frac{\sin \theta}{a} \frac{\partial \chi}{\partial \theta}$$

where λ is longitude and a is the earth's radius.

The linear equations (2.5) provide specification of the diagnostic quantities U and V in terms of the prognostic variables ψ and χ . In this way all of the hydrodynamical variables are true scalars and thus can be expanded in terms of spherical harmonics.

Equations of Motion in Spectral Form

Consider scalar functions of position on a sphere, expressed as truncated spherical harmonic expansions. The normalized associated Legendre polynomials can be defined by (3):

$$P_n^m(\mu) = \frac{(-1)^{n+m}}{2^n n!} \left[\frac{(2n+1)(n-m)!}{2(n+m)!} \right]^{1/2} (1-\mu^2)^{m/2} \frac{d^{m+n}}{d\mu^{m+n}} (1-\mu^2)^n \quad (2.6)$$

where $\mu = \cos \theta$ and $\theta = \text{colatitude}$ ($0 \leq \theta \leq \pi$)

The normalization of Eq. (2.6) is

$$\int_{-1}^1 P_n^m(\mu) P_k^m(\mu) d\mu = \delta_{n,k} \quad (2.7)$$

Here m and n are the order and degree of the normalized associated Legendre polynomial, respectively. The generation of numerical values for P_n^m is based on the recursion relation

(3)

$$P_n^m(\mu) = 2 a_n^m \mu P_{n-1}^m(\mu) - b_n^m P_{n-2}^m(\mu) \quad (2.8)$$

where

$$a_n^m = (1/2) \left(\frac{4n^2 - 1}{n^2 - m^2} \right)^{1/2} \quad \text{and} \quad b_n^m = \frac{(2n+1)(n-m-1)(n+m-1)}{(2n-3)(n-m)(n+m)}$$

Factoring $2a_n^m$ from both terms on the right side of (2.8) gives the following (17):

$$P_n^m(\mu) = \frac{\mu P_{n-1}^m - \epsilon_{n-1}^m P_{n-2}^m}{\epsilon_n^m} \quad (2.9)$$

$$\text{where } \epsilon_n^m = \left(\frac{n^2 - m^2}{4n^2 - 1} \right)^{1/2} \quad (2.9a)$$

Defining a surface spherical harmonic as (32)

$$Y_n^m(\theta, \lambda) = P_n^m(\cos \theta) e^{im\lambda} \quad (2.10)$$

where i is the imaginary unit $\sqrt{-1}$, it follows that

$$\int_S Y_n^m (Y_n^m)^* ds = \begin{cases} 2\pi, & n = m \\ 0, & n \neq m \end{cases} \quad (2.11)$$

where S is the surface of the unit sphere and the asterisk denotes complex conjugation.

The prognostic variables are represented at discrete spectral levels in the vertical as shown in Figure II-1. At each discrete full level (for a given date and time), rhomboidal truncated expansions in terms of the spherical harmonics Y_n^m for the prognostic variables are given as follows (15):

$$\{ \psi, \chi \} = a^2 \sum_{m=-J}^J \sum_{n=|m|}^{|m|+J} \{ \psi_n^m, \chi_n^m \} Y_n^m \quad (2.12)$$

where ψ_n^m and χ_n^m are complex expansion coefficients. A rhomboidal truncation limit J is here taken as 30. This results in the ordinal wave number n and the zonal wave number m truncation scheme shown in Figure III-2. This truncation scheme defines the wave numbers associated with the truncated spherical harmonic series expansion of equation (2.12).

Diagnostic variables are based on Eqs. (2.12) and (2.5) and it is noted that the pseudo-velocity must be truncated such that (17)

$$\{ U, V \} = a \sum_{m=-J}^J \sum_{n=|m|}^{|m|+J+1} \{ U_n^m, V_n^m \} Y_n^m \quad (2.13)$$

where U_n^m and V_n^m are the desired complex spectral coefficients. The truncation limit in Eq. (2.13) is required in order to make U, V computations compatible with the truncation scheme defining the vorticity and divergence series of Eq. (2.12).

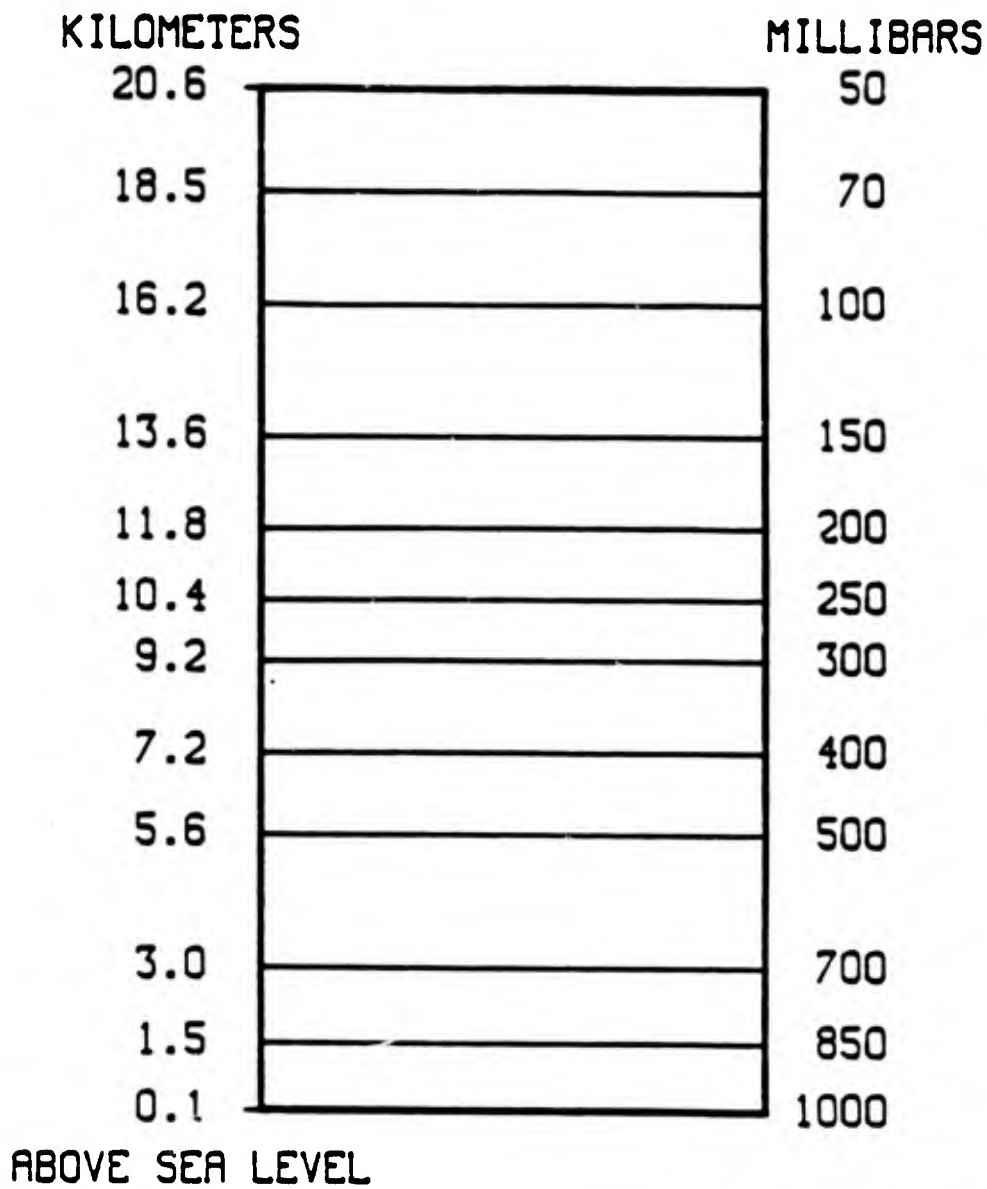


Figure II-1: Spectral levels used in AFGL Model (17:8)

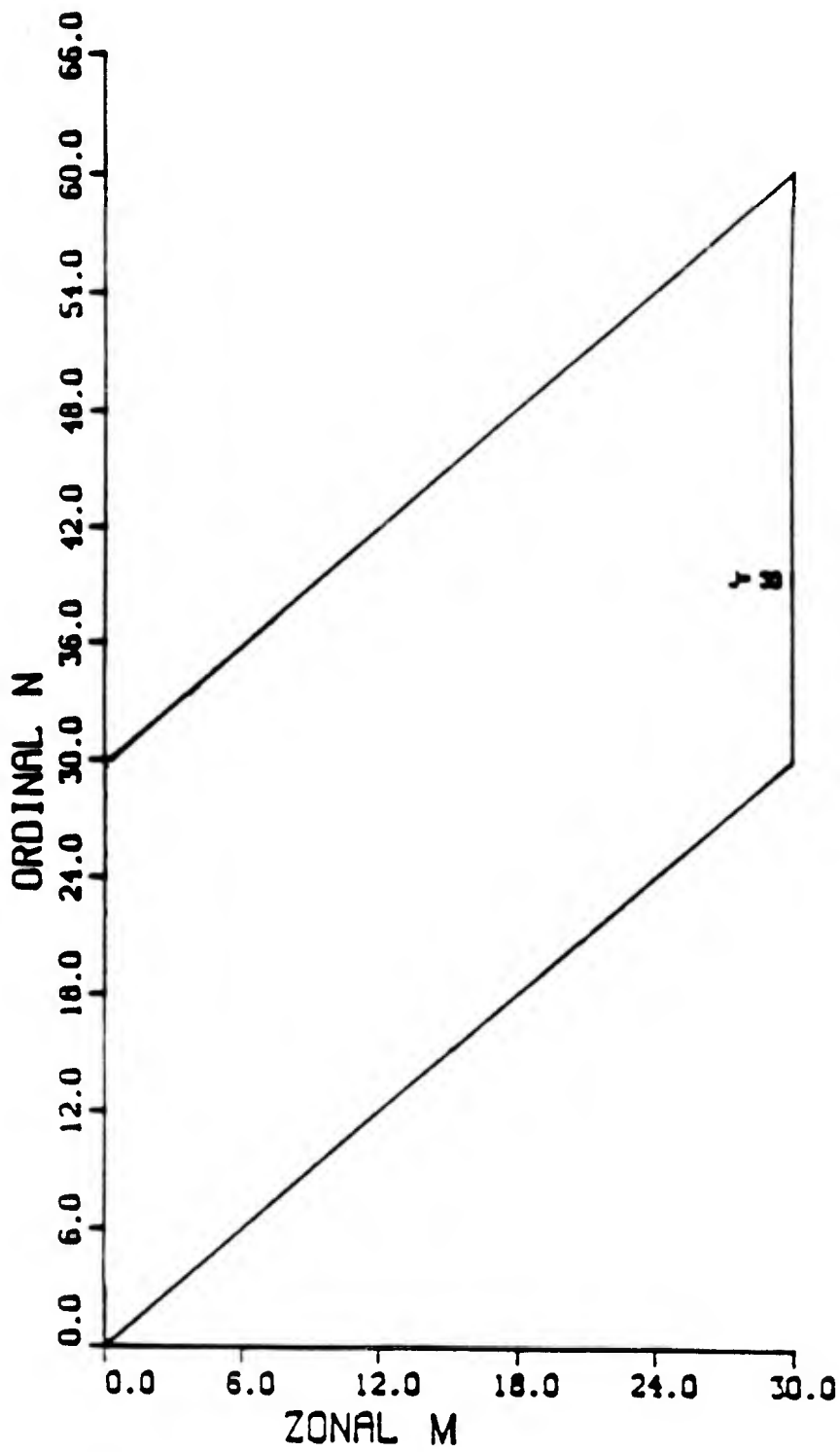


Figure II-2. Spectral domain using a rhomboidal truncation.

The criterion for truncating (2.13) in terms of the Legendre functions may be specified by any two of the three scalar indices m , n , and $n-m$. The order m is a zonal (latitudinal) wave number, and $(n-m)$ denotes a meridional wave number. Spherical harmonic expansions of geophysical variables used in AFGL uses the rhomboidal truncation criterion (12)

$$0 \leq m, n-m \leq r \quad (2.13a)$$

where r is an arbitrary integer.

The vector $\gamma \equiv m, n$ formed from the scalar indices of the function P_n^m may be regarded as a radius vector in the m, n -plane, which terminates at one of the infinite number of integral lattice points in this plane (1). It is convenient to refer to the "parity" of a wave vector $\gamma \equiv m, n$ as the parity of the sum of the components of the vector; thus, γ will be said to have even or odd parity if $m_{\max} + n$ is even or odd (where m_{\max} is the maximum zonal wavenumber value for the rhomboidal scheme) (2). If γ has odd parity, $P_\gamma(\mu)$ is an odd function of $\mu = \cos \theta$, so the vorticity and stream function must be antisymmetric with respect to the equator. Conversely, if γ has even parity, $P_\gamma(\mu)$ is an even function so the vorticity and stream function must be symmetric with respect to the equator.

Substitution of expansions (2.12) and (2.13) into Eq. (2.5) yields, on application of a standard recurrence equation and the orthogonality property of the spherical harmonics, the relationships (15)

$$U_n^m = (n-1) \epsilon_n^m \psi_{n-1}^m - (n+2) \epsilon_{n+1}^m \psi_{n+1}^m + im \chi_n^m \quad (2.14)$$

$$V_n^m = -(n-1) \epsilon_n^m \chi_{n-1}^m + (n+2) \epsilon_{n+1}^m \chi_{n+1}^m + im \psi_n^m$$

Note from (2.14) that the expansions of U and V are truncated at $n = |m| + J + 1$, one degree above the expansions for ψ and χ , thereby yielding equivalence of representation between $\{\psi, \chi\}$ and $\{U, V\}$.

To obtain the equations in spectral form, let the functions defined by (2.13) be given, and let it be required to compute its expansion coefficients $\{U_n^m, V_n^m\}$. Multiplying (2.13) by $(Y_n^m)^*$, integrating over S , and using the orthogonality condition (2.11), yields the Legendre transform (32)

$$\{U_n^m, V_n^m\} = \frac{1}{2\pi} \int_S \{U(\theta, \lambda), V(\theta, \lambda)\} (Y_n^m)^* ds \quad (2.15)$$

where $(Y_n^m)^*$ = the complex conjugate of the surface spherical harmonic (Eq. (2.10))

equal to $P_n^m(\cos \theta) e^{-im\lambda}$

and $ds = \sin \theta d\theta d\lambda$ ($0 \leq \theta \leq \pi$, $0 \leq \lambda \leq 2\pi$)

Then (2.15) becomes

$$\{U_n^m, V_n^m\} = \frac{1}{2\pi} \int_0^{2\pi} \int_0^\pi \{U(\theta, \lambda), V(\theta, \lambda)\} P_n^m(\cos \theta) e^{-im\lambda} \sin \theta d\theta d\lambda \quad (2.16)$$

for all (m, n) .

The numerical evaluation of the integrals in (2.16) proceeds in two steps. First, define the Fourier coefficients at a given colatitude as (32)

$$\{U^m(\theta), V^m(\theta)\} = \frac{1}{2\pi} \int_0^{2\pi} \{U(\theta, \lambda), V(\theta, \lambda)\} e^{-im\lambda} d\lambda \quad (2.17)$$

and compute them using a Fast Fourier Transform (FFT). See Appendix B for FFT methods. Next, the Legendre integrals in colatitude are evaluated by a Gauss-Legendre (G-L) quadrature. If $y=y(\mu)$ is a polynomial of degree not exceeding $2q-1$, then (32)

$$\int_0^{\pi} y(\theta) \sin \theta \, d\theta = \int_{-1}^1 y(\mu) \, d\mu \approx \sum_{k=1}^q GW_k y(\mu_k) \quad (2.18)$$

where the colatitude circles θ_k (or μ_k) are chosen symmetric to the equator and specified as the roots of (12)

$$P_q(\mu_k) = 0 \quad (2.19)$$

and where $P_q(\mu_k)$ are the values of the ordinary Legendre polynomials.

The G-L weights, GW_k , retrieve the orthogonality of the Legendre functions of the same rank over the set of discrete points μ_k given by (11)

$$GW_k = \frac{2 \sin^2(\mu_k)}{q^2 [P_q'(\mu_k)]^2} \quad (2.20)$$

Plugging (2.17) into (2.16), and application of (2.18) results in a G-L integration method to accurately compute (2.16) as (32)

$$\{U_n^m, V_n^m\} = \int_{-1}^1 \{U^m(\mu), V^m(\mu)\} P_n^m(\mu) \, d\mu = \sum_{k=1}^q \{U^m(\mu_k), V^m(\mu_k)\} P_n^m(\mu_k) GW_k \quad (2.21)$$

In order to solve (2.21) (based on a rhomboidal truncation parameter $J=30$), q must be at least 72 points in latitude (12). This fixes the latitudinal spacing of the Gaussian grid at 2 1/2 degrees of latitude. Equivalent longitude spacings require 144 points, for a total grid consisting of 10,368 points beginning at Greenwich and 88°46'N and is

completed by incrementing first longitude to the east and then colatitude to the south. The latitude lines are chosen to avoid the poles and the equator, where data values are independent of longitude (12). Figure II-3 depicts the Gaussian grid defined for the integrations and Table II-1 displays the G-L colatitudes and weights in the Northern Hemisphere for the J=30 case.

THE GAUSSIAN GRID

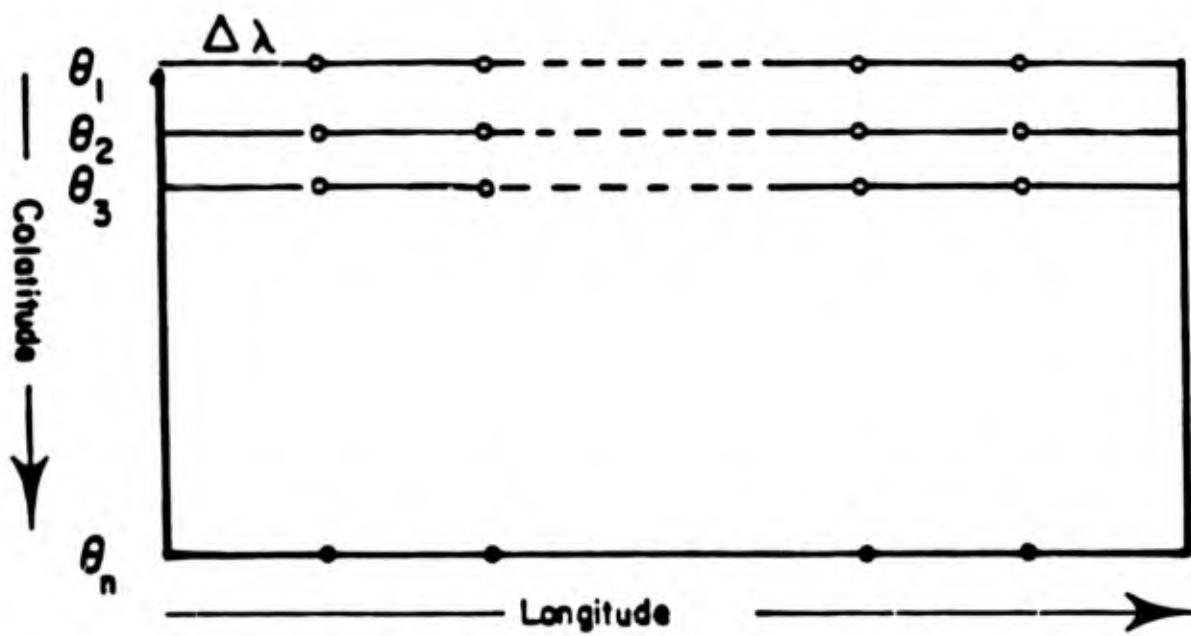


Figure II-3 (32)

Table II-1

Gauss-Legendre Angles and Weights for the Northern Hemisphere

Using a Rhomboidal Truncation of $J=30$

<u>k</u>	<u>Colatitude (degrees)</u>	<u>GW_k</u>
1	1.90	.141151639418E-02
2	4.36	.328316977480E-02
3	6.84	.515143602069E-02
4	9.32	.701027232224E-02
5	11.80	.885599607528E-02
6	14.28	.106851081660E-01
7	16.76	.124941656217E-01
8	19.25	.142797690553E-01
9	21.73	.160385649505E-01
10	24.21	.177672507917E-01
11	26.69	.194625808662E-01
12	29.17	.211213722185E-01
13	31.66	.227405105577E-01
14	34.14	.243169560658E-01
15	36.62	.258477491021E-01
16	39.11	.273300157391E-01
17	41.59	.287609731654E-01
18	44.07	.301379348962E-01
19	46.55	.314583158246E-01
20	49.04	.327196370650E-01
21	51.52	.339195306187E-01
22	54.00	.350557438084E-01
23	56.48	.361261435087E-01
24	58.97	.371287201554E-01
25	61.45	.380615915146E-01
26	63.93	.389230062175E-01
27	66.41	.397113470457E-01
28	68.90	.404251339720E-01
29	71.38	.410630269371E-01
30	73.86	.416238283607E-01
31	76.35	.421064853977E-01
32	78.83	.425100919104E-01
33	81.31	.428338901684E-01
34	83.79	.430772722750E-01
35	86.28	.432397813053E-01
36	88.76	.433211121656E-01

Consider (2.13) rewritten as (17)

$$\begin{aligned} \{U(\theta, \lambda), V(\theta, \lambda)\} = & \sum_{n=0}^{J+1} \{U_n^0, V_n^0\} P_n^0(\cos \theta) \\ & + 2 \operatorname{Re} \left[\sum_{m=1}^J \sum_{n=m}^{m+J+1} \{U_n^m, V_n^m\} P_n^m(\cos \theta) \right] e^{im\lambda} \end{aligned} \quad (2.24)$$

Eq. (2.17) may be evaluated numerically as (32)

$$\{U^m, V^m\} = \sum_{n=m}^{m+J+1} \{U_n^m, V_n^m\} P_n^m(\cos \theta) \quad m=0, \dots, J \quad (2.25)$$

Equation (2.24) can now be written as (32)

$$\{U(\theta, \lambda), V(\theta, \lambda)\} = \sum_{m=0}^J \{U^m, V^m\} e^{im\lambda} \quad (2.26)$$

and its form suggests the application of a Fast Fourier Transform (FFT).

As stated earlier, 144 points were used in the longitudinal direction for the Gaussian grid. It can be shown that if $f(x)$ is a trigonometric polynomial of degree not exceeding $N-1$, that (32)

$$\int_0^{2\pi} f(x) dx = \frac{2\pi}{N} \sum_{j=0}^{N-1} f\left(\frac{2\pi j}{N}\right) \quad (2.27)$$

is an exact quadrature.

In the case of Eq. (2.17), trigonometric polynomials of degree up to $3J$ will arise in the quadratic terms. It is required that $N \geq 3J+1$ be the transform grid resolution for exact integrations. This requires N to be greater than or equal to 91. The AFGL model meets this condition, using $N=144$ equally spaced longitude points. From Eq. (2.27), Eq. (2.17) for a given colatitude θ_k , gives Fourier coefficients found via a FFT as (32):

$$\{U^m(\theta_k), V^m(\theta_k)\} = \frac{1}{N} \sum_{j=0}^{N-1} \{U(\theta_k, \lambda_j), V(\theta_k, \lambda_j)\} e^{-im\lambda_j} \quad (2.28)$$

where $\lambda_j = 2\pi j/N$

and $U(\theta_k, \lambda_j)$ and $V(\theta_k, \lambda_j)$ are known gridded input values

From Eq. (2.28), the integral in Eq. (2.21) is replaced with the G-L quadrature of (2.21) to yield the spectral coefficients of the wind (i.e., the desired output of AFGL).

The vorticity and divergence equations show the nonlinear aspect of the hydrodynamical equations for two-dimensional planetary circulations of the earth's atmosphere (Eq. 2.2). This nonlinearity produces truncation errors that lead to computational instabilities when employing classical finite differencing techniques (15). If the prognostic variables are represented in the spectral domain, then the truncation errors are avoided completely because all interactions which contribute to harmonics outside of the truncated set S (given as 32 by 31) in wave-number space are automatically eliminated. This property is the principal advantage for using spectral methods.

III. Locator Model

A locator model is used to track space and time histories of particles within dust clouds that are generated by nuclear or non-nuclear explosions. The locator model is part of REDRAM which tracks a set of user-specified initial particle sizes from an initial stabilized cloud through a spatially-variable wind field to the ground. REDRAM linearly interpolates the particle trajectory histories to find the positions of the particles at a user-specified "freeze frame" time. The near vertical line connecting the trace particle positions at the freeze frame time is the freeze frame cloud axis. REDRAM accounts for particle spatial distributions by expanding normal density functions in three directions about each particle (modal) position. Figure III-1 illustrates the freeze frame cloud axis for a hypothetical one megaton burst at Warren AFB for a freeze frame time of eight hours after burst. The figure shows the freeze frame cloud axis projected on back faces of latitude versus height and longitude versus height. These projections represent the freeze frame cloud axis skewed in space at the eight hour freeze frame time. Trace particles smallest in size are located at the top of the cloud axis and trace particles largest in size are located at the cloud axis bottom. A shadow projection of these trace particles onto the map of the United States represents modal positions (points of peak gaussian values) onto the ground.

The residues from nuclear dust clouds have defense planners concerned about long time free-field environments resulting from dust clouds generated by massive nuclear strikes and the impact these environments will have on mission completion for airborne aircraft and other retaliatory defenses. The modeling techniques described below are used to predict particle transport of fallen and/or falling environments.

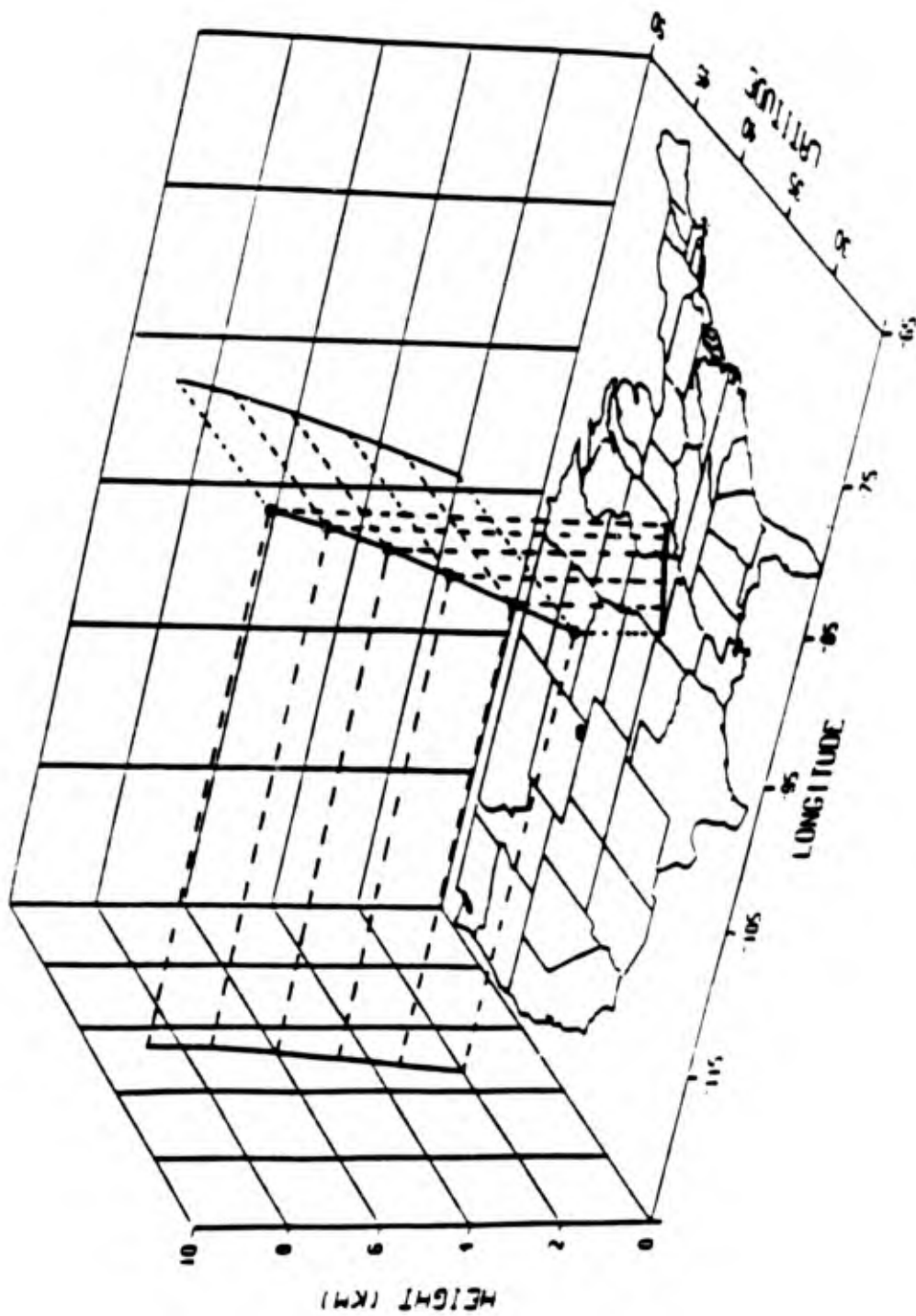


Figure III-1. Freeze frame cloud axis for a one megaton burst detonated at Warren AFB eight hours after burst.

Particle Size Distributions

Dust clouds generated by surface nuclear or non-nuclear bursts modeled numerically on a computer must have initial conditions specified in order to simulate the initial physical properties of the clouds. One such initial condition is the initial particle-size distribution chosen to represent the initial stabilized distributed cloud. Dose calculations resulting from nuclear clouds are very sensitive to the choice of these particles. Due to lack of nuclear test data, the choice of the particle-size distribution and of the trace particles which represent it is also one of much controversy. Non-nuclear dust clouds are not as controversial because much of the required data needed for analysis exists.

The number-size distribution generated by a nuclear surface burst is modeled as perfect spheres having radii, r , and a lognormal distribution (7):

$$N(r) = \frac{N_t}{\sqrt{2\pi} \beta r} \exp\{-(1/2)[(\ln(r) - \alpha_0)/\beta]^2\} \quad (1/m) \quad (3.1)$$

where N_t is the total number of particles and β is the logarithmic slope. The n^{th} moment of a lognormal distribution having the same slope β is also lognormal with (7)

$$\alpha_n = \alpha_0 + n\beta^2 \quad (3.2)$$

where α_0 is the logarithm of the median number-size radius $\ln(r_0)$. Using DELFIC default spectrum as the number-size distribution yields $\alpha_0 = \ln(.204)$ and $\beta = \ln(4)$. This spectrum represents Nevada test site soil.

Bridgman and Bigelow showed that the weighted sum of two lognormal distributions could represent the DELFIC default activity-size distribution. This distribution is given as (7)

$$A(r) = f_v \frac{A(t)}{\sqrt{2\pi} \beta r} \exp\{-(1/2)[(\ln r - \alpha_3)/\beta]^2\} \\ + (1-f_v) \frac{A(t)}{\sqrt{2\pi} \beta r} \exp\{-(1/2) [(\ln r - \alpha_2)/\beta]^2\} \quad (3.3)$$

f_v is the fraction of total activity which distributes volumetrically and they suggest $f_v=.68$, $(1-f_v)$ is the fraction of surface distributed activity, r is in meters and $A(t)$ is the total activity (in curies) given by (14)

$$A(t) = A_1 t^{-1.2} \text{ (Ci)} \quad (3.4)$$

where A_1 is the one-hour reference activity and is equal to 530 gamma megacuries per kiloton of fission yield and $t^{-1.2}$ is the Way-Wigner activity decay approximation in units of hours, valid for times greater than 10 minutes.

Initial Stabilized Cloud

The initial stabilized cloud occurs at the point where the rising radioactive particles stop rising. At this point, the gravity-sorted particles are modeled using correlations to DELFIC cloud height data (16). Average wafer center heights for each DELFIC particle diameter was used as the initial condition for the vertical distribution in the stabilized cloud. Figure III-2 shows particle-size variations to average wafer center heights for initial clouds of five different nuclear yields. Particle sizes and heights are linearly related by the slopes and intercepts given in figure III-2. Hopkins (16) used a polynomial least-squares fit from DELFIC burst data for yields of 1 kiloton to 15 megatons to express this linear relation as

$$\begin{aligned} \text{Slope} = & -\exp\{1.574 - .01197 \ln Y + .03636 (\ln Y)^2 \\ & - .0041 (\ln Y)^3 + .0001965 (\ln Y)^4 \} \end{aligned} \quad (3.5)$$

$$\begin{aligned} \text{Intercept} = & \exp\{7.889 + .34 \ln Y + .001226 (\ln Y)^2 \\ & - .005227 (\ln Y)^3 + .000417 (\ln Y)^4 \} \end{aligned} \quad (3.6)$$

where Y= weapon yield (kilotons), Slope is in vertical meters per micrometer of particle diameter and Intercept is the altitude (in meters) of the average wafer center height.

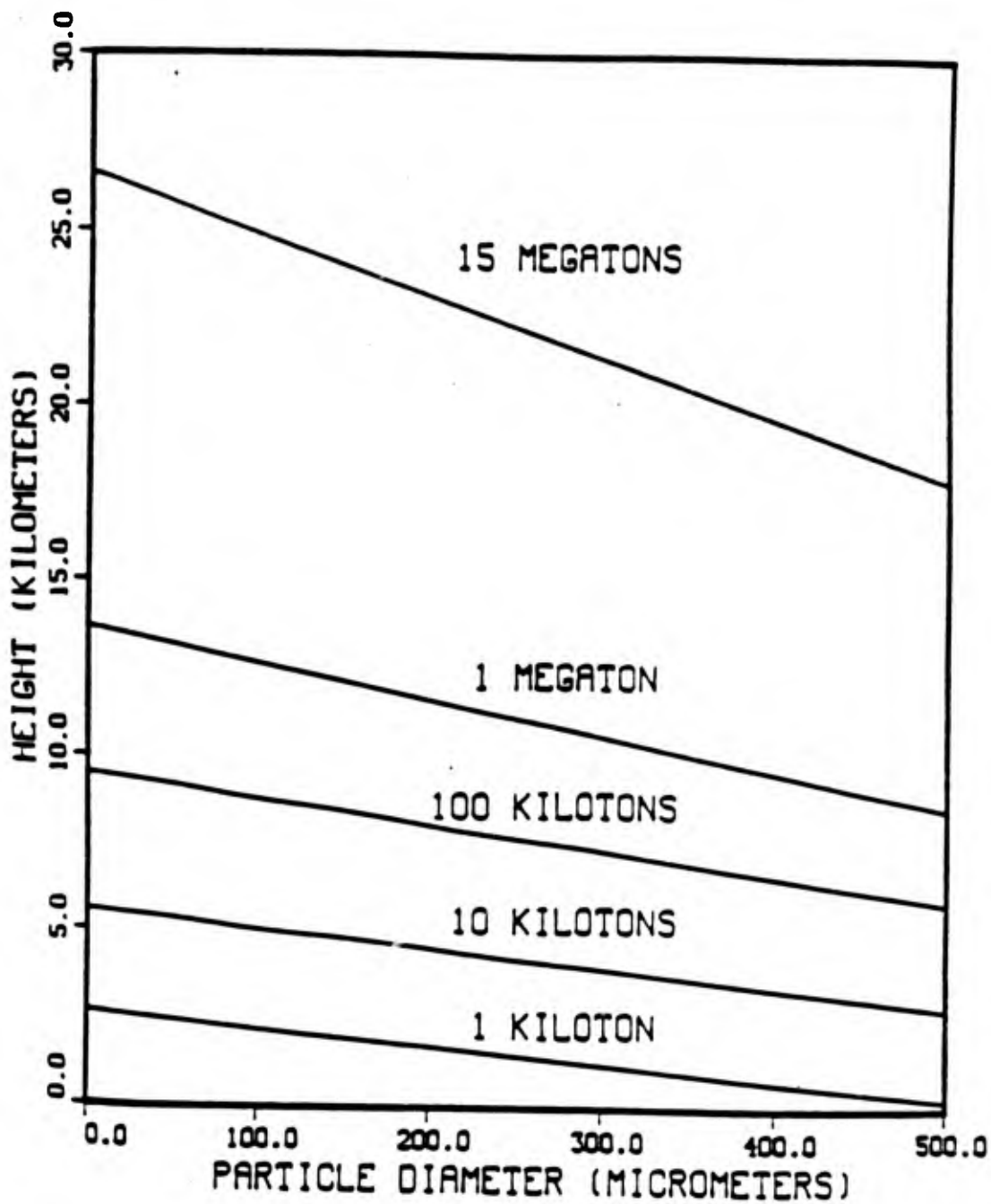


Figure III-2. Linear relation of average wafer center heights versus DELFIC initial particle-sizes for various yields (17:29)

Layered Atmosphere

As mentioned in chapter II, the spectral heights represent the computed spectral coefficients for 12 pressure levels of atmosphere. In order to model particle transport using these coefficients, the atmosphere must have a sufficient number of layers to produce accurate hotline locations. Hopkins showed that using more than 24 layers would not greatly increase the accuracy of the hotline location, and that going from 24 to 10 layers results in approximately a five percent change in hotline accuracy (17). Since winds are taken twice daily, the best "forecasted" prediction AFGL can make for hotline locations is 12 hours. This results in inaccuracies of hotline predictions and is considered larger than the 24 to 10 layer deviation. A computer savings of 50% results in a 10 layer choice (opposed to 24 layers) and is thus chosen as the modeling parameter. Figure III-3 shows the relation of a 10-layered atmosphere to particle-size and spectral heights for a one megaton initial cloud.

REDRAM models the initial cloud in a layered atmosphere by linearly interpolating in height the spectral winds. The interpolated winds transport falling particles in the lateral directions to produce locations of falling particles in time.

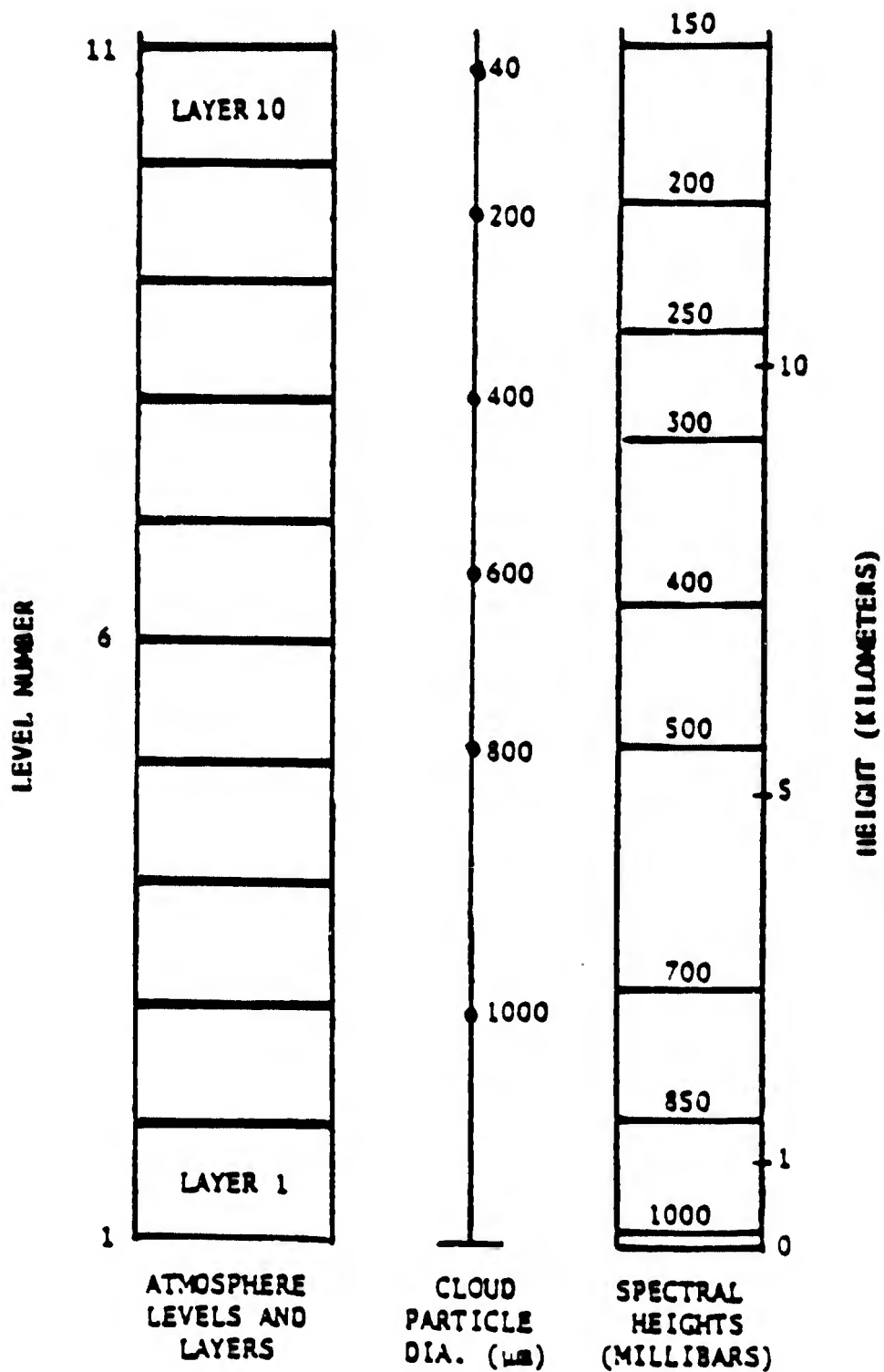


Figure III-3. Model heights compared to particle-sizes and spectral heights for a one megaton initial cloud (17:33).

Fall Mechanics in a Layered Atmosphere

REDRAM models the layered atmosphere using equations of state for a U.S. Standard Atmosphere (23). Terminal velocities of each particle within a layered atmosphere are calculated using Davies-McDonald fall mechanics (7) in order to obtain the particle's residence times.

The terminal velocities, V_z , of free-falling spheres in air can be determined from a balance of forces equation given as (7)

$$\{(1/2) \rho_a(z) V_z^2\} C_d(V_z) \pi r^2 = (4/3) \pi r^3 \rho_f g \quad (3.6)$$

where the left hand side of (3.6) is the force due to aerodynamic drag and the right hand side is particle weight due to gravity. Each parameter in Eq. (3.6) is defined as:

$$\{(1/2)\rho_a(z) V_z^2\} = \text{dynamic pressure}$$

$$\rho_a(z) = \text{air density as a function of altitude}$$

$$C_d(V_z) = \text{drag coefficient as a function of terminal velocity}$$

$$\pi r^2 = \text{particle cross sectional area}$$

$$\rho_f = \text{particle solid density}$$

$$g = \text{gravitational constant}$$

Equation (3.6) is not useful because it is a single equation in two unknowns (V_z and C_d).

McDonald (20) noted that the Reynolds number for falling spheres is given by

$$R_e = \frac{2 V_z \rho_a(z) r}{\eta(z)} \quad (3.7)$$

where R_e is the Reynolds number and $\eta(z)$ is the dynamic viscosity of air as a function of altitude. Solving (3.7) in term of the terminal velocity yields

$$V_z = \frac{R_e \eta(z)}{2\rho_a r} \quad (3.8)$$

Substituting (3.8) into (3.6) becomes

$$R_e^2 C_d = \frac{32 \rho_a \rho_f g r^3}{3 \eta^2} \quad (3.9)$$

where arguments have been suppressed.

Equation (3.9) does not help in determining terminal velocities because the left hand side is a product of two unknowns. However, Davies (10) related Reynolds number to the product $R_e^2 C_d$ by

$$R_e = (R_e^2 C_d / 24) - 2.3363 \times 10^{-4} (R_e C_d)^2 + 2.0154 \times 10^{-6} (R_e^2 C_d)^3 - 6.9105 \times 10^{-9} (R_e^2 C_d)^4 \quad (3.10)$$

for $R_e^2 C_d < 140$; $R_e < 4$

$$\log_{10}(R_e) = -1.29536 + .986 \log_{10}(R_e^2 C_d) - .046677 [\log_{10}(R_e^2 C_d)]^2 + .0011235 [\log_{10}(R_e^2 C_d)]^3 \quad (3.11)$$

for $100 < R_e^2 C_d < 4.5 \times 10^7$; $3 < R_e < 10000$

For a given particle of radius r , at an altitude z , the quantity $R_e^2 C_d$ is found from Eq. (3.9). Using Eq. (3.10) or (3.11) gives the Reynolds number needed to determine the terminal velocity in Eq. (3.8). The slip factor correction for drag "slip" at high altitudes is given as (7:212)

$$V_z = V_z \left(1 + \frac{1.165 \times 10^{-7}}{\rho_a r} \right) \quad (3.12)$$

where V_z in the right hand side of Eq. (3.12) is computed from (3.8), r is in meters and ρ_a has units of Kg/m^3 .

Using the average terminal velocities for each layer allows computation of the particle residence times for each particle in each layer and is given by the following equation (16).

$$t_{ik} = \frac{\Delta z}{\left[\frac{(V_z)_j + (V_z)_{j+1}}{2} \right]} \quad (3.13)$$

where

k = layer number bounded by heights j and $j+1$

t_{ik} = residence time of i^{th} particle in the k^{th} layer

Δz = constant layer thickness given as the highest initial particle height (smallest sized particle) divided by the total number of layers

$(V_z)_j$ = terminal velocity of particle at bottom layer height

$(V_z)_{j+1}$ = terminal velocity of particle at top layer height

The total time for the i^{th} particle to fall from its initial height to the ground is given as

$$TFALL = \sum_{k=1}^{NL} t_{ik} \quad (3.13a)$$

where $TFALL$ = total fall time of the i^{th} particle (seconds)

NL = total number of model layers given in Fig. III-3

The above equations assume spherical particles of constant density falling freely through a discretized atmosphere and uses the smallest sized particle to initialize the highest layer height. Figure III-4 shows total fall times for particles falling through a U.S. Standard Atmosphere.

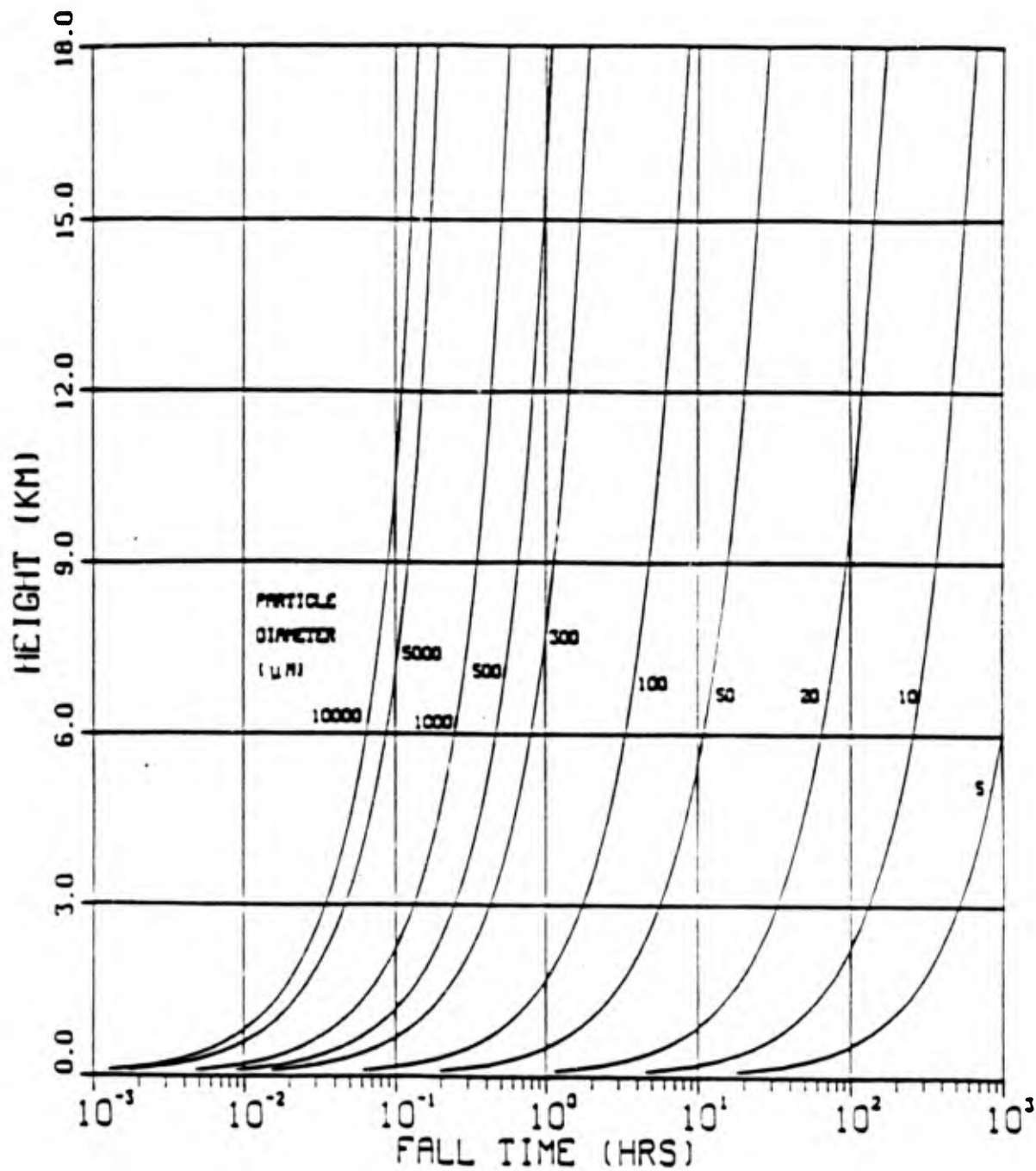


Figure III-4. Fall times for particles falling through a U. S. Standard Atmosphere (17:35)

Wind Shear

Vertical wind shear is the rate of change of wind velocity with distance perpendicular to the wind direction and gives a measure of the dispersive effect wind has on falling particles within the cloud. Vertical wind shear is represented as (17)

$$s_x = \Delta u / \Delta z \quad (3.14)$$

$$s_y = \Delta v / \Delta z \quad (3.15)$$

where

s_x = westerly vertical wind shear component at the k^{th} layer

s_y = southerly vertical wind shear component at the k^{th} layer

Δz = layer thickness defined in (3.13)

Δu = westerly spectral wind component within Δz

Δv = southerly spectral wind component within Δz

Wind shear is observed both near ground and in jet streams, where it may be associated with atmospheric turbulences acting on the cloud. For nuclear clouds, wind shear is considered to dominate lateral spreading effects at times greater than three hours after burst (25).

REDRAM calculates wind shear for each particle size in the discrete cloud. The modeling equation is given as (17)

$$(S_x, S_y) = \left[\sum_i (s_x, s_y)_i^2 (t_i / \text{TFALL}) \right]^{(1/2)} \quad (3.16)$$

where

(S_x, S_y) = root-mean-square (rms) value of the wind components of

Eqs. (3.14) and (3.15)

t_i = residence time defined in Eq. (3.13) at the k^{th} layer

TFALL = total fall time of particle from initial cloud height to ground defined in Eq. (3.13a)

Weighted rms residence time values of net shear account for the time each particle spends in a k^{th} layer of atmosphere while transporting laterally.

Spatial Distribution of Stabilized Cloud

The spatial distribution of the initial stabilized cloud for any one trace particle size r_i , is modeled as a three-dimensional (3-D) normalized gaussian distribution. The spatial distribution function is given as:

$$F_i(x,y,z,t) = \frac{\exp\left[-\frac{1}{2}\left(\frac{x(t)-x_0}{\sigma_x(t)}\right)^2\right]}{\sqrt{2\pi}\sigma_x(t)} \cdot \frac{\exp\left[-\frac{1}{2}\left(\frac{y(t)-y_0}{\sigma_y(t)}\right)^2\right]}{\sqrt{2\pi}\sigma_y(t)} \cdot \frac{\exp\left[-\frac{1}{2}\left(\frac{z(t)-z_0}{\sigma_z(t)}\right)^2\right]}{\sqrt{2\pi}\sigma_z(t)} \quad (3.17)$$

where

t = time of freeze frame interpolation (seconds)

x_0 = Mode coordinate of ground zero in earth radians, of the i^{th} particle measured in a spherical coordinate system referenced to the prime meridian and projected onto a latitude-longitude mesh.

y_0 = Mode coordinate of ground zero in earth radians, of the i^{th} particle measured in a spherical coordinate system referenced to the north pole and projected onto a latitude-longitude mesh.

z_0 = Mode height of the i^{th} particle at ground zero (meters)

$x(t)$ = Temporally interpolated i^{th} particle position in earth radians referenced to the prime meridian and projected onto a latitude-longitude mesh. The particle modal position is computed as the product of the eastward spectral wind component, U , times the freeze frame interpolation time t .

$y(t)$ = Temporally interpolated i^{th} particle position in earth radians referenced to the north pole and projected onto a latitude-longitude mesh. The particle modal position is computed as the product of the northward spectral wind component, V , times the freeze frame interpolation time t .

$z(t)$ = Temporally interpolated i^{th} particle height (meters)

$\sigma_x(t)$ = Cloud standard deviation in West-East direction computed in earth radians

$\sigma_y(t)$ = Cloud standard deviation in South-North direction computed in earth radians

$\sigma_z(t)$ = Cloud standard deviation in vertical direction (meters)

In order to model 3-D normalized gaussian clouds, a latitude-longitude mesh is used to account for lateral particle translations in each discrete layer of atmosphere. Peak gaussian values represented by cloud center axes correspond to mode coordinates on the latitude-longitude mesh for fixed altitudes and time. Off-axis particle locations are tracked initially by using a quarter-mesh in the north-east quadrant of a latitude-longitude grid referenced at the mode. Expansions of quarter-meshes into 3-D gaussians for each particle are accomplished by noting the gaussian clouds are symmetric about the mode locations. Use of symmetry results in large savings in computational search time. Figure III-5 is a cartoon depiction of how particles are modeled with 3-D gaussians. Fig. III-5a begins with gravity sorted particles at an initial stabilized time. Fig. III-5b represents particle locations after translation and wind shear. Fig. III-5c shows the particle mode location and north-east quadrant of the latitude-longitude mesh used for expanding the 3-D gaussians. Fig. III-5d

portrays a 3-D gaussian cloud generated by expanding the north-east quadrant of the latitude-longitude mesh into a discrete volumetric cell. Figure III-6 represents an unexpanded gaussian quadrant of a latitude-longitude mesh in a discretized atmosphere for five particles. Figure III-7 is the 3-D gaussian cloud fully expanded in the lateral directions for three particles. Cloud boundaries are chosen 3σ in all directions from the particle mode locations. This accounts for particles lying within 99.75% of the gaussian cloud.

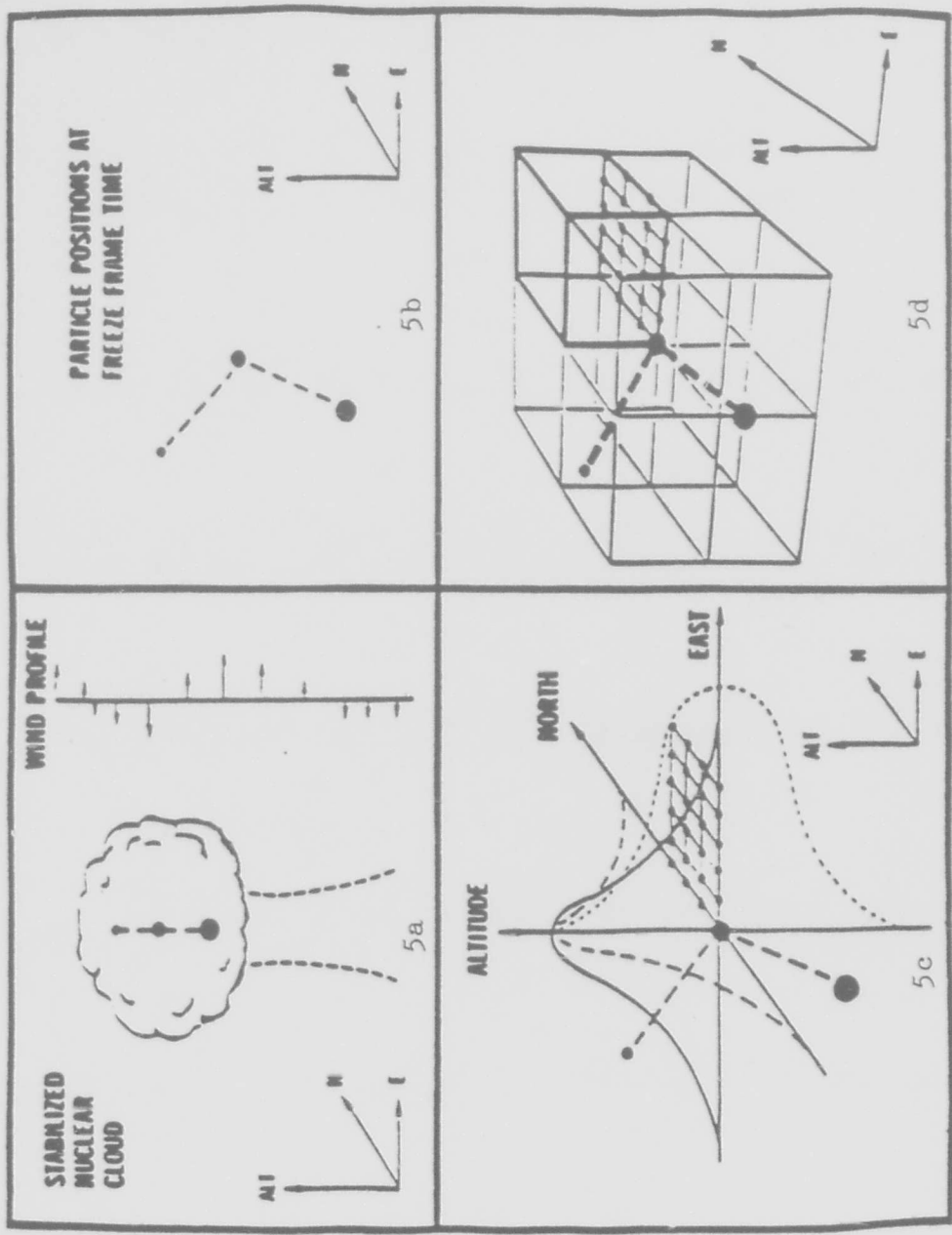


Figure III-5. Three-dimensional gaussian cloud model for particles transported in space at a fixed freeze-frame time.

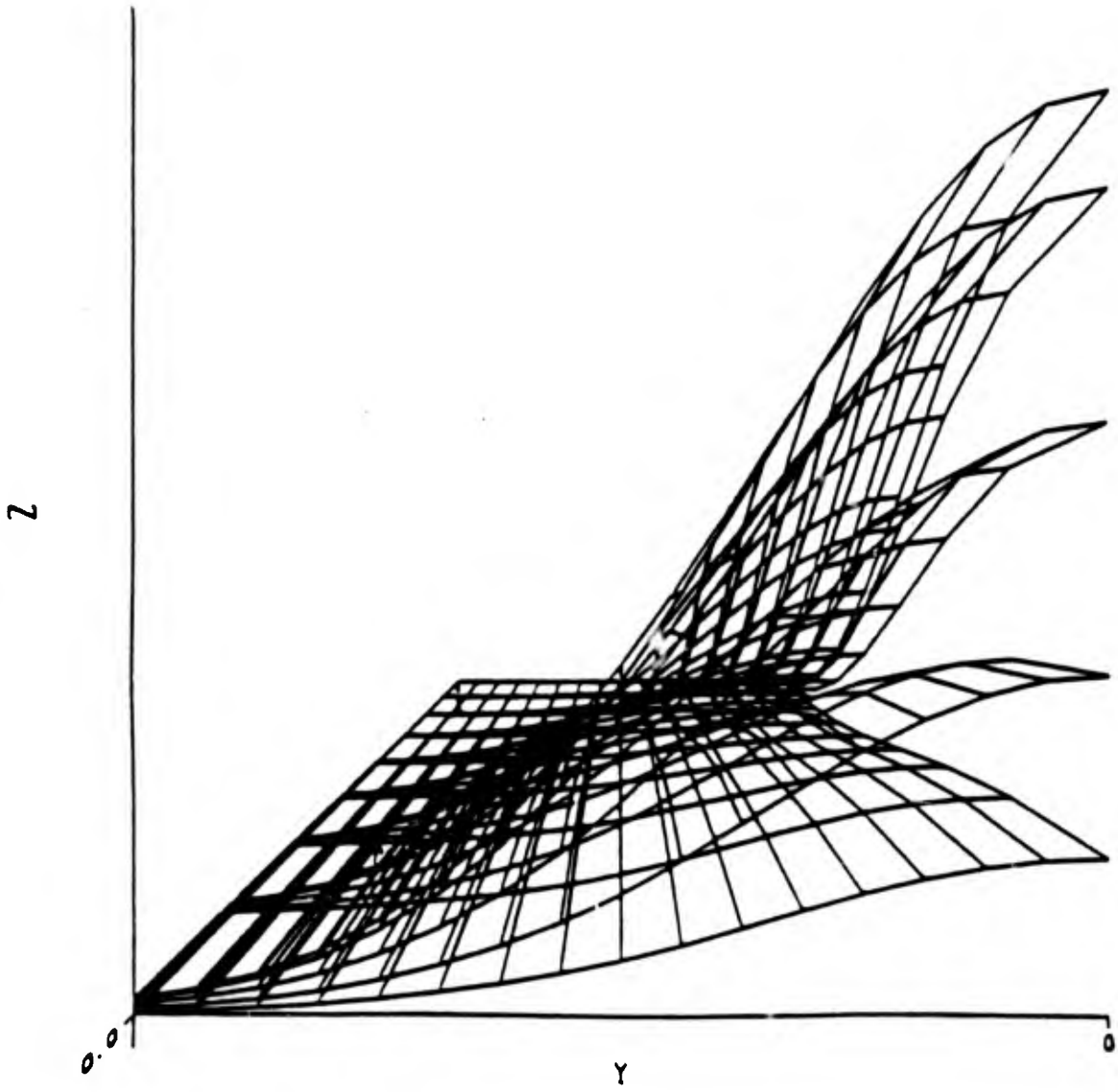


Figure III-6. Unexpanded gaussian quadrant of a latitude-longitude mesh in a discretized atmosphere for five particles.

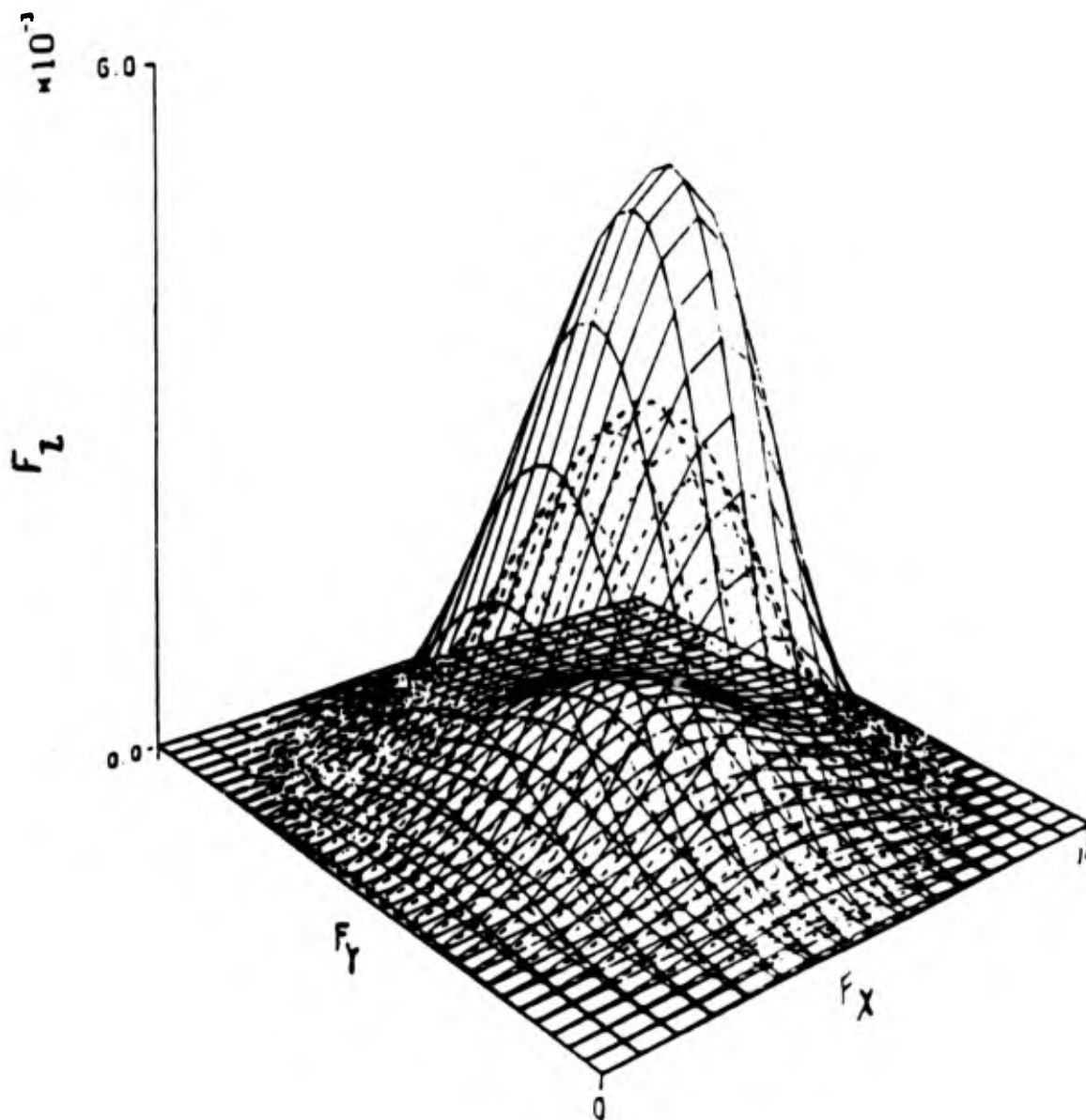


Figure III-7. Fully expanded two-dimensional gaussian lateral spatial representation for three particles.

Cloud Deviations

In addition to translation the gaussian functions also spread with time. This was indicated in Eq. (3.17) with standard deviations which were functions of time. AFIT's fallout model uses WSEG empirical fits to treat cloud standard deviations defined in Eq. (3.17). Crosswind deviation, σ_y , given in the AFIT Fallout Model for constant V_x winds is (30:73)

$$\sigma_y^2(t) = \sigma_0^2(1 + 8 t_a^*/T_c) + (t S_y \sigma_h/2)^2 \quad (\text{km}) \quad (3.18)$$

where

$$\sigma_0 = 1.609 \exp \left[.7 + \frac{1}{3} (\ln Y) - \frac{3.25}{4 + (\ln Y + 5.4)^2} \right] \quad (\text{km}) \quad (3.19)$$

equals the initial cloud radius parameter

t_a^* = elapsed time for toroidal growth = t for $t \leq 3$ hours, or 3 for $t > 3$ hours

$$T_c = 12 \left(\frac{H_c}{60} \right) - 2.5 \left(\frac{H_c}{60} \right)^2 \quad (\text{hours})$$

equals the characteristic time for rate deposition to decrease $1/e$ of maximum value

Y = Yield (megatons) for $.001 \leq Y \leq 100$ megatons

$$H_c = 44 + 6.1 \ln Y - .205(\ln Y + 2.42) |\ln Y + 2.42| \quad (\text{kilofeet})$$

equals the initial stabilized cloud center height

$$\sigma_z = .18 H_c \quad (\text{kft})$$

$$\sigma_h = .305 \sigma_z \quad (\text{km})$$

t = freeze frame time (hours)

S_y = wind shear in y direction (hours^{-1})

The first term in Eq. (3.18) accounts for early times where toroidal growth of the nuclear cloud dominates. The second term represents growth due to wind shear and becomes significant for times greater than 3 hours.

Equation (3.19) is from the WSEG model (17) and Eq. (3.18) has its origin in WSEG but was modified by Bridgman (30:73).

Hopkins used an analogous equation for (3.18) to account for lateral spread in the x direction. In the form of Eq. (3.18), the σ_x deviation is modeled as

$$\sigma_x^2(t) = \sigma_0^2 (1 + 8 t_q^* / T_c) + (t S_x \sigma_H / 2)^2 \quad (\text{km}) \quad (3.20)$$

Summary

The locator model computes freeze frame cloud axis locations for a given freeze time for falling trace particles as well as predicted hotline locations for fallen trace particles generated by a nuclear burst. Spherical particles falling freely through a U.S. Standard Atmosphere from the initial stabilized cloud are transported laterally through spectral winds. An increased number of atmospheric layers yields better accuracy in predicting hotline locations, but at the expense of doubling computer run time. Linear vertical interpolations of winds between spectral heights was assumed and used to compute wind shear at each level of altitude on each particle in space and time. Three dimensional normalized gaussian distributions are used to represent the expanding cloud. Use of gaussian symmetry about a central particle mode location results in a large savings in computational run time.

The locator model will be used to validate the particle transport and distributed mass resulting from a high explosive non-nuclear generated dust cloud.

IV. Validation

Direct Course HE Test

A passage from the abstract of the Defense Nuclear Agency (DNA) sponsored high explosives (HE) Direct Course Experiment is quoted for clarification as to the purpose and results of the test (19).

"The dust cloud (non-radioactive) generated in the Direct Course Experiment was successfully and safely sampled with an instrumented aircraft to determine the size and concentration of particulates. The principal methodology utilized for sizing "in-situ" cloud measurements were performed from 1.6 to T+64 minutes. The total mass lofted as measured from this data was found to be 2.86×10^8 gm., which is 5-6% of that lofted by a comparable sized surface burst. Typical mass loadings were a few tenths of a gram per cubic meter..."

Following is the Direct Course cloud analysis. A comparison of predicted mass histograms to measured data shows that particle transport is modeled accurately and realistically using a spectral wind fallout model.

Test Description

The Direct Course experiment took place at White Sands Missile Range, New Mexico. An elevated spherical charge of 600 tons of ANFO (ammonium nitrate / fuel oil) was detonated (at 33.6° North latitude and 106.5° West longitude) on 26 October, 1983, at 18:06 MDT on a tower approximately 50 meters above ground level (AGL) (see Figure IV-1). A Beechcraft Baron research aircraft mounted with light scattering imaging probes passed through the center of the dust cloud lofted by the explosion. These imaging probes are optical particle size spectrometers (19) used for making in-situ measurements of the

airborne dust particles. Within two minutes after detonation, the aircraft passed through the cloud's stem at an altitude of .28 kilometers. All passes up to pass 20 were ascending aircraft passes through the center of the wind sheared cloud/stem. Pass 7 is considered the cloud bottom (void of stem particles) and Pass 20 was estimated as the cloud top. Passes 21 through 28 are passes stepping down through the cloud, where Pass 28 reaches a bottom altitude of .74 kilometers.

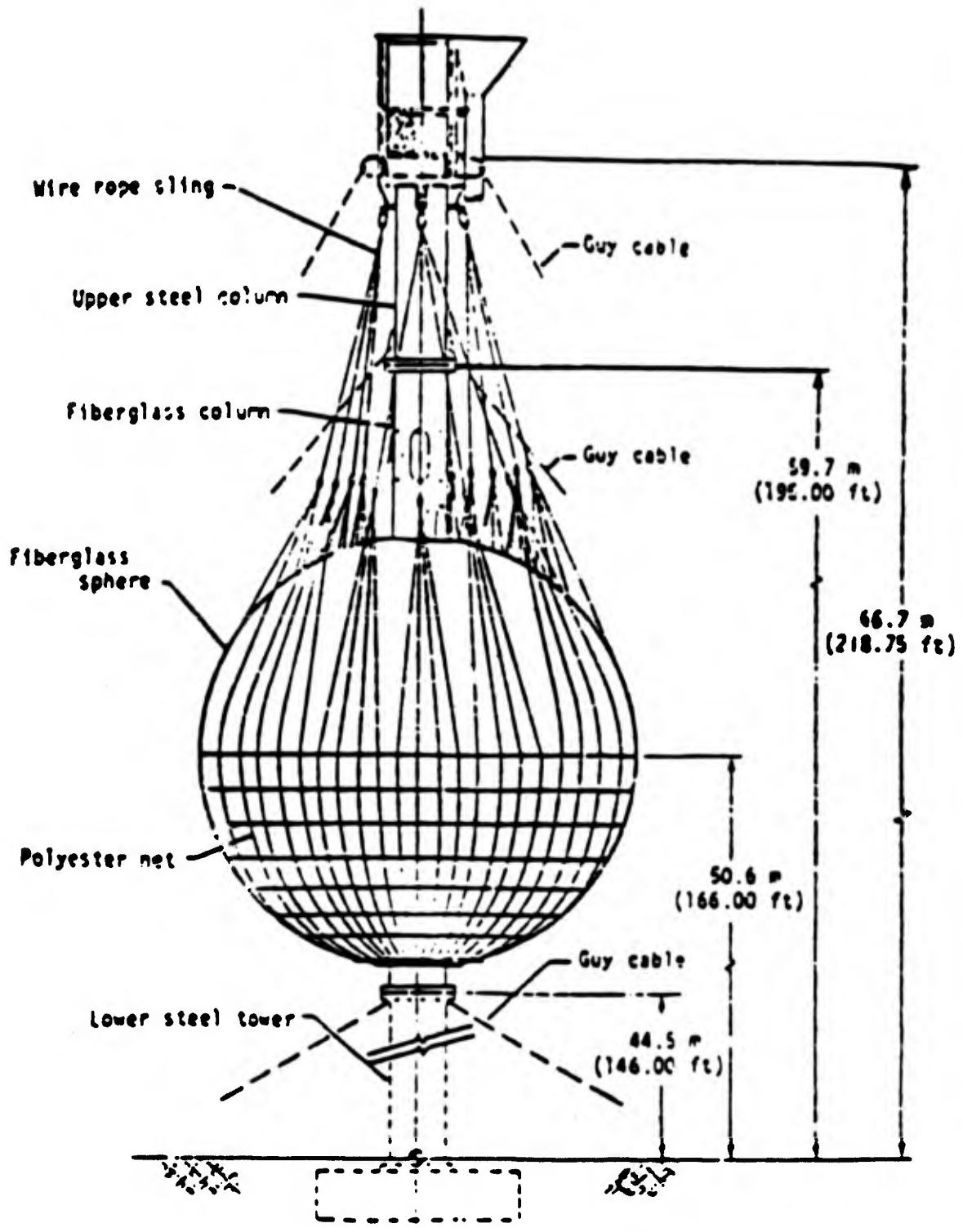


Figure IV-1. Direct Course tower and container support system (29:9)

Direct Course Test Results

Table IV-1 summarizes Direct Course measurements used in this validation. Columns 2, 3 and 4 of Table V-1 are average values of the aircraft altitude, magnetic heading and true airspeed for each particular pass. Columns 5 and 6 are times in and out of the cloud center and were determined to the nearest second. Column 7 is transit time the aircraft spent traversing the cloud boundaries through its center and column 8 gives the expanding cloud diameter as functions of space, time and particle transport due to wind shear effects.

Table IV-2 lists the kilograms of mass and accumulated mass for each pass and also the percent accumulation. The table is broken into a climb and a descent portion as illustrative of cloud dissipation with time.

Cloud width for the first 20 cloud passes is presented in Fig. IV-2. With the exception of mid-cloud fluctuations, a consistent expansion rate is observed.

Table IV-3 contains aircraft coordinates at the center of the cloud referenced to ground zero for each pass. Columns 2 and 3 give cloud center positions west and north of ground zero, respectively. Column 4 contains the mean sea level (MSL) altitudes of aircraft location for each respective pass to the cloud center and column 5 yields the time after burst for the aircraft to reach the cloud center for each pass.

TABLE IV-1.

Direct Course Cloud Measurements for the First 27 Passes (19)

Pass #	Altitude (km)	Magnetic Bending (deg)	True Airspeed (m/s)	Time In	Time Out	Transit Duration (sec)	Width (m)
1	0.28	325	88.0	12:07:34	12:07:43	7	615
2	0.44	108	89.7	12:08:33	12:08:44	11	986
3	0.39	253	89.5	12:09:29	12:09:39	10	895
4	0.73	033	86.8	12:10:22	12:10:34	12	1040
5	0.91	179	84.5	12:11:04	12:11:15	11	930
6	1.06	307	80.7	12:11:50	12:12:08	18	1450
7	1.21	099	82.0	12:12:43	12:13:10	27	2210
8	1.37	260	94.5	12:13:59	12:14:19	20	1890
9	1.52	317	97.0	12:15:22	12:15:53	31	3004
10	1.68	188	95.9	12:16:48	12:17:08	20	1910
11	1.84	322	99.0	12:18:14	12:18:38	24	2376
12	2.00	098	94.6	12:19:22	12:19:39	17	1608
13	2.16	352	98.2	12:20:35	12:20:59	24	2350
14	2.33	109	95.0	12:21:39	12:22:06	27	2565
15	2.48	260	96.7	12:22:50	12:23:22	32	3090
16	2.63	115	96.3	12:24:00	12:24:30	30	2890
17	2.79	255	98.5	12:25:22	12:25:55	33	3250
18	2.95	104	98.3	12:26:39	12:27:16	37	3636
19	3.12	253	97.5	12:28:08	12:28:29	21	2050
20	3.27	104	98.8	12:29:40	12:29:52	12	1185
21	2.97	255	92.0	12:31:51	12:32:16	24	2210
22	2.63	088	92.4	12:33:24	12:34:04	40	3690
23	2.32	193	89.9	12:35:37	12:36:05	28	2520
24	2.00	051	88.5	12:37:47	12:38:13	26	2300
25	1.69	161	88.3	12:39:58	12:40:31	33	2910
26	1.36	082	87.8	12:43:34	12:44:34	59	5180
27	1.05	230	83.0	12:47:58	12:48:57	59	4900

TABLE IV-2.

Direct Course Accumulated Mass Summary (19)

Pass #	CLIMB			DESCENT		
	Mass kg	Accum. Mass kg	Accum. %	Mass kg	Accum. Mass kg	Accum. %
1	34,160	3.416×10^4	11.94			
2	22,080	5.624×10^4	19.67			
3	6,300	6.254×10^4	21.87			
4	14,000	7.654×10^4	26.76			
5	17,280	9.382×10^4	32.81			
6	37,800	1.316×10^5	46.02			
7	71,400	2.030×10^5	70.99			
8	27,360	2.304×10^5	80.56			
9	6,690	2.371×10^5	82.91			
10	3,136	2.402×10^5	83.99			
11	5,536	2.457×10^5	85.93			
12	3,712	2.495×10^5	87.23			
13	7,136	2.566×10^5	89.73			
14	5,644	2.622×10^5	91.69			
15	5,850	2.681×10^5	93.74			
16	10,335	2.784×10^5	97.36			
17	5,440	2.838×10^5	99.26			
18	1,872	2.857×10^5	99.92			
19	232	2.859×10^5	99.99			
20	8	2.860×10^5	100.00	16.8	16.8	00.04
21				806	823	2.01
22				12214	1.304×10^4	31.77
23				3520	1.656×10^4	40.35
24				4743	2.130×10^4	31.91
25				3233	2.455×10^4	39.84
26				3193	2.755×10^4	67.62
27				3348	3.109×10^4	75.78
28				9938	4.103×10^4	100.0

DIRECT COURSE CLOUD WIDTH MEASUREMENTS

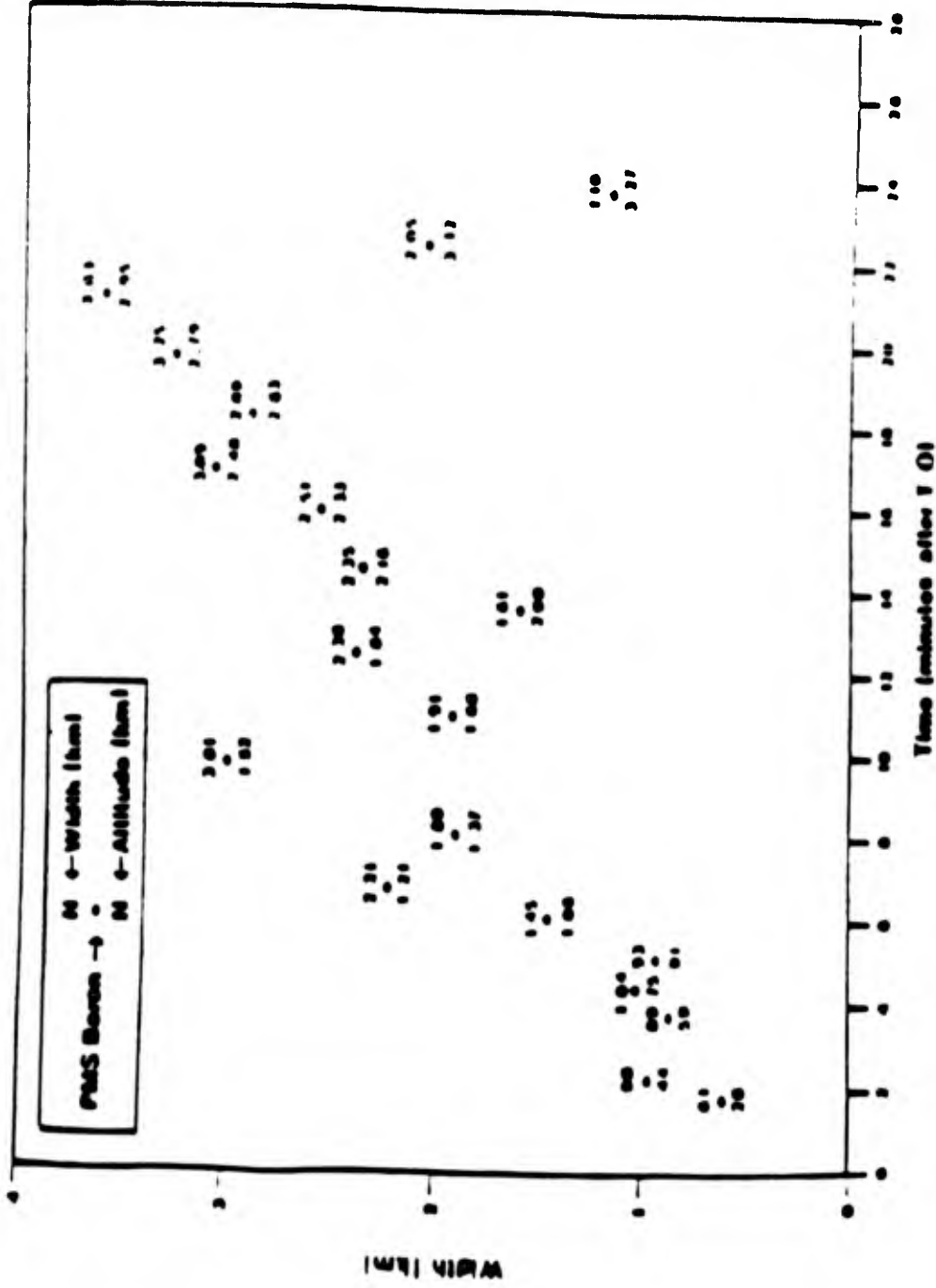


Figure IV-2. Measured cloud widths for the first 20 passes (19).

TABLE IV-3.

Direct Course Cloud Center Coordinates as functions of space and time
for passes 7 through 27

Pass #	West of GZ (km)	North of GZ (km)	Altitude (km)	Arrival Time (sec)
7	1.261	0.304	2.69	416
8	2.478	0.522	2.85	489
9	3.347	1.174	3.00	578
10	4.435	3.087	3.16	658
11	5.326	3.913	3.32	746
12	5.652	4.130	3.48	811
13	6.522	5.348	3.64	887
14	7.087	5.348	3.81	953
15	8.565	6.000	3.96	1026
16	8.870	6.609	4.11	1095
17	10.348	6.652	4.27	1178
18	10.957	7.087	4.43	1258
19	11.609	7.696	4.60	1333
20	13.478	8.087	4.75	1426
21	13.935	9.087	4.45	1564
22	14.348	10.522	4.11	1664
23	13.000	10.304	3.80	1791
24	13.913	10.783	3.48	1920
25	13.652	8.261	3.17	2054
26	12.609	0.783	2.48	2284
27	10.000	0.565	2.53	2548

Particle Size Spectrometers

The Two-Dimensional Optical Array Imaging Probe, OAP-2D-C, has 32 light sensitive diodes which are sampled at a rate comparable with the true airspeed of the aircraft, and produces a two dimensional image of particles in the range of sizes from 25 to 800 microns. Table IV-4 lists the lower, upper and mean range of each of the 32 channels.

The Forward Scattering Spectrometer Probe, FSSP, models 100 sized particles in the range from 4 to 62 microns. Table IV-5 lists the lower, upper and mean range for its 15 channels.

In order to save space in this report, the OAP-2D-C and FSSP combined histograms are tabulated in units of grams per cubic meter per micron and can be obtained from the DNA report (19). These histograms were compared in the validation to predicted results from REDRAM.

TABLE IV-4.
Micron Diameter Ranges for the OAP-2D-C.

Cloud #	Low (μm)	High (μm)	Median (μm)
1	17.75	42.5	30.5
2	42.5	67.25	54.875
3	67.25	92.0	79.625
4	92.0	116.75	104.375
5	116.25	141.5	129.125
6	141.5	166.0	153.75
7	166.0	190.5	178.25
8	190.5	215.25	202.875
9	215.25	242.0	228.625
10	242.0	264.75	253.375
11	264.75	289.0	276.875
12	289.9	313.75	301.375
13	313.75	338.25	326.0
14	338.25	363.0	350.625
15	363.0	387.5	375.25
16	375	425	400
17	400	450	425
18	425	475	450
19	450	500	475
20	475	525	500
21	500	550	525
22	525	575	550
23	550	600	575
24	575	625	600
25	600	650	625
26	625	675	650
27	650	700	675
28	675	725	700
29	700	750	725
30	725	775	750
31	750	800	775
32	775	825	800

TABLE IV-5.

Micron Diameter Ranges for the FSSP.

Channel	Low (μm)	High (μm)	Median (μm)
1	4	6	5
2	6	10	8
3	10	14	12
4	14	18	16
5	18	22	20
6	22	26	24
7	26	30	28
8	30	34	32
9	34	38	36
10	38	42	40
11	42	46	44
12	46	50	48
13	50	54	52
14	54	58	56
15	58	62	60

AFGL Validation

For validation of AFGL, NMC provided Hopkins with the AFGL spectral coefficient generator model and a set of winds for 12UT 26 Oct 83 and 00UT 27 Oct 83 (Hopkins already had the spectral coefficients for these times and dates (17)). Using these winds and AFGL, spectral coefficients were generated. Hopkins wrote a program to convert spectral coefficients back to winds in order to validate the operation of AFGL.

A statistical comparison was made that compared actual winds from NMC to winds derived from the AFGL spectral coefficients. For validation purposes (of AFGL), Direct Course wind data was used as a comparison. Three factors were used to determine the comparison.

$$(1) |\text{ERROR}| = |X_c - X_r|$$

$$(2) |\text{ERROR}|_{\text{avg}} = \frac{1}{N} \sum_{i=1}^N |X_c - X_r|_i$$

$$(3) |\text{ERROR}|_{\text{fractional}} = \frac{1}{N} \sum_{i=1}^N \left[\frac{|X_c - X_r|}{X_r} \right]_i$$

where X_c = calculated winds

X_r = reference winds from NMC

N = number data pairs.

As expected, the winds generated near the poles had largest errors, but at locations greater than 10° latitude from the poles the average error was approximately .2 m/s.

Due to problems of using small velocity winds for fractional error comparisons, two separate calculations were made, one for winds greater than or equal to 1 m/s and

another for winds greater than or equal to 2 m/s. At locations greater than 10° latitude from the poles the fractional errors between the generated and actual winds averaged .05 for winds greater than 1 m/sec.

Since areas of interest in the world are away from the poles and large winds are much more dominant than very small winds, the average and fractional errors computed verify AFGL as a good operational model.

Spectral Winds

In order to get optimum accuracy in predicting particle transport, spectral coefficients for 12UT 26 Oct 83 and 00UT 27 Oct 83 were linearly interpolated, producing a new set of spectral coefficients which effectively yield spectral coefficients at the date and time of detonation (Direct Course was detonated 18UT 26 Oct 83). Figures IV-3 through IV-6 show spectral winds over the United States computed at the lowest four levels above ground using the linearly interpolated spectral coefficients. These figures agree with Table IV-3 that the predominant winds at test site location were southeasterly.

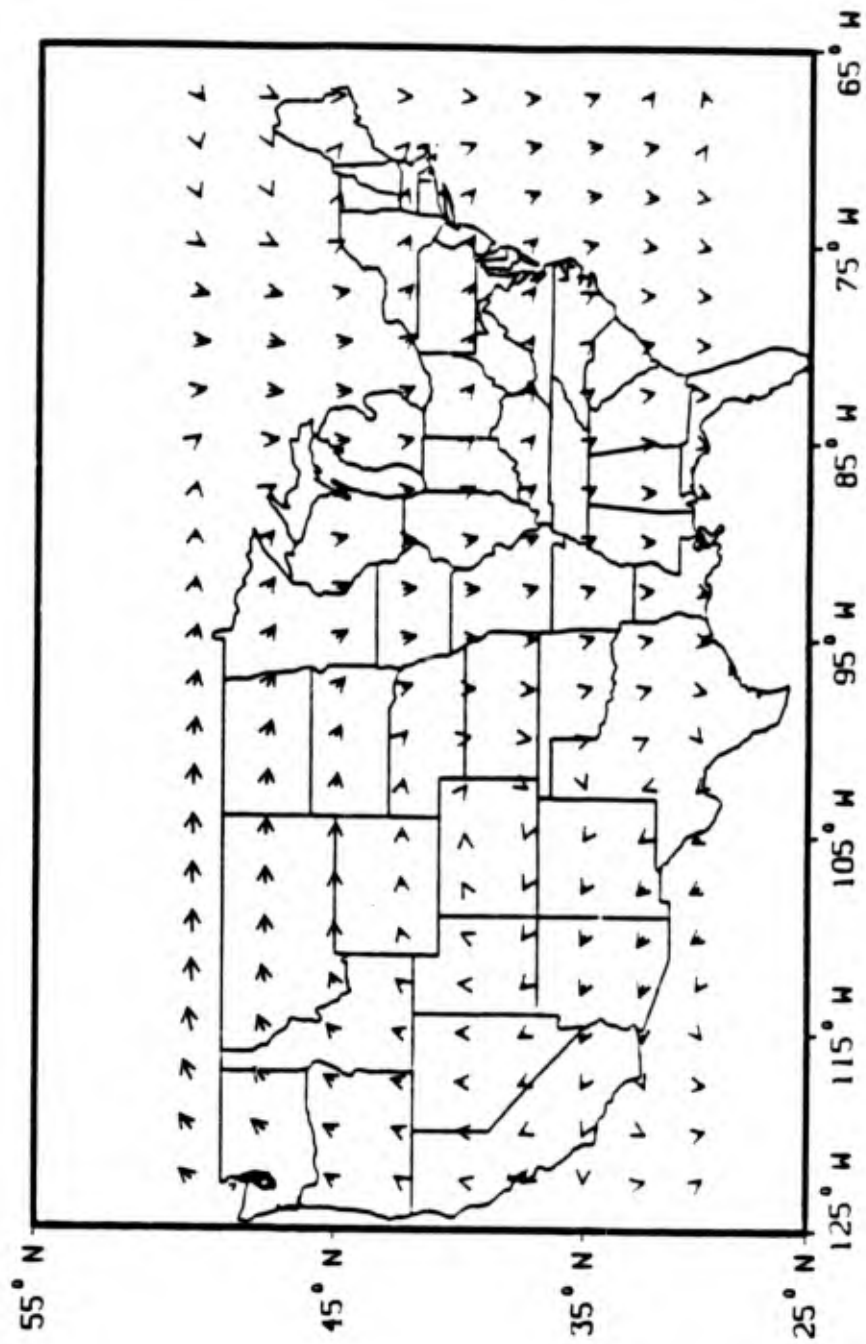


Figure IV-3. Interpolated 12UT 26 OCT 83 and 00UT 27 OCT 83 wind field (1000 mb).

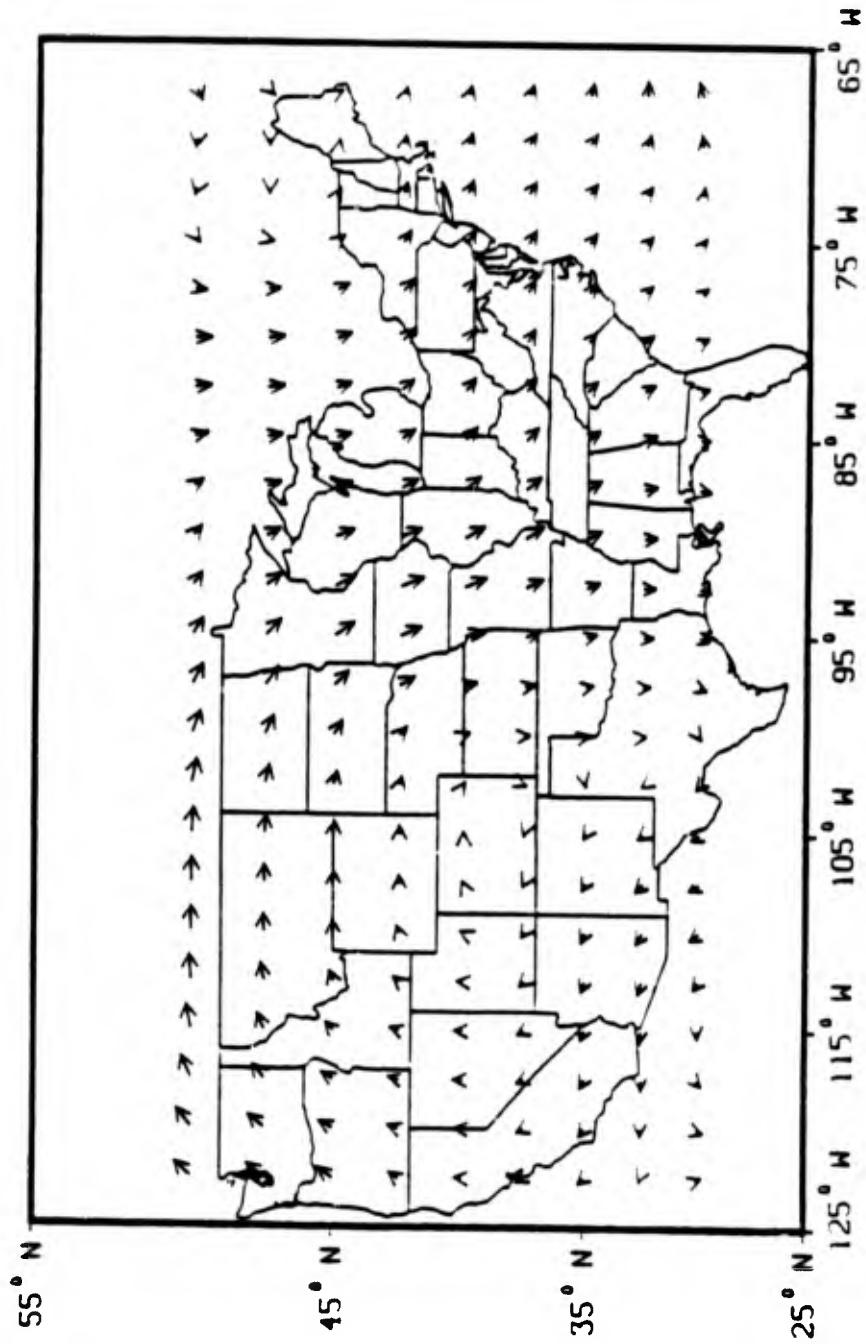


Figure IV-4. Interpolated 12UT 26 OCT 83 and 00UT 27 OCT 83 wind field (850 mb).

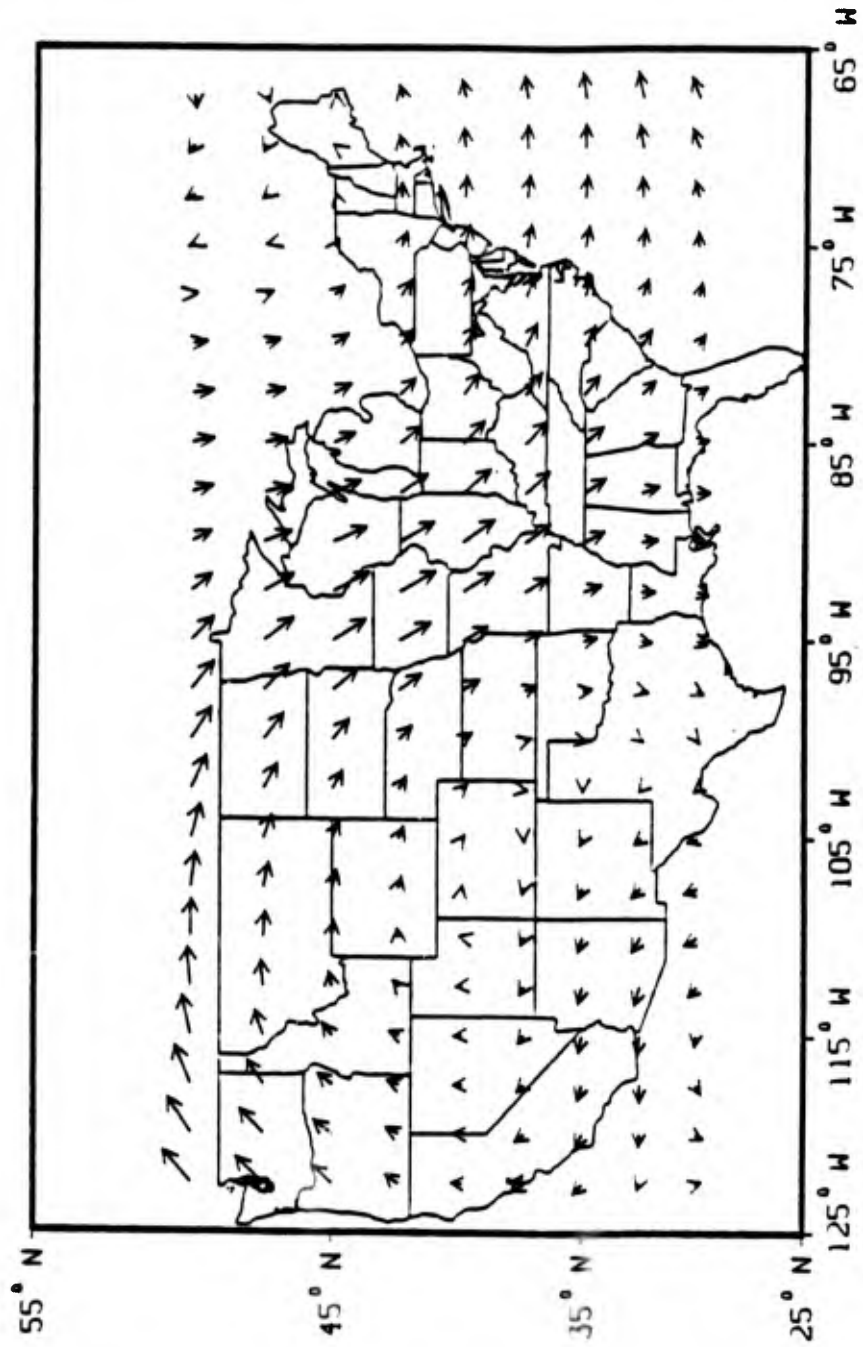


Figure IV-5. Interpolated 12UT 26 OCT 83 and 00UT 27 OCT 83 wind field (700 mb).

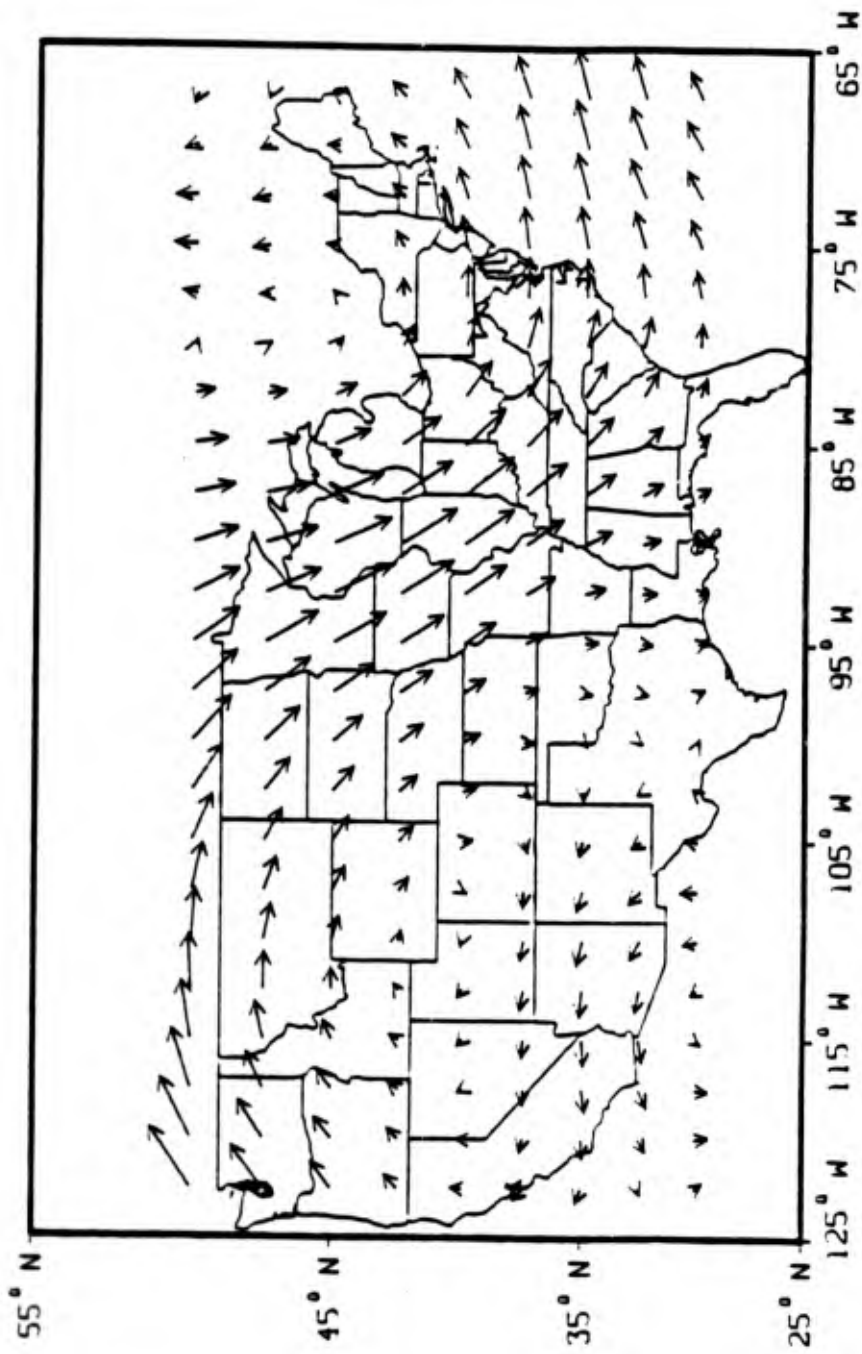


Figure IV-6. Interpolated 12UT 26 OCT 83 and 00UT 27 OCT 83 wind field (500 mb).

REDRAM does not accurately predict particle transport within the boundary layer of the earth (approximately one to three kilometers) because AFGL is a planetary model which predicts long wave circulation patterns of the earth's atmosphere. Terrain obstruction of surface winds within localized areas (between collecting sites) gives rise to errors when predictions via global spectral interpolations are used, and thus it is possible for cloud transport to be affected by atmospheric disturbances too small to appear within the spectral resolution of AFGL.

Boundary layer effects were ignored in the Direct Course validation because the analysis began at a stabilized cloud time (Pass 7) where the altitude (2.69 km MSL) was in the approximate transition region of the boundary layer.

Initial Particle Size and Filter Analysis

Tables IV-4 and IV-5 give the range of particle sizes the spectrometers used for in-situ cloud measurements. In order to compare mass histograms, REDRAM must use initial particle sizes within the ranges of these spectrometers. The mean-rounded (rounded up or down for values greater than or less than a half) values for each channel of the two spectrometers were chosen as the initial particle sizes. In order to conserve run time in the Direct Course analysis, the first 25 mean-rounded channel values were chosen and are contained in Table IV-6.

TABLE IV-6.

Initial Particle Sizes Used in REDRAM for Direct Course Analysis

<u>Channel #</u>	<u>Diameter (μm)</u>
1	5
2	8
3	12
4	16
5	20
6	24
7	28
8	32
9	36
10	40
11	44
12	48
13	52
14	56
15	60
16	80
17	105
18	129
19	154
20	203
21	203
22	229
23	253
24	277
25	301

Results from Direct Course filter analysis of aircraft filter samples showed that numerous metallic fragments of various sizes and shapes were present in the filters and it was concluded that these fragments were radar chaff remnants from a chaff source placed on the surface near ground zero. Sizes varied from 5 μm pieces to 1 mm strands with a width of 20 to 50 μm . Many of the fragments appeared to have been melted or stressed by the blast.

A near absence of large particles (greater than 200 μm) on the filter media was observed. Since the OAP-2D-C Spectrometer recorded large particles in-situ (for the same pass), it was concluded that most of the large particles as seen by the OAP-2D-C were actually aggregates. Specifically, there was evidence on most filter media elements of breakups of these large aggregates, which were seen in-situ by the OAP-2D-C Spectrometer.

While there were a number of spherical particles present on the various filter media, most were irregular fragments, and a large percentage of these were platelike. The composition of the nearly spherical particles observed on the filters was glassy, with the possible source being the HE sphere itself. Vaporization of the HE fiberglass sphere by the explosion followed by condensation could explain the presence of glassy spherical particles.

Presenting the above filter analysis demonstrates the discrepancies that may arise concerning particle morphology and the spherical particle assumption. Different shaped particles have different coefficients of drag and thus have different fall rates.

The spectrometers used in-situ were calibrated to glass beads and other spheres of known sizes. Detection within the fixed resolution of these instruments should yield objects which have sphere or near spherical shapes. This is supported by the fact that metallic fragments and fibers were not detected by the spectrometers but were found in

microscopic examination of the filter media, and by the fact that large aggregates (spherical) were measured with the spectrometers and verified in the filter analysis (as breakups).

Thus, since REDRAM compares predicted histograms with spectrometer results, and based on the last argument, use of the spherical particle assumption in REDRAM was chosen.

Direct Course HE Cloud Analysis

Unlike cloud modeling for a nuclear burst, HE cloud modeling is more precise because the data exists (as functions of time and space) for cloud top and bottom heights, and cloud widths. Complex bomb physics (fractionation, updrafts and toroidal circulation) accompanying a nuclear burst need not be accounted for when modeling HE initial clouds. Due to this lack of nuclear phenomenology, REDRAM was modified to account for a HE burst.

Pancake Cloud

In chapter III, it was mentioned that a nuclear burst produces particles in a stabilized cloud which are gravity sorted. This is not the case for a HE burst. Bridgman (7) showed that if the vertical activity distribution (initial particle-size distribution in this case) is symmetric about the cloud's center, the vertical cloud distribution can be reduced to a pancake cloud at its center.

The cloud center height for the pancake model was chosen as the average of the cloud top (3.27 km AGL) and bottom (1.21 km AGL). The terrain height of 1.48 km was added to this average (2.2 km AGL) height to yield the cloud's center height of 3.68 km MSL.

Based on Hopkins' analysis of Mount St. Helens (17), he found that the cloud's vertical thickness represented by the σ_z parameter (see chapter III) for the vertical

distribution of the gaussian cloud was equivalent to $4\sigma_z$. Using this result, the HE cloud thickness was chosen as

$$Z_T - Z_B = 4\sigma_z \quad (4.1)$$

where Z_T is the cloud top height ≈ 3200 m

Z_B is the cloud bottom height ≈ 1200 m

Thus, the σ_z value chosen for the HE model was 500 meters.

Lateral Expansion

A linear regression was made on the data in Figure IV-2 and is given in Figure IV-7. The expanding radius of the HE cloud as a function of time can be expressed as

$$R = (mt + b)/2 = 0.04121 t + 0.51728 \quad (4.2)$$

where R is the cloud radius in kilometers, m and b are the slope (in km/min) and intercept of Fig. IV-7 and t is taken as the aircraft's arrival time to the cloud's center (for any given pass). A radial standard error for Eq. (4.2) was computed as 0.344 kilometers.

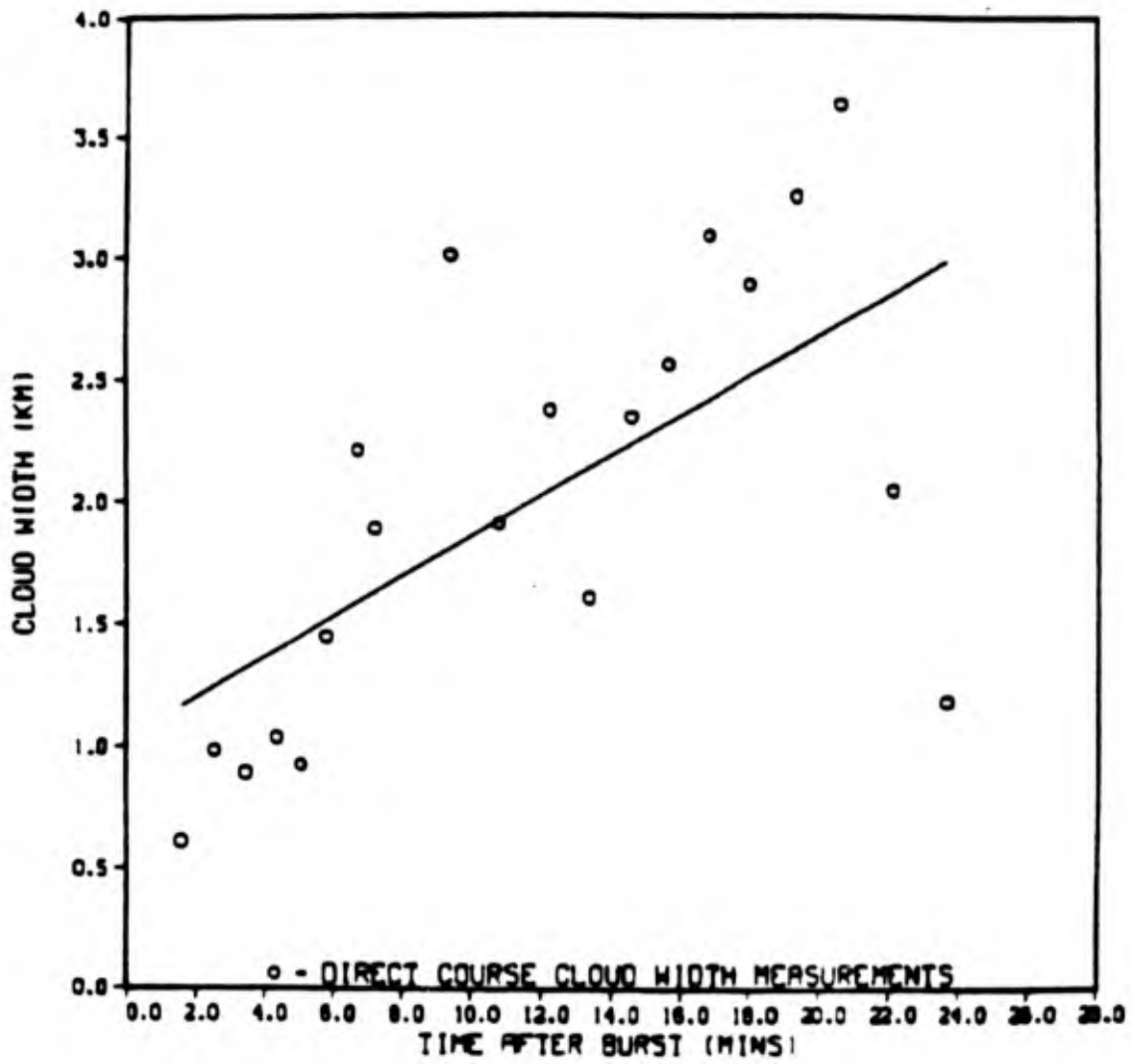


Figure IV-7. Linear regression of measured cloud data with a standard error of 0.688 kilometers.

Symmetry was assumed in the lateral direction because the aircraft's time to reach the cloud's center was taken as half the time used to traverse its diameter. This implies that

$$\sigma_x = \sigma_y = \sigma_c \quad (4.3)$$

where σ_c is the lateral standard deviation of the normalized gaussian distribution. The lateral standard deviation in terms of R from Eq. (4.2) is

$$\sigma_c = R \quad (4.4)$$

This concludes the development of cloud parameters peculiar to HE tests. Nuclear and HE generated dust clouds use the same modeling techniques to predict the spatial distributions and the fall mechanics of the generated trace particles so these techniques will not be repeated in this chapter (given in chapter III).

Mass Fraction Distribution

Mass histograms were chosen as the comparison for Direct Course analysis because extensive data of mass loadings per pass, mass solid density (2.3 gm/cc) and the total mass budget resulting from passes through the cloud were best determined from Direct Course experimental results. In order to get REDRAM predicted results in units of the mass histograms obtained in the DNA report (gm/m³-μm), mass fraction per micrometer of dust particle diameters characteristic of distributions of the test site soil was made. Zimmerman derived an eighth-order polynomial fit of the test site soil in units of mass fraction per micron of particle diameter. It is given as

$$\begin{aligned} \text{Ln}(\Delta M(d) / \Delta d) = & -2.7973914 - 3.3879049 x + 6.1365564 x^2 - 5.5195742 x^3 \\ & + 2.3597698 x^4 - 5.333146 x^5 + .0655594 x^6 \\ & - .0041489 x^7 + .0001059 x^8 \end{aligned} \quad (4.5)$$

where $x = \text{Ln}(d)$

d = particle diameter (micrometers)

$\Delta M(d) / \Delta d$ = mass fraction per micron

Detailed derivation of Eq. (4.5) is found in Appendix B.

REDRAM output is in the form of volumetric cells. Each cell contains a fraction of the 3-D normalized gaussian spatial distribution of a desired quantity of interest (mass) for specific trace particles (particles remaining at a given freeze frame time). The units of the cellular output are given as

$$n = \left(\frac{1}{\text{radians}} \right)_{\text{LAT}} \left(\frac{1}{\text{radians}} \right)_{\text{LONG}} \left(\frac{1}{\text{meters}} \right)_{\text{ALT}} \quad (4.6)$$

where n is the 3-D normalized cell value from Eq. (3.17), inverse radians are the lateral dimensions for the latitudinal and longitudinal directions and inverse meters represent the vertical gaussian distribution. Converting the units of (4.6) into metric inverse volumes, n_c , requires

$$n_c = a \cdot b \cdot c \cdot d \cdot e \cdot b \cdot c \cdot f = 2.97 \times 10^{-14} \text{ m}^{-3} \quad (4.7)$$

where a = inverse distance of latitude in radians⁻¹

b = ($\pi/180$) radian-to-degree (inverse) conversion

c = (degree/111 km) degree conversion per the earth's radius at the equator

d = $\cos(33.624)$ latitude correction for the ground zero latitude coordinate

e = inverse distance of latitude in radians⁻¹

f = inverse distance of altitude in meters⁻¹

The flight path integrated average density function, \bar{n} , is approximated as

$$\bar{n} = \int_{\text{Path}} n \, dl / \int_{\text{Path}} dl \quad (4.8)$$

where the denominator of (4.8) is the total number of cells used in the integration of the numerator.

Using the results of Eqs. (4.5), (4.7), and (4.8) allows the mass density distribution function, $m(d)$, to be defined as

$$m(d) = T_m \cdot \bar{n} \cdot n_c \cdot M(d)/\Delta d \quad (\text{gm/m}^3\text{-}\mu\text{m}) \quad (4.9)$$

where T_m is the total mass lofted for the isolated cloud mass (chosen as 1.55×10^8 grams) and is equal to the accumulated mass of Pass 20 (cloud top) minus the accumulated mass of Pass 6 (mass isolating the cloud bottom), and where $M(d)/\Delta d$ is the exponential value of Eq. (4.5).

Equation (4.9) is the final form required to compare in-situ spectrometer results to REDRAM predicted values.

Results

Figures IV-8 through IV-28 give results of mass histograms computed from REDRAM compared to in-situ spectrometer measurements. Figures V-8 through IV-21 yield the mass density distribution functions of Eq. (4.9) as functions of particle diameter for the aircraft's ascent through the cloud, and Figures IV-22 through IV-28 give the results for the descending passes.

Figure IV-29 contains the spatial center coordinates of REDRAM predicted cloud centers compared to actual flight data of Table IV-3.

Statistical Comparison

Table IV-7 contains the fractional error for all mass histograms (Figures IV-8 through IV-28) as a function of channel particle size. Fractions greater than one result in an overprediction of mass sizes compared to actual data and fractions less than one indicate underpredicted results.

Absolute errors for the west and north transport directions (for ascending passes) are given in Table IV-8. The absolute average error for the west and north directions is approximately .26 and .98 kilometers respectively.

Table IV-7. Fractional Errors of Computed Direct Course
Mass Histograms for Passes 7 through 27.

<u>Channel #</u>	<u>Particle Size (μm)</u>	<u>Fractional Error</u>
1	5	3.670
2	8	16.89
3	12	120.20
4	16	25.51
5	20	6.127
6	24	24.38
7	28	23.51
8	32	22.59
9	36	31.39
10	40	31.59
11	44	27.33
12	48	27.14
13	52	27.19
14	56	27.06
15	60	28.52
16	80	24.34
17	105	14.64
18	129	4.966
19	154	2.415
20	178	1.090
21	203	.7715
22	229	.7034
23	253	.6390
24	277	.4445
25	301	.5211

Table IV-8. Absolute error of the cloud center axis
for the west and north components.

<u>Pass #</u>	<u>Error in West Direction (km)</u>	<u>Error in North Direction (km)</u>
7	1.38	1.47
8	.572	1.70
9	.441	1.44
10	.052	.022
11	.294	.100
12	.001	.928
13	.173	.905
14	.244	1.07
15	.033	1.28
17	.034	.88
18	.034	.87
19	.283	1.48
20	.072	1.42

Discussion and Summary

The spectral wind model predicted accurate mass densities as seen in-situ by spectrometers (Figures IV-8 through IV-28). REDRAM underpredicts aircraft mass histograms across the full particle range for Passes 7 and 8. These differences in mass histograms might be explained by the fact that pseudo masses (densities greater than 2.3 gm/cc) such as chaff fragments and fiberglass strands are detected by the mass spectrometers but are not accounted for in REDRAM because REDRAM only modeled

mass fractions characteristic of the test site soil. As time goes on, these pseudo masses fall out faster than the characteristic soil particles, thereby leaving mass densities more representative to soil masses. These "representative" soil mass densities are best depicted in Figures IV-10 through IV-28 where the pseudo masses have fallen out of the cloud. Pass 20 (Fig. IV-21) yielded a poor in-situ measurement because there were very few particulate masses at the cloud top. This resulted in poor statistics for comparison of this pass.

In general, REDRAM overpredicts small end particle ranges of the mass histograms and underpredicts the large end (see Figures IV-10 through IV-28). As mentioned in the filter analysis section, the falling particles form aggregates which cause the low end particle sizes to shift towards the higher end (as compared to predicted results). Thus, the in-situ (aggregated) detections will see less mass than the nonaggregated REDRAM particles at the small particle size range and more mass at the larger end.

Finally, the larger absolute errors from table IV-8 for the low altitude passes (passes 7 and 8) might be explained as boundary layer transport. As mentioned earlier, the winds within the boundary layer of the earth (1 to 3 kilometers high) are not very accurate. Passes 7, 8, and 9 are less than or equal to 3 kilometers in altitude and thus might be within the earth's boundary layer. This would result in inaccurate predictions of the cloud's center axis for these passes. The northern translations in Table IV-8 yielded less accurate predicted northern locations of the cloud center (compared to the measured centroid) because the northern wind components had small actual wind speeds. The AFGL validation section revealed that small actual wind speeds produced larger wind errors (compared to predicted winds) than large actual wind speeds. This corresponds to the northern translations which had smaller actual winds and which predicted less accurate northern locations (average error in north direction is 0.982 km compared to a 0.259 km average error in the west direction).

DIRECT COURSE PASS NUMBER 7

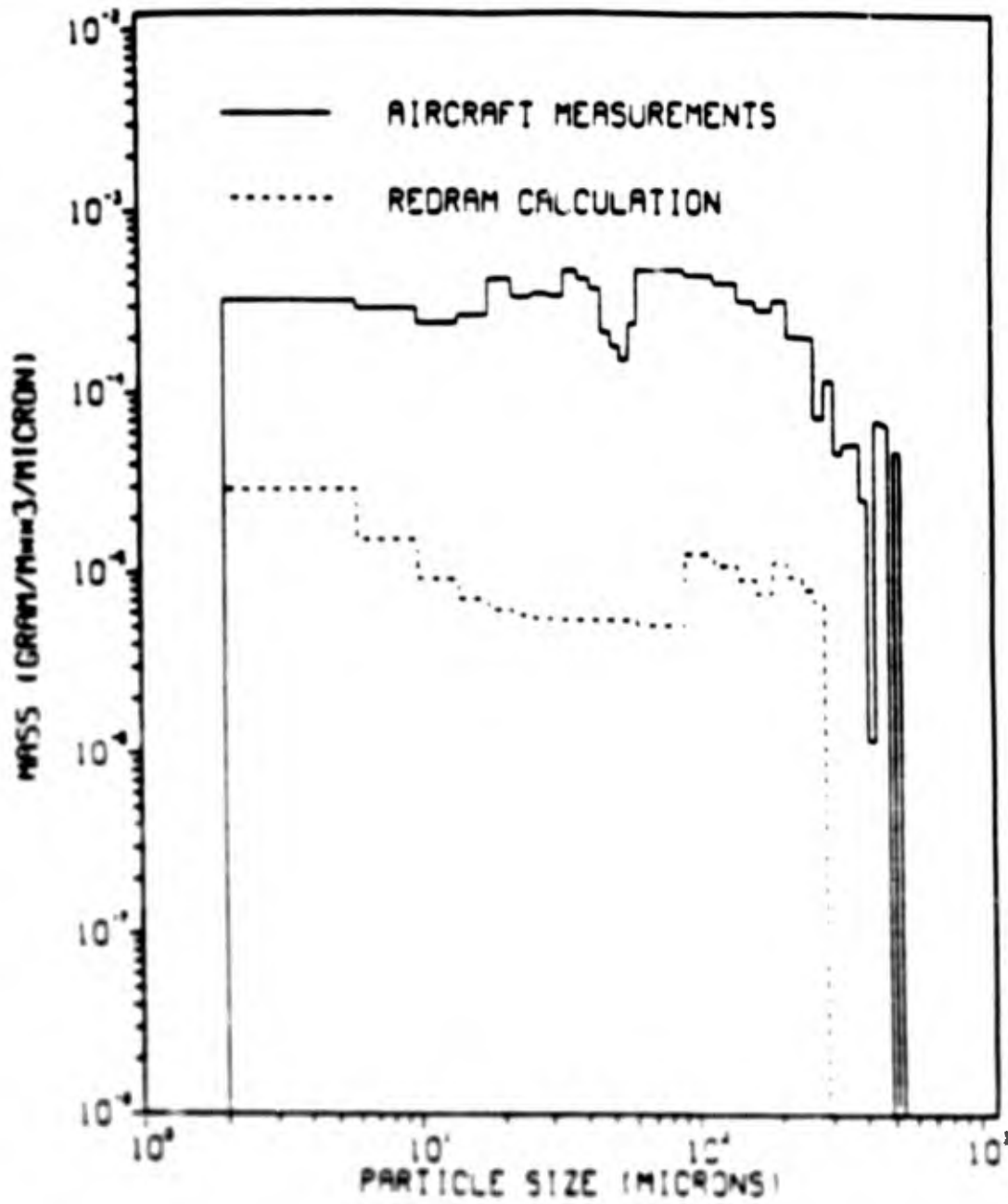


Fig IV-8.

DIRECT COURSE PASS NUMBER 8

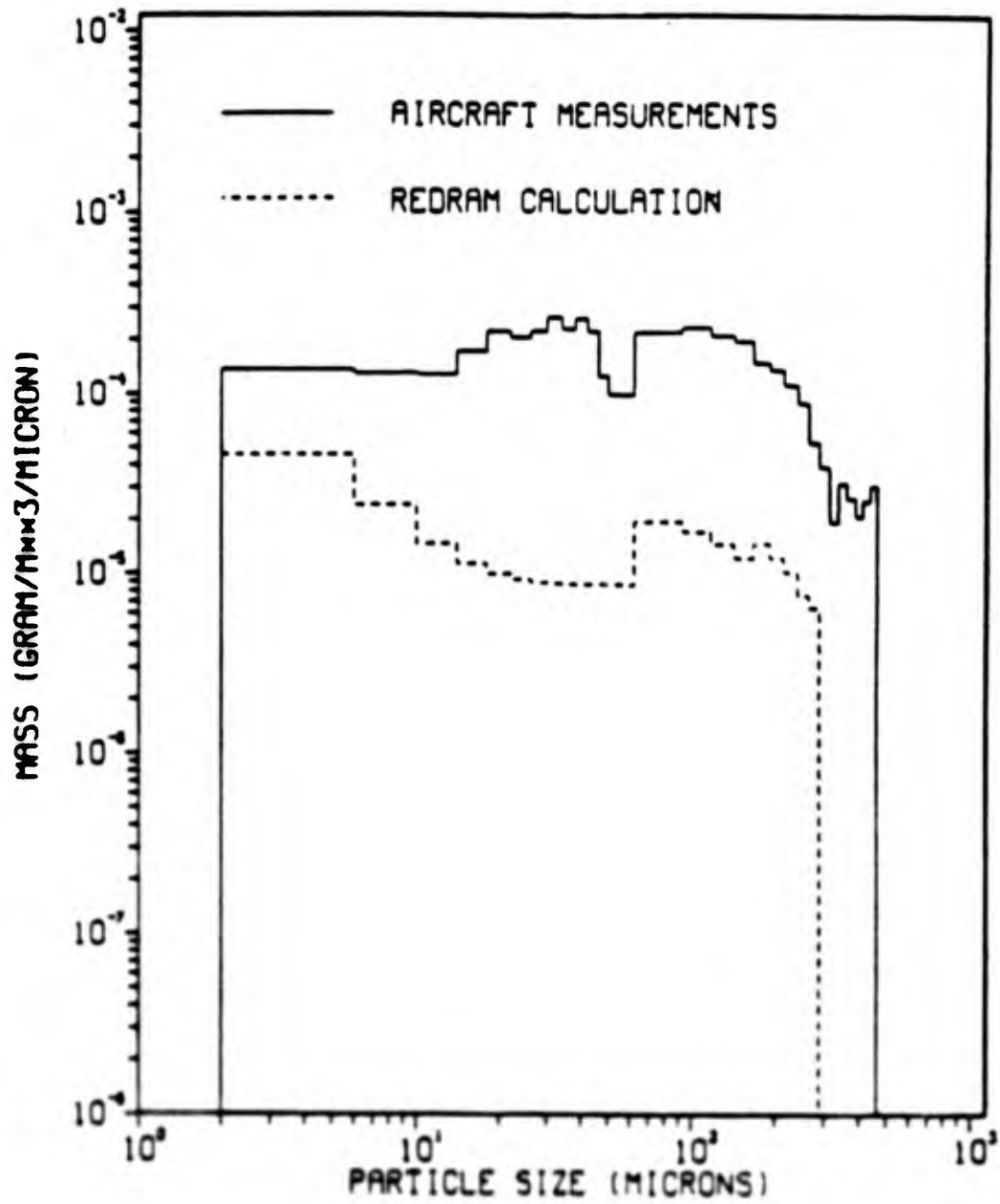


Fig. IV-9

DIRECT COURSE PASS NUMBER 9

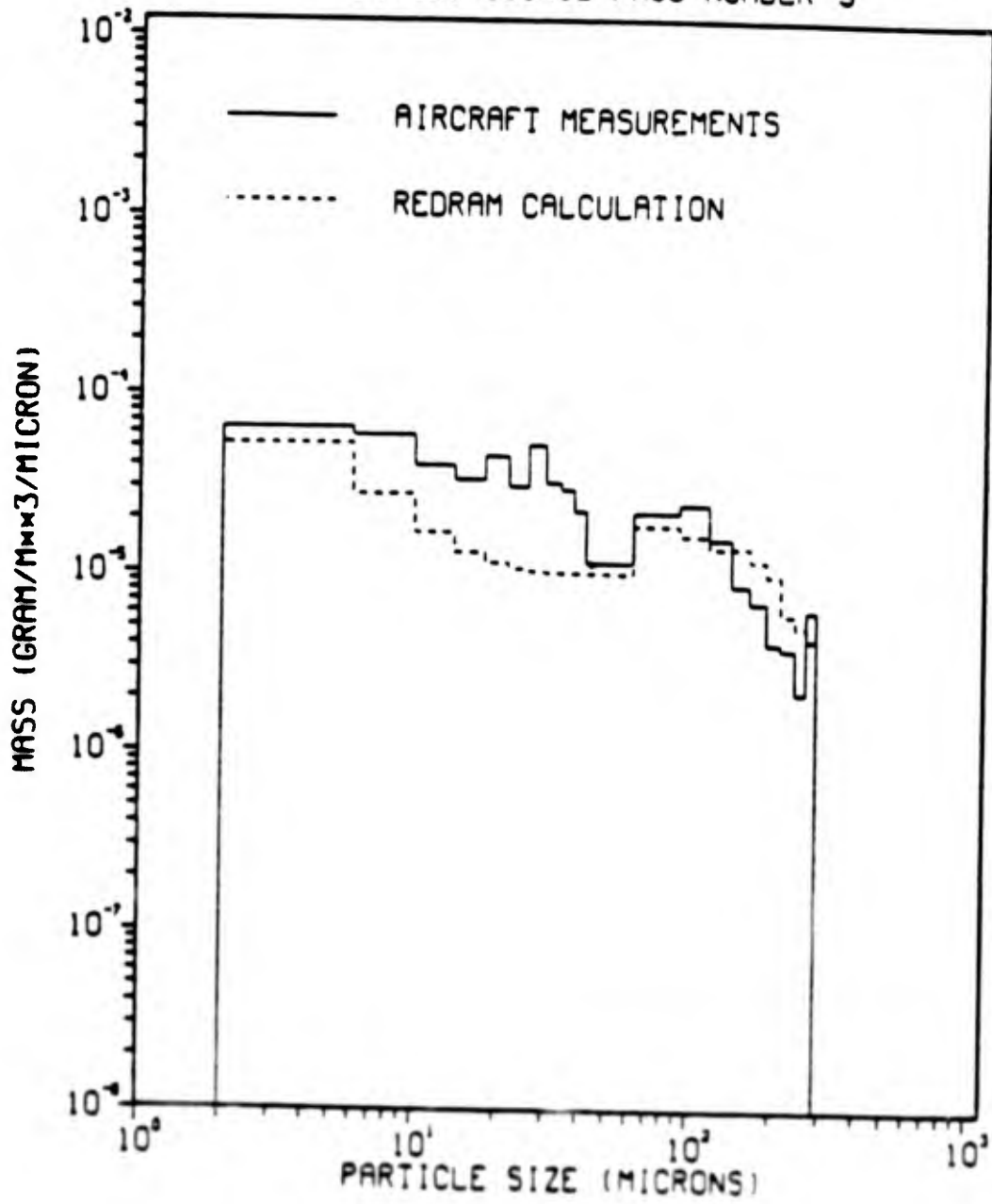


Fig. IV-10.

DIRECT COURSE PASS NUMBER 10

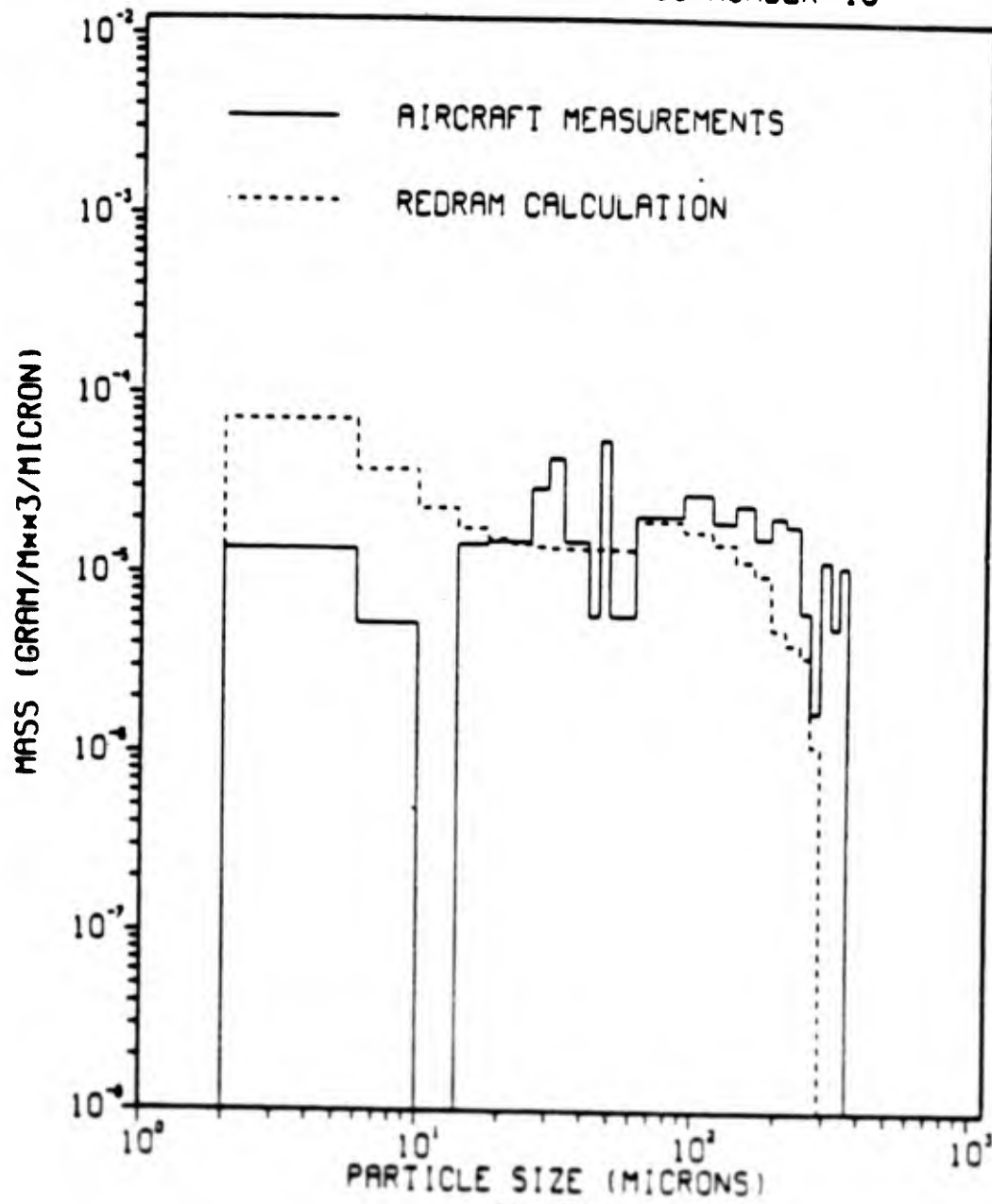


Fig. IV-11.

DIRECT COURSE PASS NUMBER 11

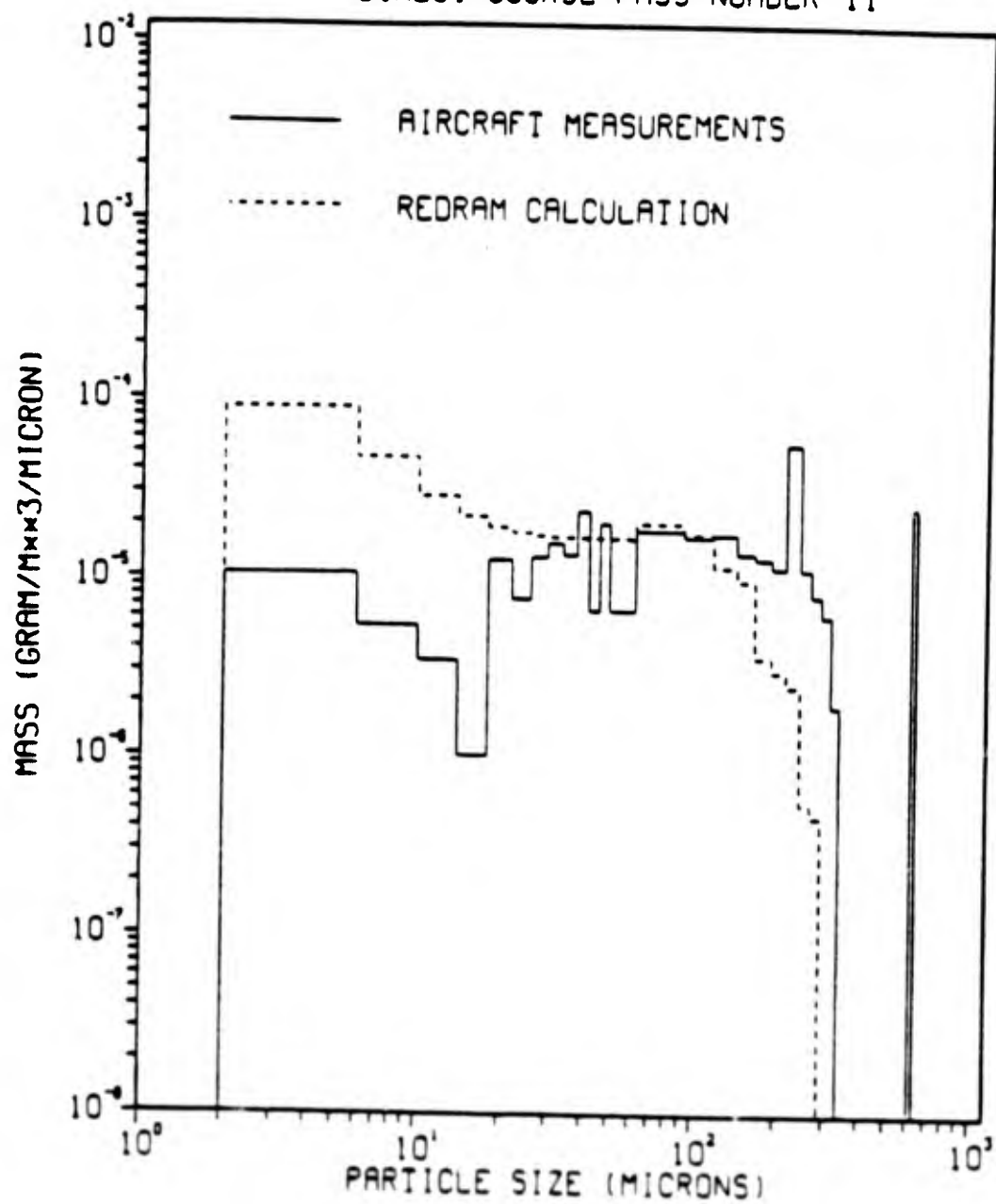


Fig. IV-12.

DIRECT COURSE PASS NUMBER 12

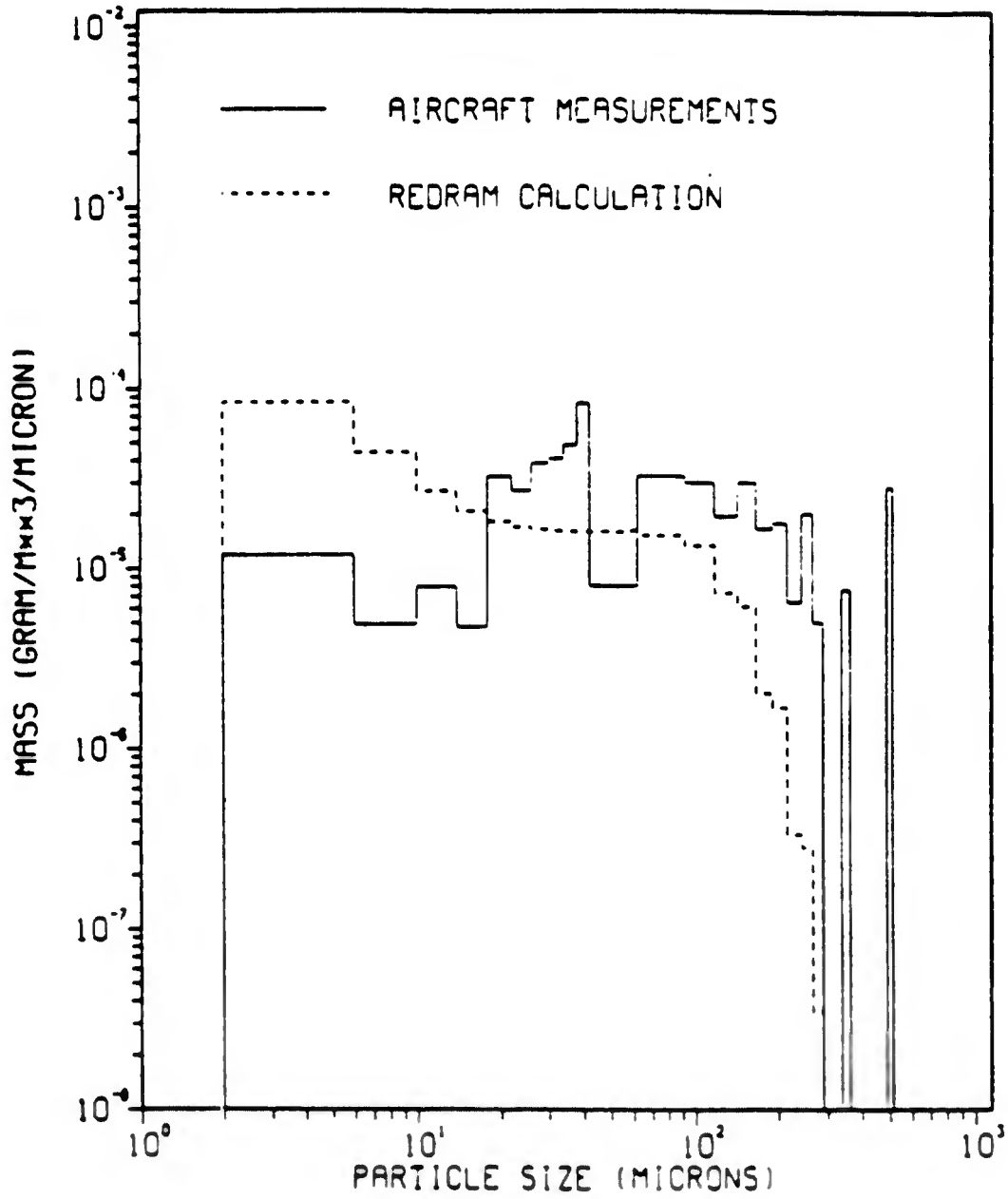


Fig. IV-13.

DIRECT COURSE PASS NUMBER 13

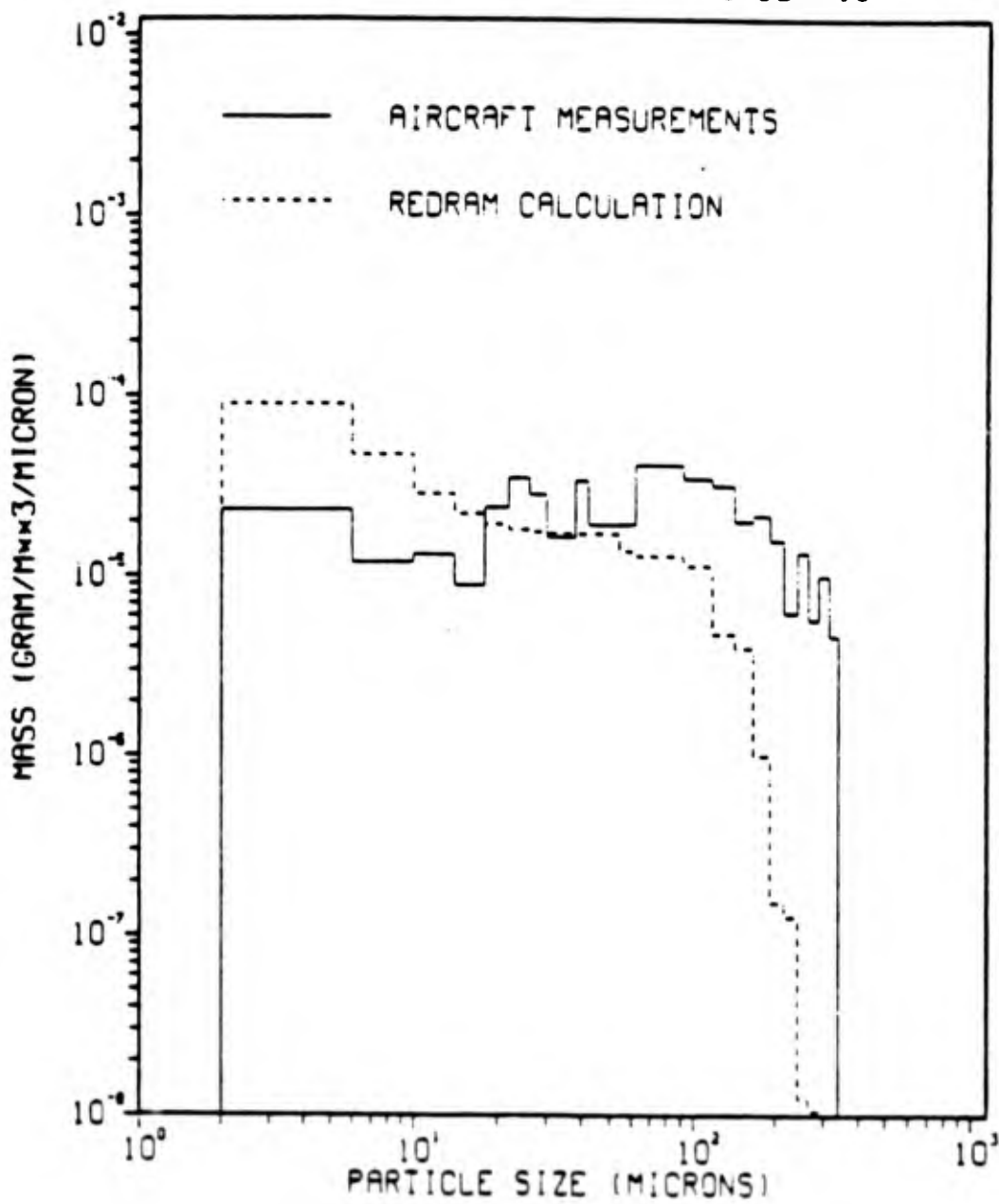


Fig. IV-14.

DIRECT COURSE PASS NUMBER 14

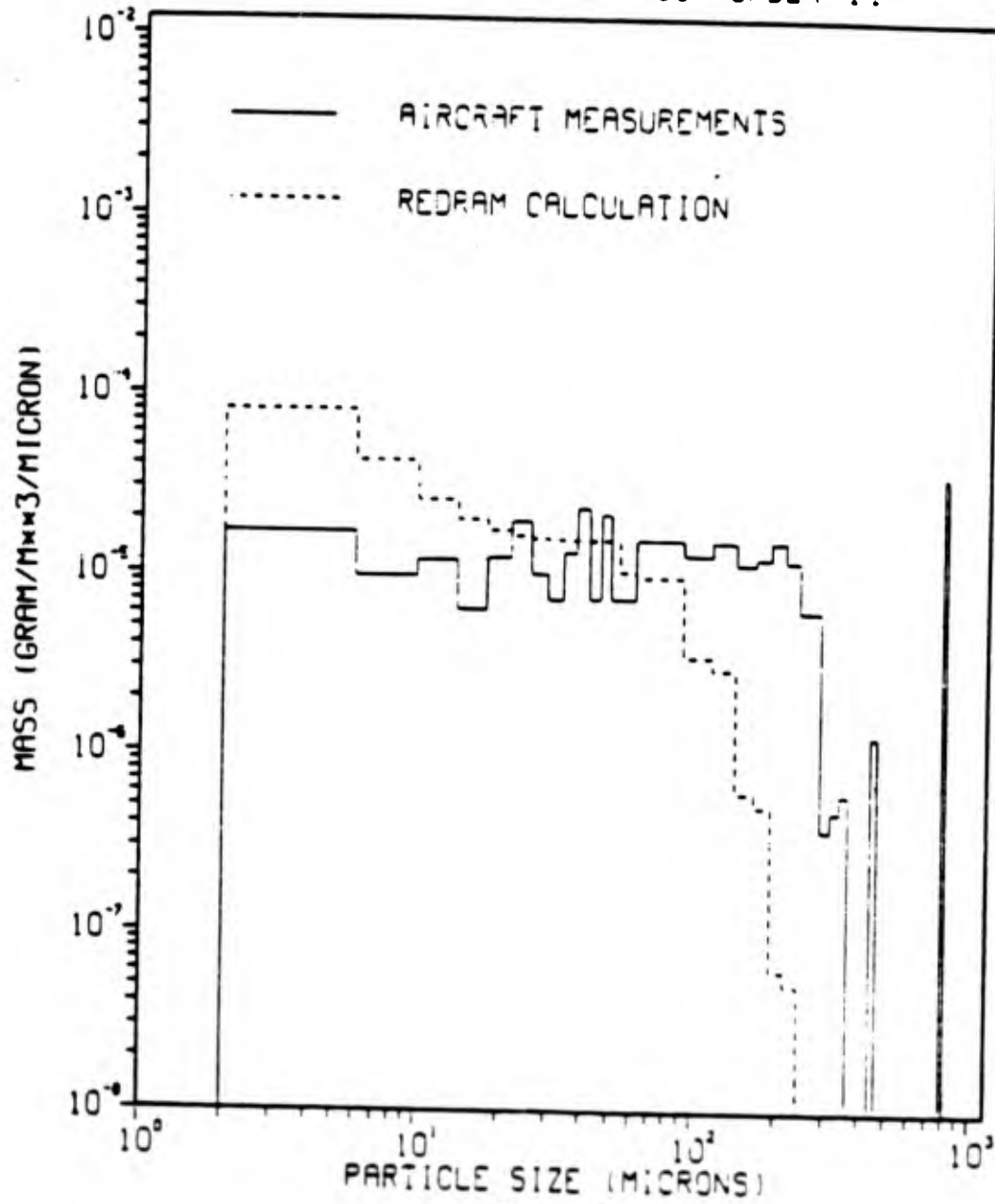


Fig. IV-15.

DIRECT COURSE PASS NUMBER 15

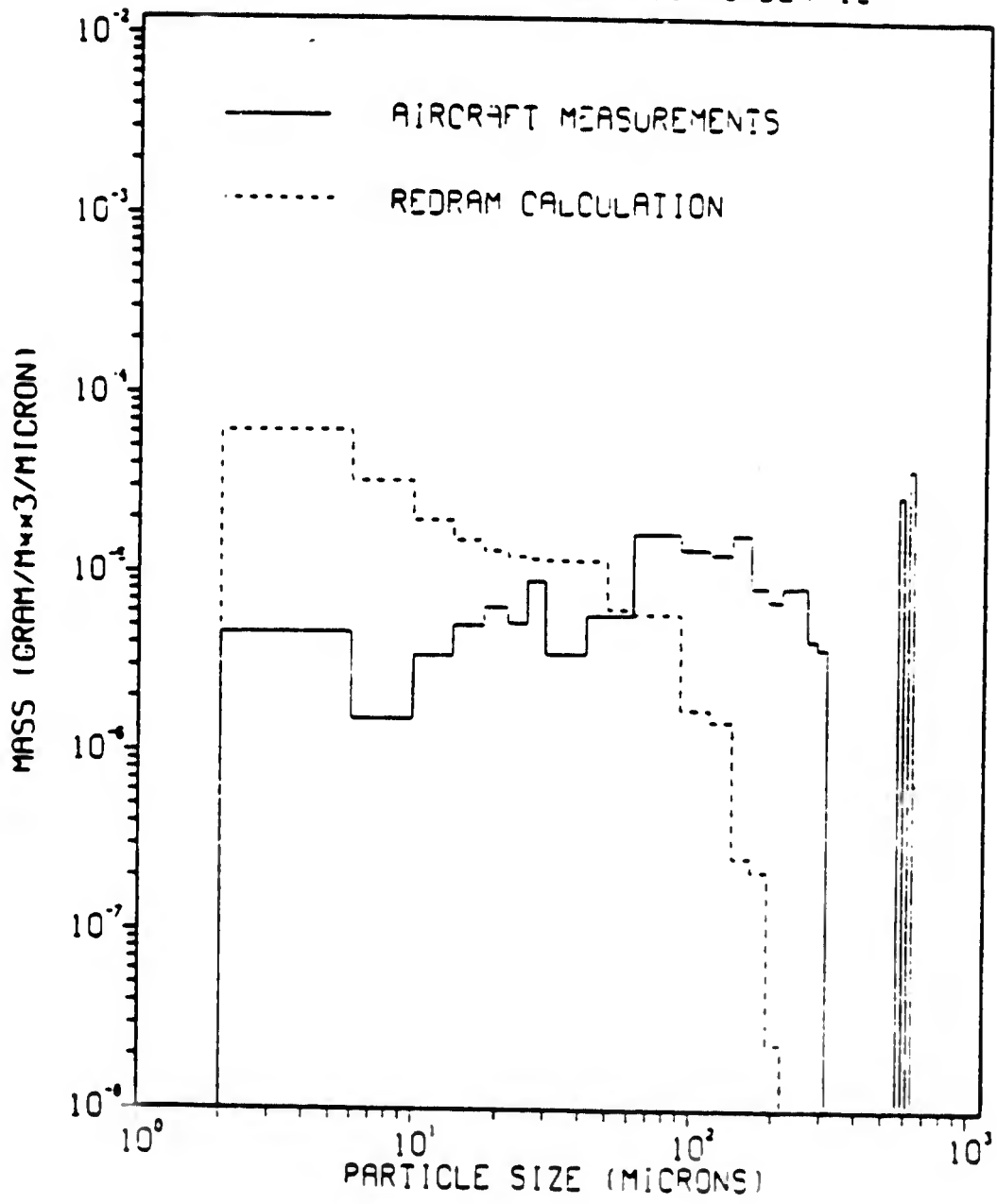


Fig. IV-16.

DIRECT COURSE PASS NUMBER 16

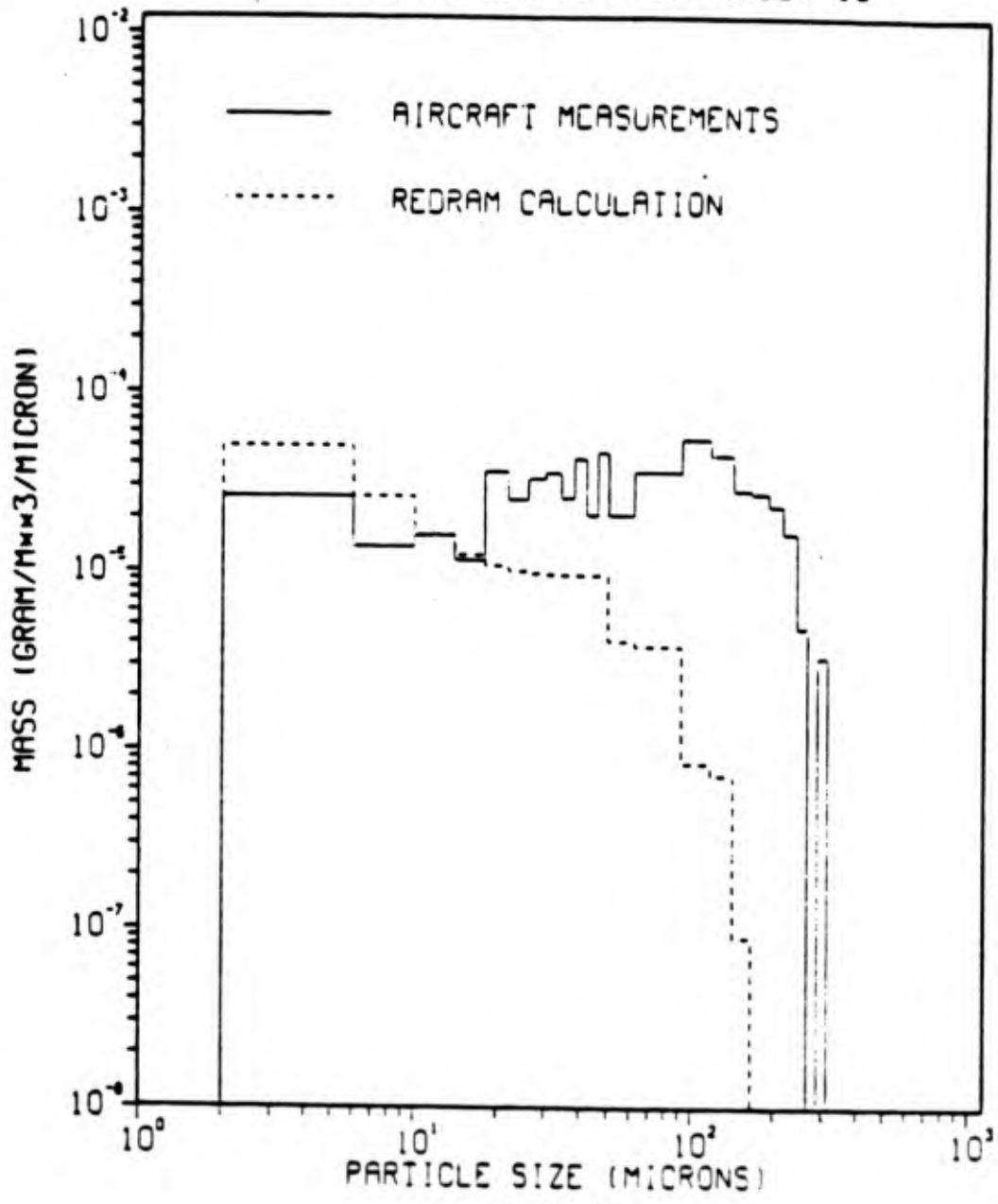


Fig. IV-17.

DIRECT COURSE PASS NUMBER 17

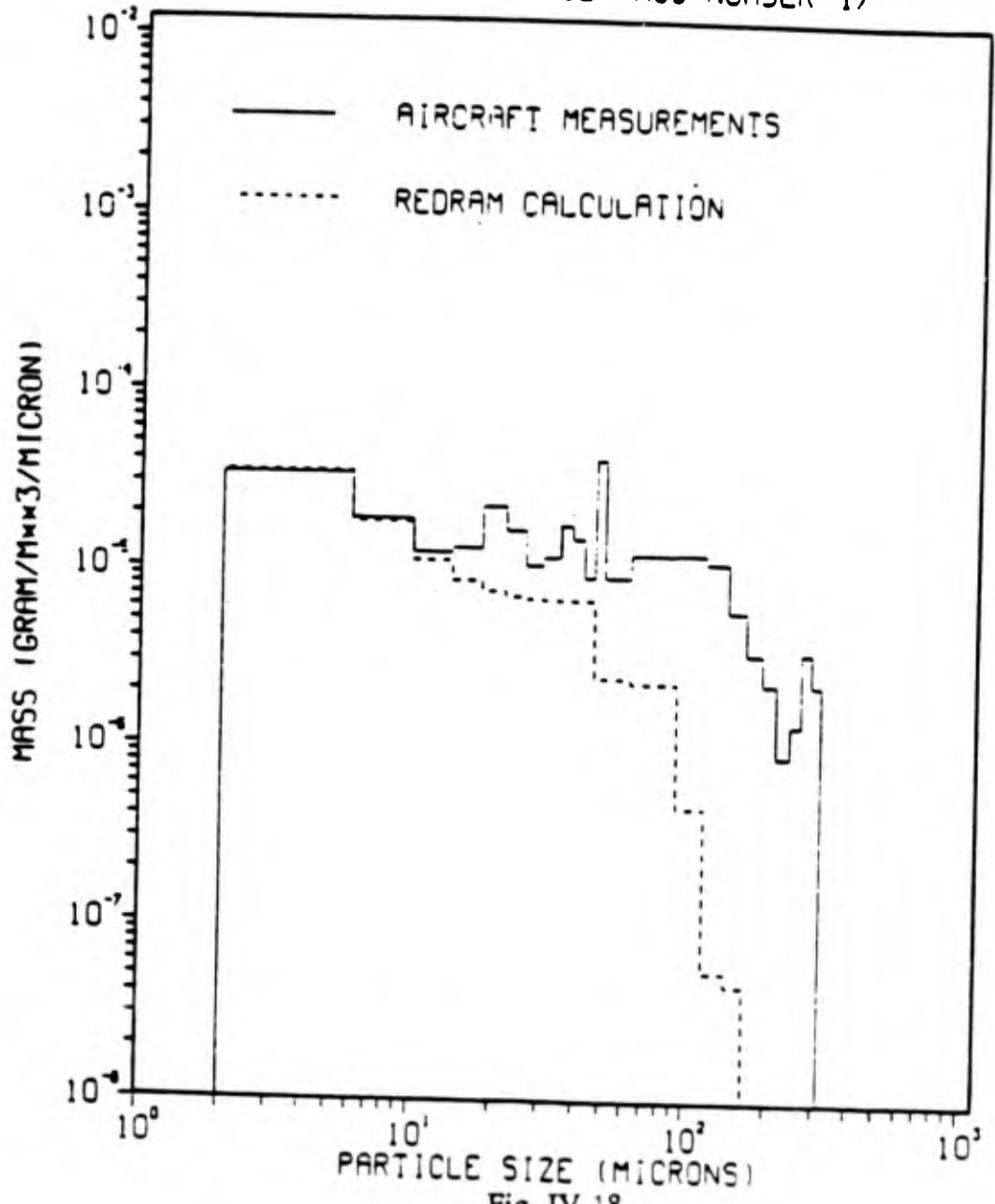


Fig. IV-18.

DIRECT COURSE PASS NUMBER 18

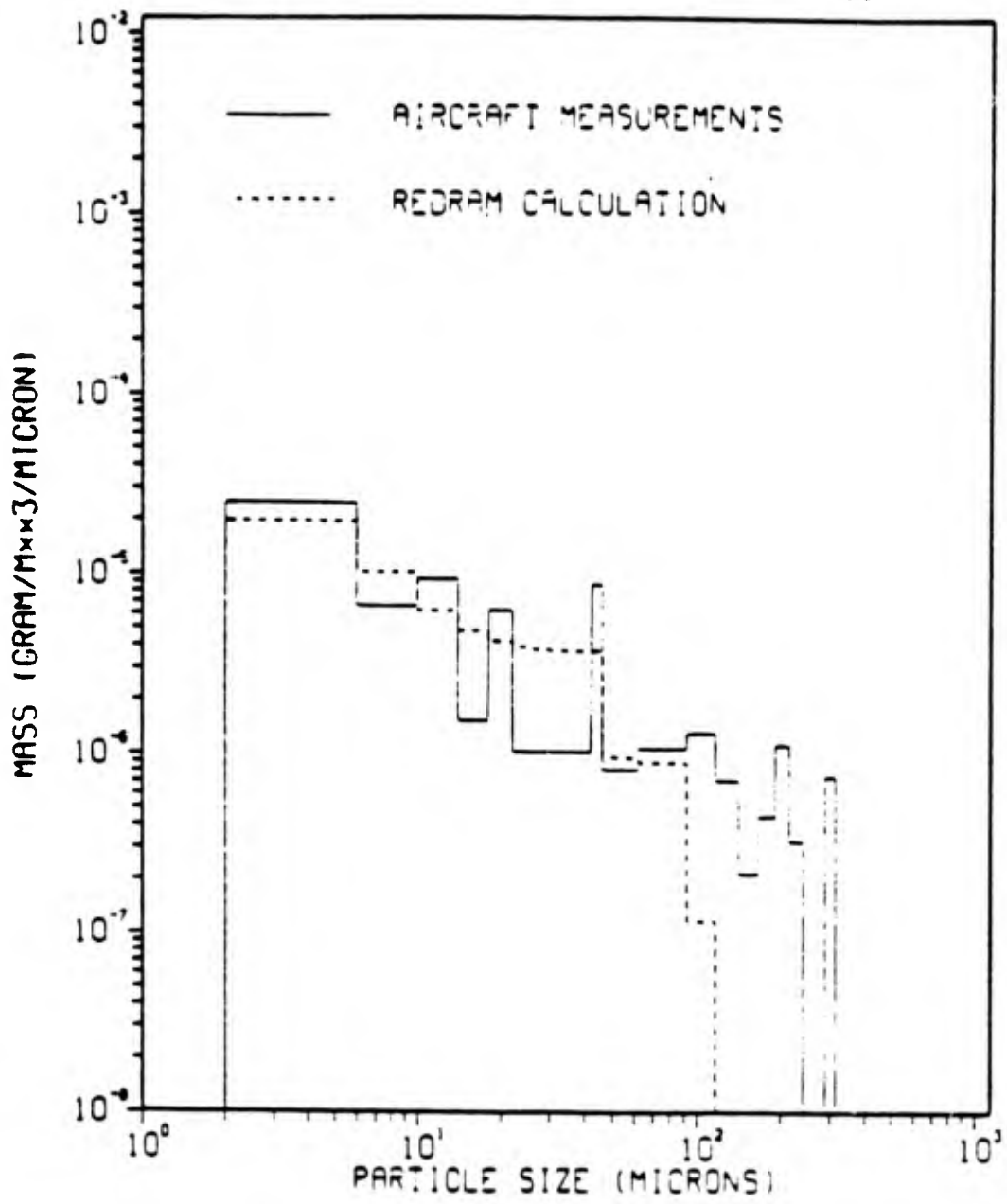


Fig. IV-19.

DIRECT COURSE PASS NUMBER 19

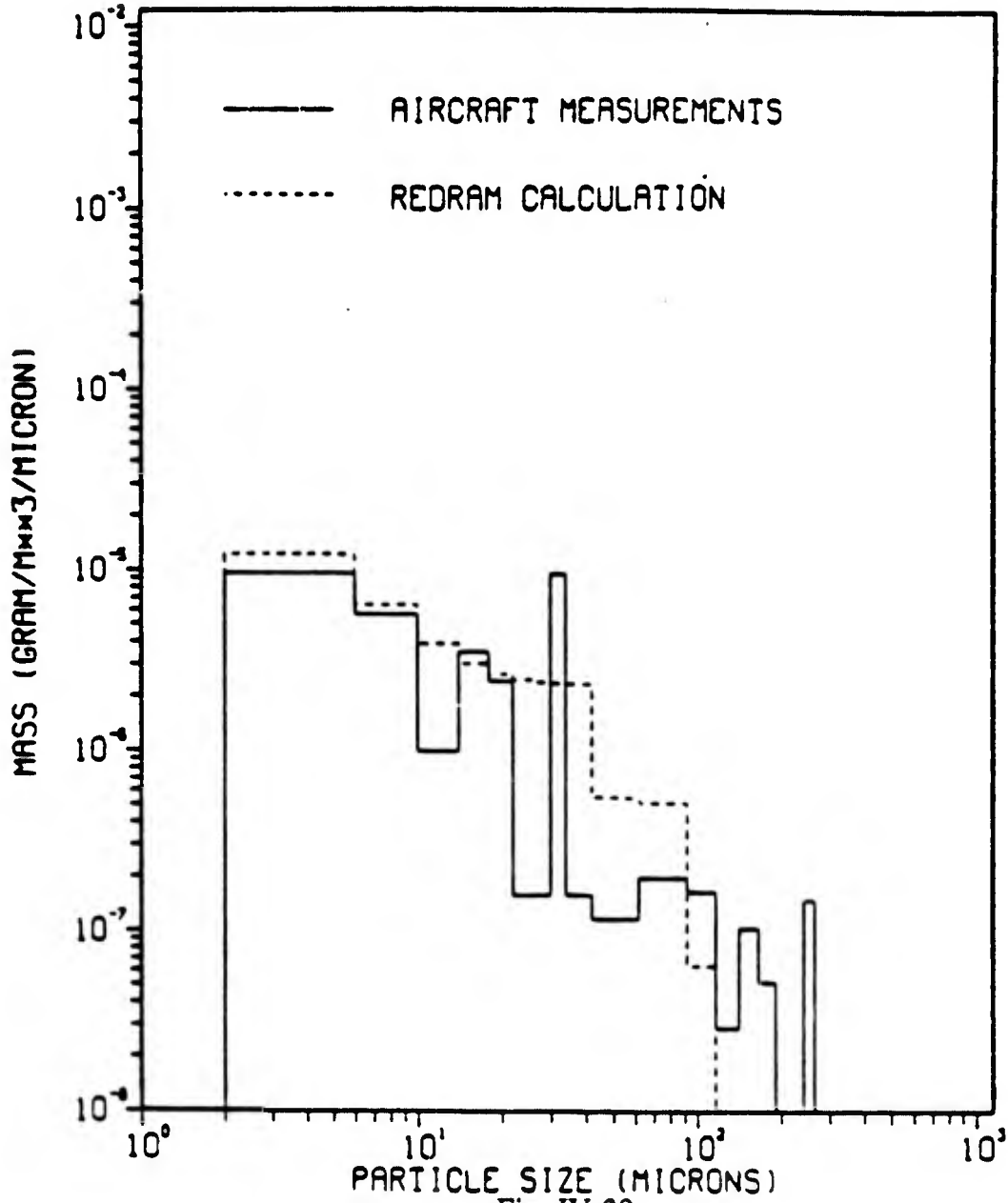


Fig. IV-20.

DIRECT COURSE PASS NUMBER 20

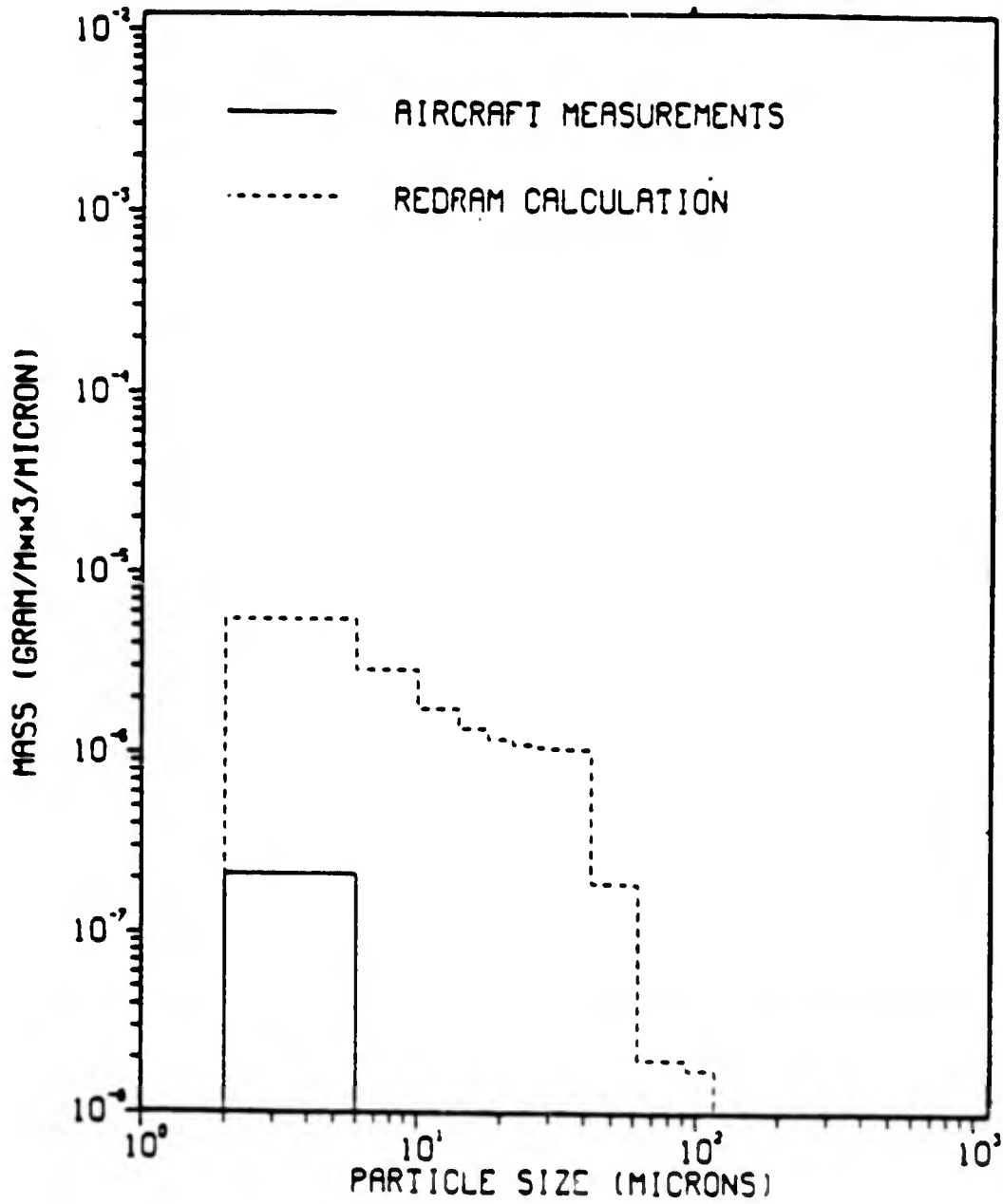


Fig. IV-21.

DIRECT COURSE PASS NUMBER 21

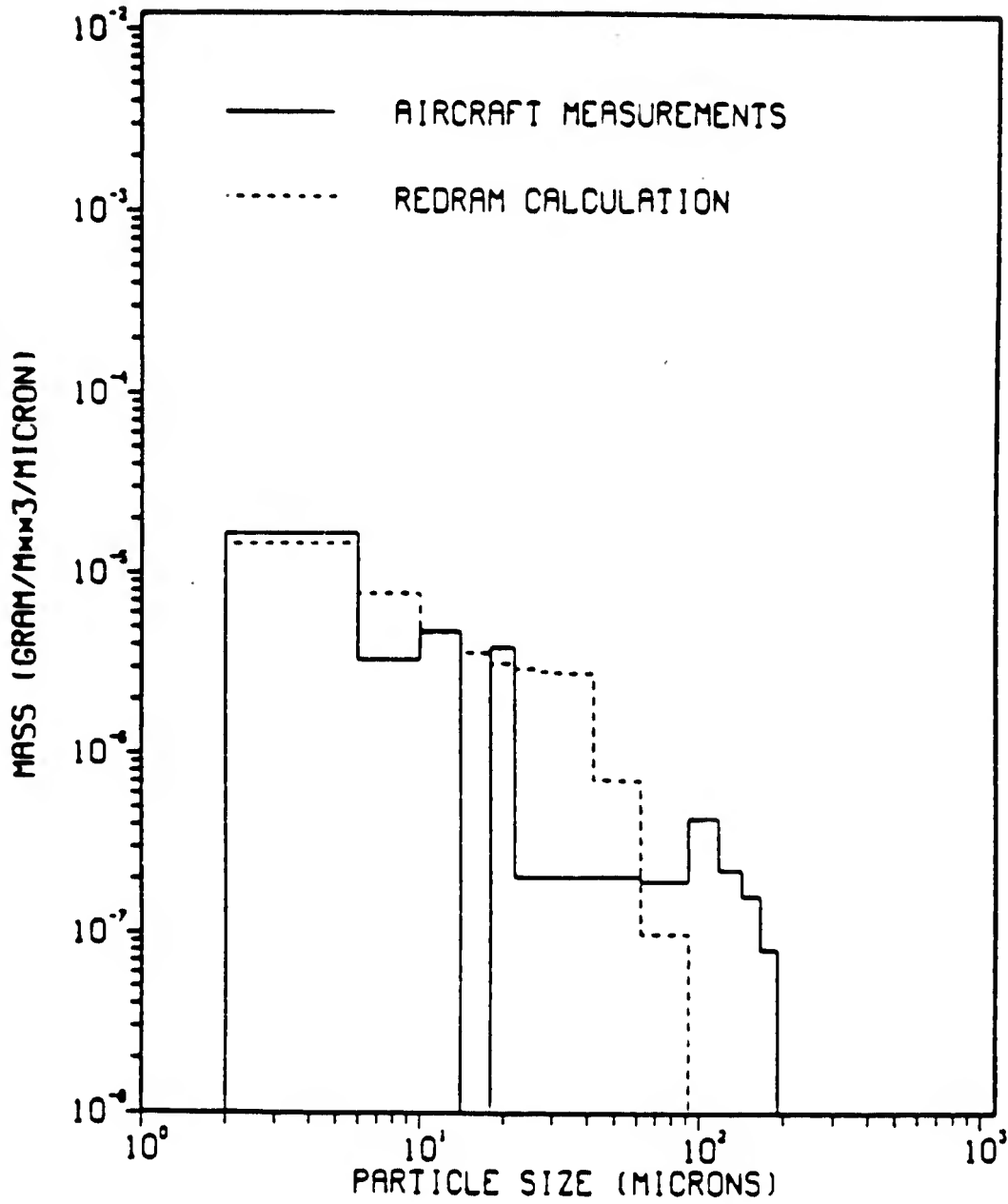


Fig. IV-22.

DIRECT COURSE PASS NUMBER 22

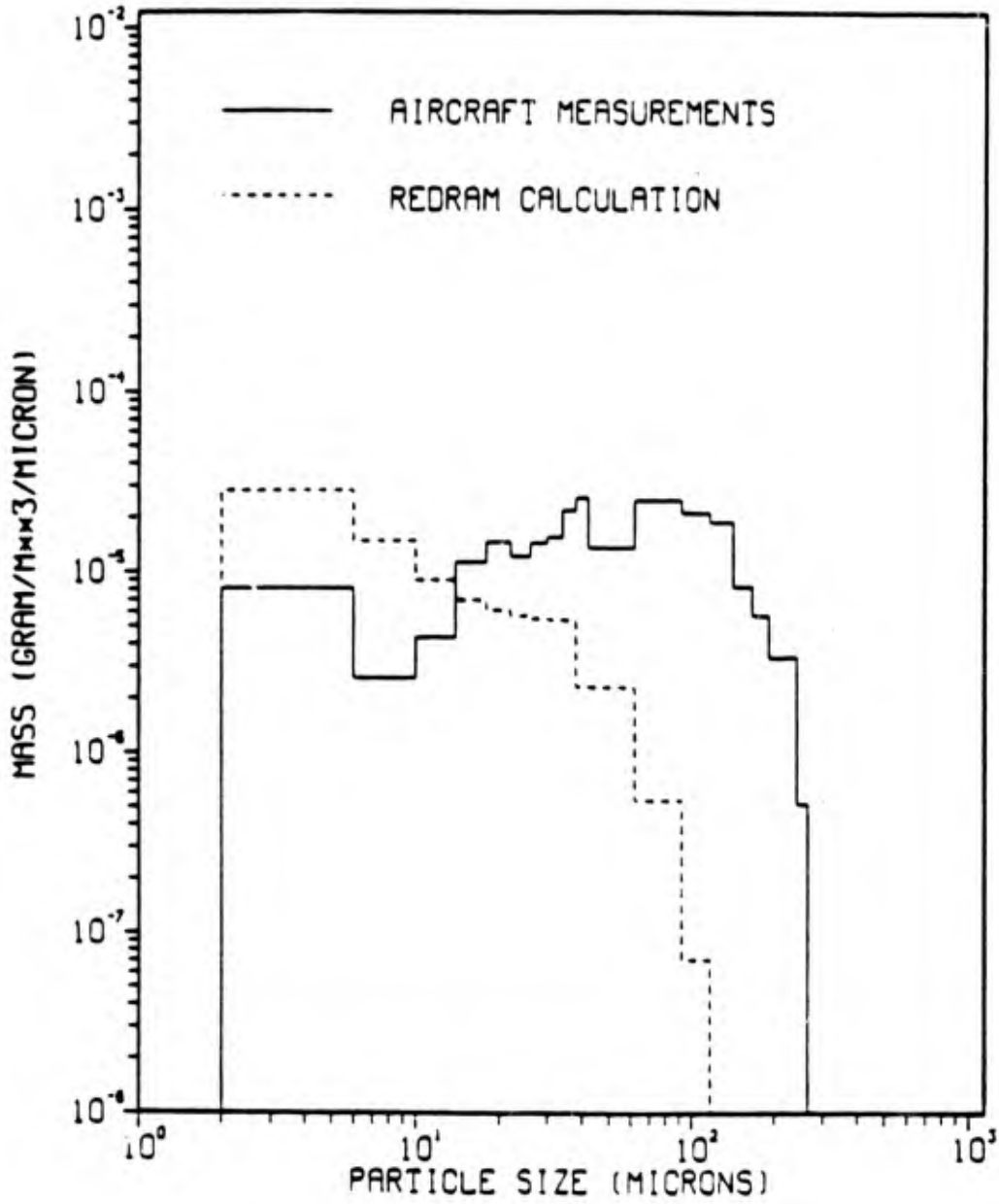


Fig. IV-23.

DIRECT COURSE PASS NUMBER 23

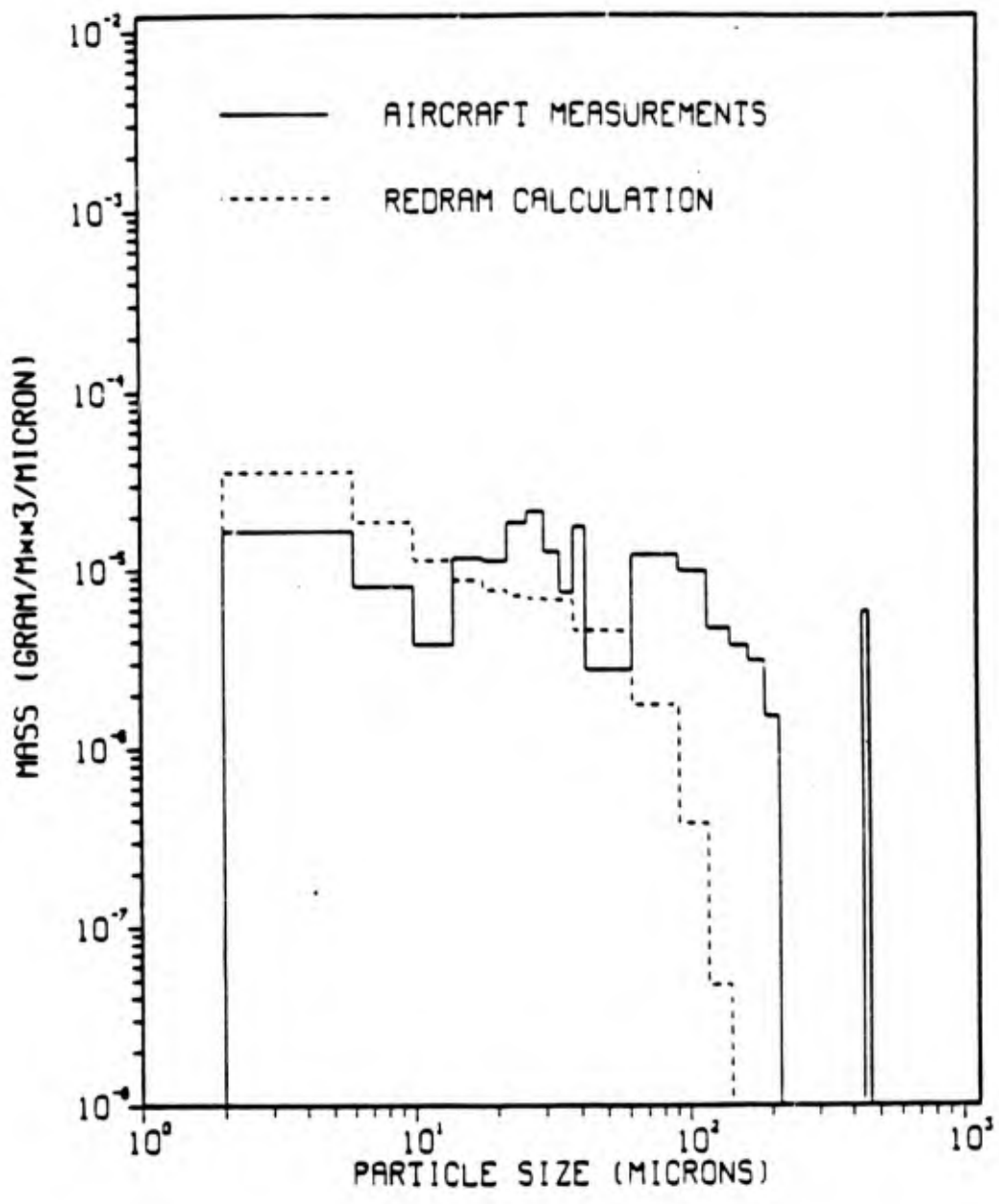


Fig. IV-24.

DIRECT COURSE PASS NUMBER 24

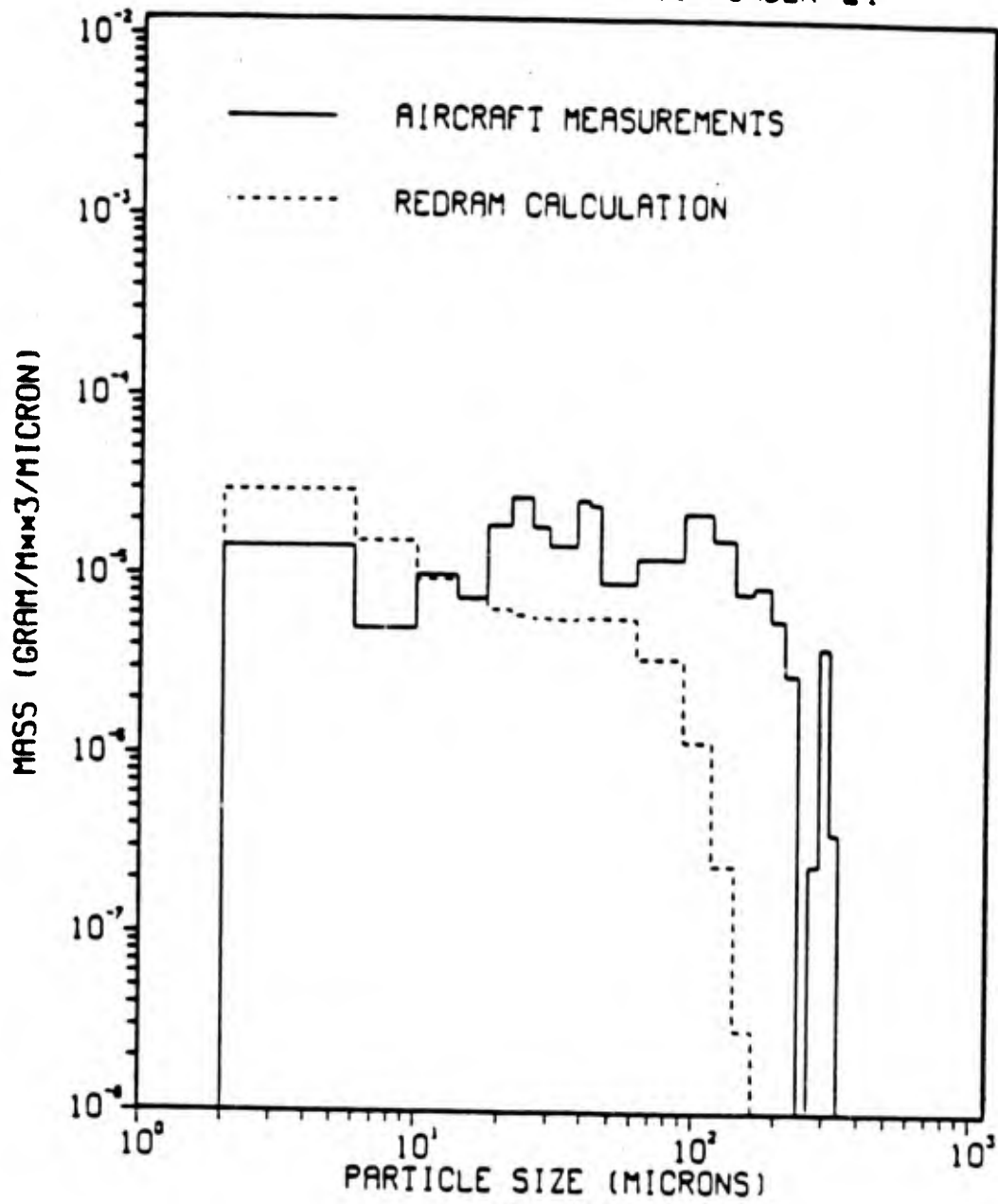


Fig. IV-25.

DIRECT COURSE PASS NUMBER 25

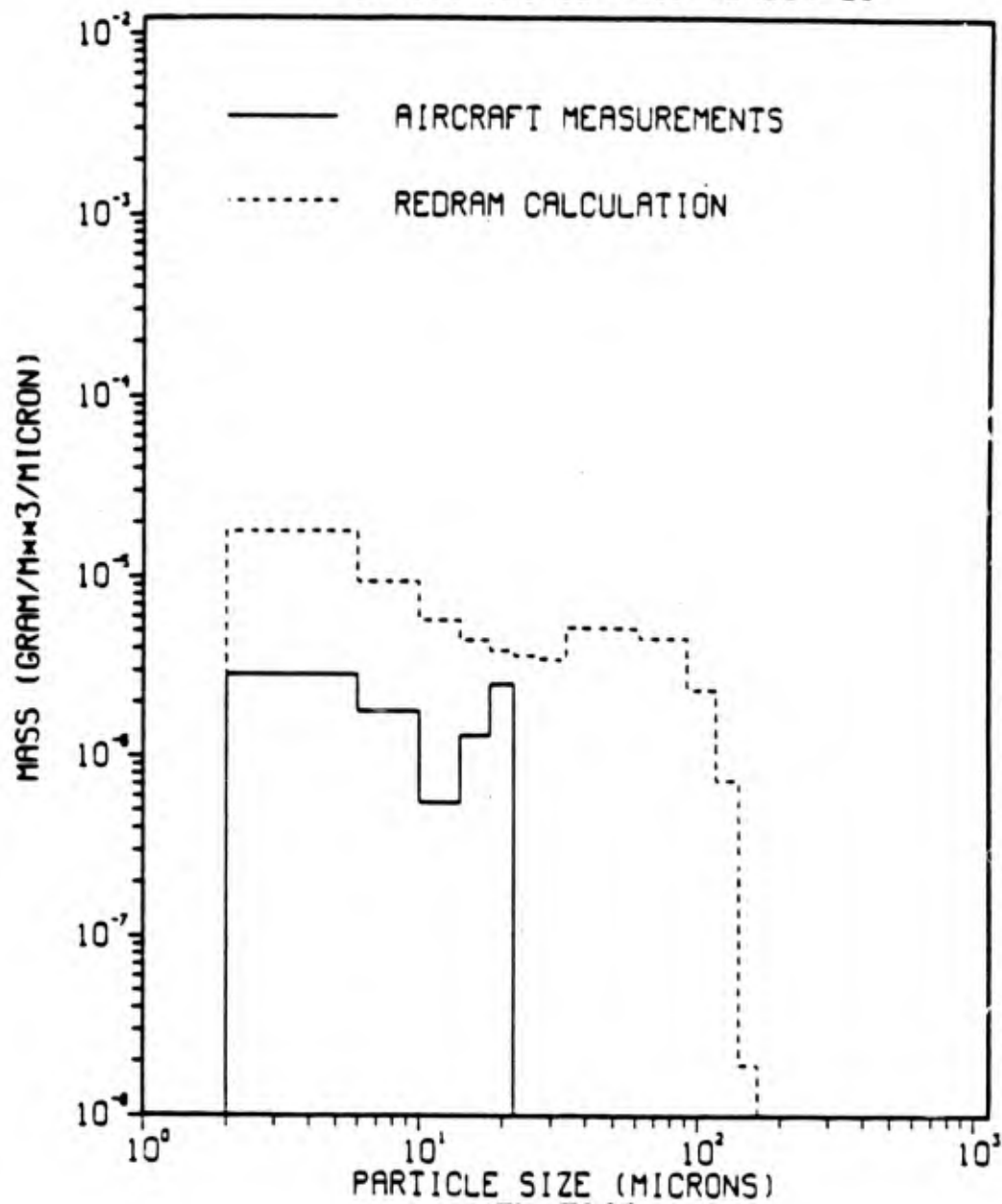


Fig. IV-26.

DIRECT COURSE PASS NUMBER 26

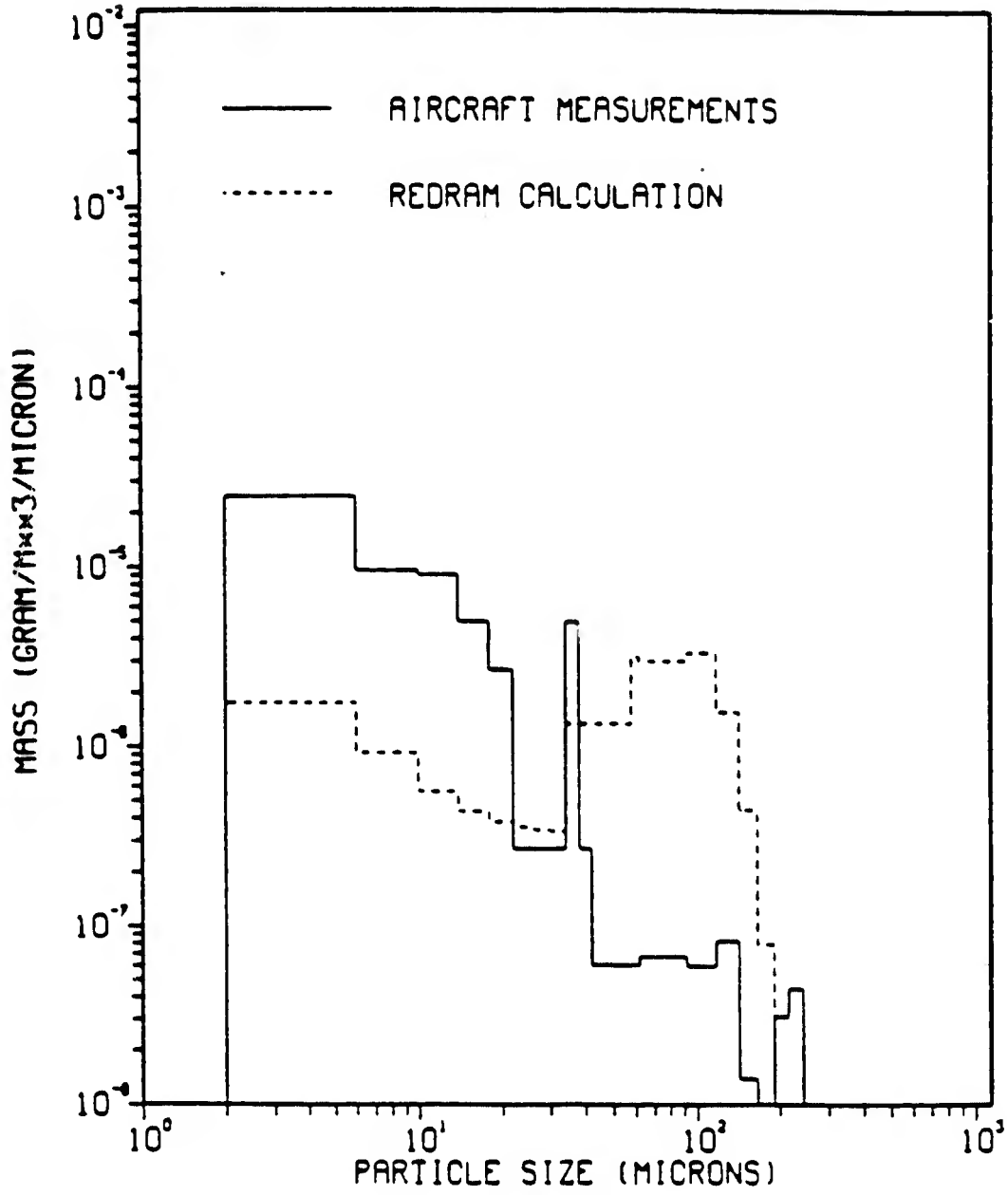


Fig. IV-27.

DIRECT COURSE PASS NUMBER .27

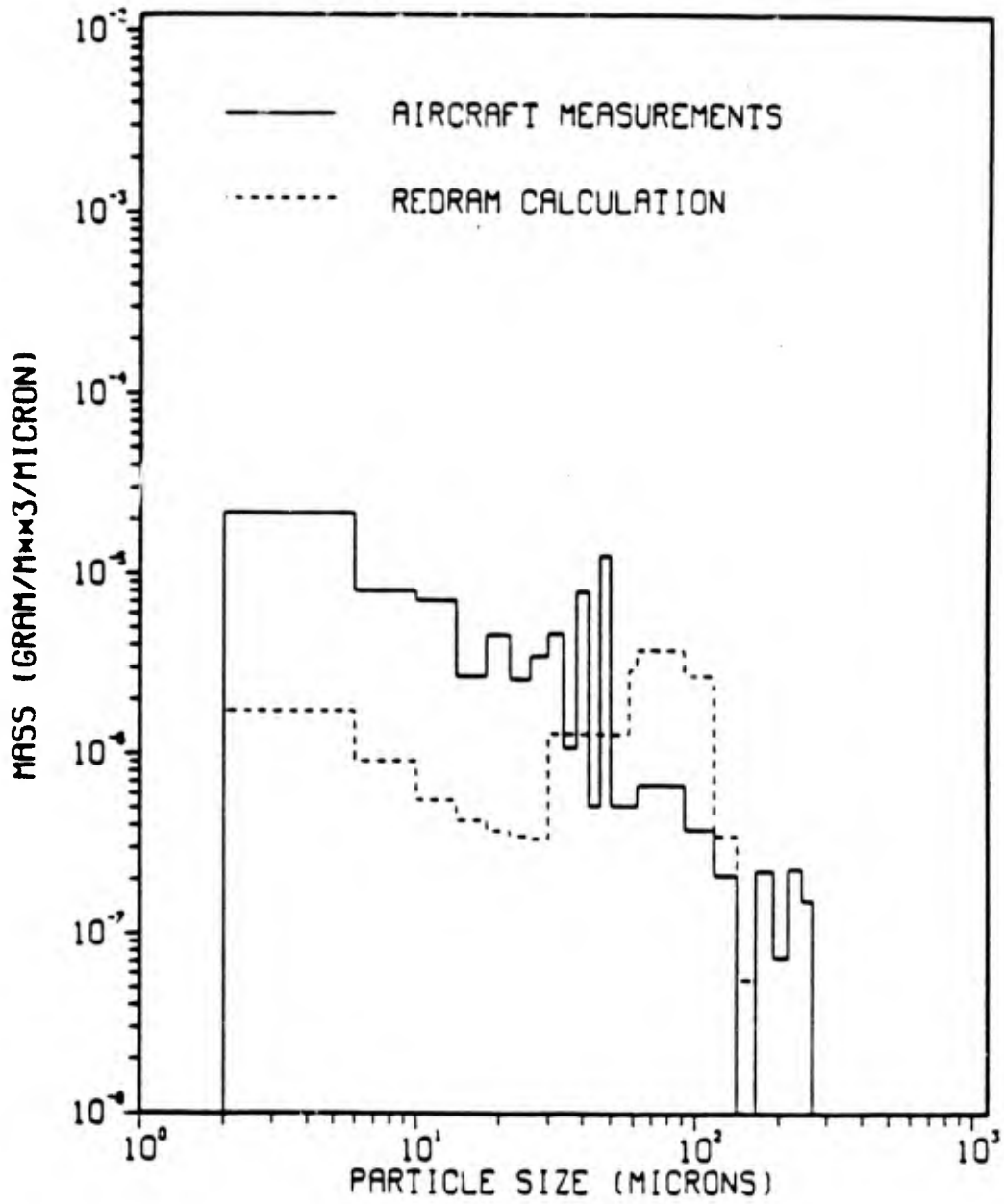


Fig. IV-28.

CLOUD CENTERS FOR PASSES 7 THROUGH 20

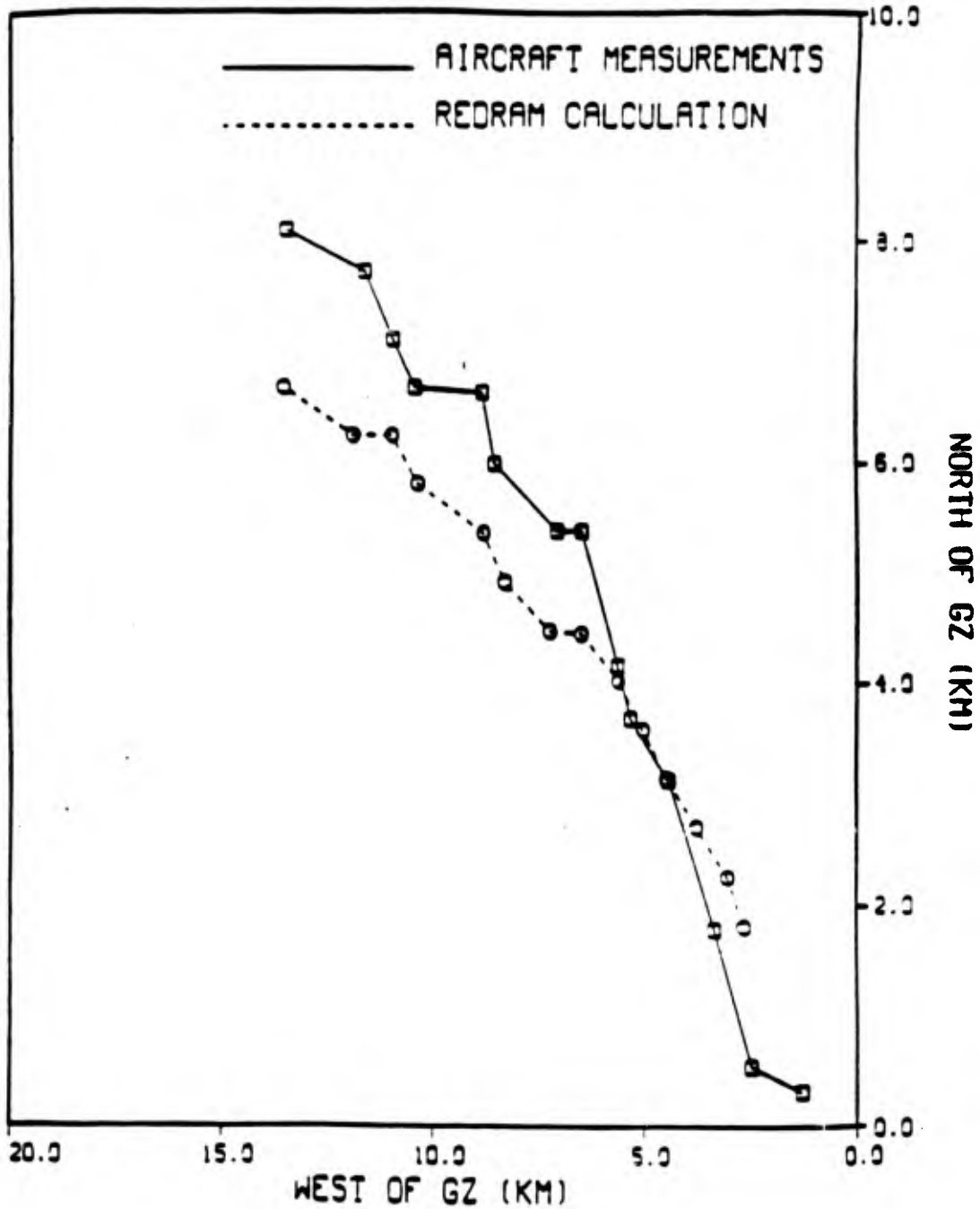


Figure IV-29. Direct Course cloud center plot on a distorted axis. Absolute average error for the west component is 0.259 kilometers and for the north component is 0.982 kilometers.

V. Summary, Conclusion and Recommendation

This chapter summarizes the results and conclusions of this analysis. A modified spectral wind fallout model was applied and validated using actual airborne data generated from a high explosive dust cloud. The calculated results generally matched the observed data as shown in figures IV-8 through IV-28. The significance of the results showed the feasibility of using global spectral coefficients in a fallout model to accurately predict particle transport.

Spectral Coefficient Wind Generator

Modeling equations of global atmospheric flow were presented to gain better understanding of how spectral coefficients are generated. Fast Fourier transforms were applied to spectral-physical space computations to more efficiently derive the spectral coefficients. Thirty wave rhomboidal spherical harmonic truncations produced high-resolution spectral predictions. These predictions were validated against actual data derived from radiosonde fits. The results produced accurate winds at locations 10° latitude from the poles and showed better accuracies for higher speed winds than for lower speed winds (~ 1 m/sec).

Particle Transport Using Spectral Winds in a Hotline Locator Model

Computed spectral coefficients were used to derive global spectral winds in the modified AFIT fallout model. Particle transport was accomplished by tracking spectral wind shear effects on falling particles through a layered (12 spectral levels) atmosphere. These wind shear effects produced accurate particle transport predictions compared to measured data.

Direct Course Analysis

Aircraft in-situ dust cloud measurements from a 26 Oct 83 high explosive (HE) detonation was used to validate a spectral wind transport model. Initial particle-size distributions for the initial stabilized cloud was derived from average optical imaging channel ranges, and applied to the fallout model as an initial condition. Other initial conditions required as inputs into the prediction model were derived from measured Direct Course experimental data. Computed spatial distributions predicted mass histograms measured by mass spectrometers mounted on an aircraft flying through the HE generated dust cloud centers (for various times and altitudes). Mass predictions for the first few aircraft passes resulted in an underprediction of masses across the particle spectrum. These differences in predictions were accounted for by noting that measured distributions consisted of a mixture of soil distributed particles along with pseudo masses of fiberglass strands and chaff remnants generated from bomb debris. Due to faster pseudo mass fallout rates (relative to slower model mass fallout rates), passes later in time displayed better comparisons of the mass histograms.

Cloud center location predictions were computed and agreed with measured results. North components of the predicted cloud centroid were less accurate than west components because larger errors occur in the spectral coefficient generator model when slower input speeds are used (i.e., slow southerly speeds were 1 m/sec or less). Larger transport errors in the first few passes were due to boundary layer effects. The spectral coefficient generator model does not account for boundary layer modeling, and thus is limited in the ability to predict low level transport.

Recommendations

1. In order to simulate forecasted free field environments resulting from nuclear dust-laden threat scenarios, typical most probable month/day global gridded winds must be obtained. These "Winds of War" are required as input into the spectral coefficient

generator model, used to predict spectral coefficients. Archiving these spectral coefficients would allow the capability of predicting free field environments that could aid in fleet survivability predictions due to post nuclear dust threat environments.

2. A nuclear fallout validation using the spectral wind fallout model would enhance the understanding of nuclear cloud parameters used as initial conditions in fallout models (provided the winds are accurately derived).

3. A multiburst dust validation to a high explosive test (Misers Bluff II) would provide insight into multiburst cloud merging required in predicting dust threat scenarios.

4. Develop a particle agglomeration transfer function that would account for the mechanics of particle aggregation.

5. Incorporate boundary layer modeling (subroutines from NMC) into the spectral coefficient generator model.

APPENDIX A

AFGL Model

Air Force Geophysics Laboratory provided ASD/ENSSS (Nuclear Survivability Group) with the software to generate spectral coefficients from a set of global, gridded wind vector components. Dr. Ken Yang and Dr. Ken Mitchell extracted relevant subroutines from the AF Geophysics Laboratory global circulation model, and they explained how to use the software. These subroutines were linked together, creating a program named AFGL. AFGL runs on the CYBER 6600 and creates a set of spectral coefficients using 2.5° gridded wind data as input.

AFGL calls four subroutines in the main program to yield spectral coefficients of the winds. The program uses regular global gridded winds arranged as U (west to east), followed by V (south to north) components of the atmospheric wind vectors, for 12 successively increasing altitudes (decreasing pressures in millibars), for a fixed date and time. Thus the four main subroutines in AFGL are called a total of 24 times for a given date and time.

GAUSS (Called from MAIN) -

Establishes the number, K, of Gaussian latitudes used for the Gaussian grid scheme (Fig. II-3). These are chosen such that they are symmetric about the equator. K=36 for this case and passes this through a call to GAUSLAT.

GAUSLAT (Called from GAUSS) -

Computes the iterated Gauss-Legendre (G-L) roots μ_k (for $k=1,2,\dots,K$), of Eq. (2.19) and the corresponding G-L weights GW_k of Eq. (2.20). The computational stability criterion in using the recurrence Eq. (2.9) requires that (2.9) is stable if its coefficients are less than unity and change signs (3). Thus, when this

computational stability criterion is met (via subroutine POLY), the Gaussian colatitude θ_k (in radians) is increased and iterated upon until divergence between two consecutive computations becomes less than the permissible error $EPS=10^{-12}$ (3). At this point, the iteration is complete and yields the Gaussian colatitude θ_k (in radians) and the corresponding G-L weight GW_k . This process is repeated for each Gaussian colatitude θ_k until all G-L roots μ_k for $k=1, \dots, K$ are found (written to TAPE1).

POLY (Called from GAUSLAT) -

Calculates the ordinary Legendre polynomials of degree $n=q=72$ evaluated at the μ_k roots of Eq. (2.19).

LINTER1 (Called from the MAIN) -

Uses TAPE1 to compute the round-off error, $D(J)$, due to the computer cosine function. The error $D(J)$ is generated when Gaussian colatitudes (in radians) are converted to degrees in order to interpolate the 2.5° gridded wind data to the Gaussian angles (in radians). $D(J)$ is found by taking the difference of the cosine (in radians) of the original Gaussian angle and the cosine of the radian-to-degree then degree-to-radian conversion of the original Gaussian angle. These values are used in subroutine LINTER2 to interpolate the input gridded wind data to a latitude-longitude Gaussian grid (written to TAPE2).

LINTER2 (Called from the MAIN) -

The input to LINTER2 is read from TAPE71 as binary gridded wind data. TAPE71 contains regular global gridded wind data for 73 latitude circles starting at the north pole. Each circle contains 144 entries, starting at the prime meridian and proceeding eastward. LINTER2 interpolates the global gridded wind data to the Gaussian colatitude angles (from TAPE2) onto a two dimensional latitude-longitude

Gaussian grid of 2.5 degrees by 2.5 degrees. These values are stored in a two dimensional array $G(I,J)$, and are used in Eq. (2.28) (written to TAPE3).

SPRMNCS (Called from the MAIN) -

This is the spherical harmonic subroutine which uses the interpolated gridded data of TAPE3 (for a given Gaussian angle) and transforms it to Fourier space in order to compute the Fourier coefficients given by Eq. (2.28) (via subroutine FFT1). It then generates the normalized associated Legendre coefficients at each Gaussian angle (via subroutine LEGEND). At this point, SPRMNCS transforms the Fourier space to Legendre space via G-L quadrature (by subroutine GQL) to yield the spectral coefficients given by Eq. (2.21) (written on TAPE72).

EPSILON (Called in SPRMNCS) -

Calculates the output parameter EPS (denoted ϵ_n^m in Eq. (2.9a)) of degree n and order m of the normalized associated Legendre polynomials in the recursion relation (2.9a). EPS is used in subroutine LEGEND to evaluate Eq. (2.9a). The maximum degree and order of Eq. (2.9) is given by IMAX and JMAX of Eq. (2.13a), where IMAX is one plus the largest zonal wave number (i.e., IMAX=31) and JMAX is one plus the largest difference between the degree and order of the Legendre functions (i.e., JMAX=31).

CFFTI (Called in SPRMNCS) -

Before computing the Fourier transform, N , the length sequence to be transformed (i.e., 144 longitudinal points) must be decomposed into its prime factors. Subroutine CFFTI initializes the array WSAVE which is used in both CFFTF and CFFTB. The prime factorization of N together with a tabulation of the trigonometric functions are computed and stored in WSAVE. The output parameter WSAVE is a work array which must be dimensioned at least $4*N+15$. The same work array can be used for both CFFTF and CFFTB as long as N remains

unchanged. Different WSAVE arrays are required for different values of N. The contents of WSAVE must not be changed between calls of CFFTF and CFFTB.

FFT1 (Called in SPRMNCs) -

This subroutine performs the forward and backward FFT's. When flagged with IDIR = -1, FFT1 does the physical to Fourier transform given by Eq. (2.28) and yields 73 Fourier complex coefficient pairs. When flagged with IDIR = 1, FFT1 does the Fourier to physical transform given by Eq. (2.26) and yields 144 truncated input values. For this case, the complex conjugates must be created for input into CFFTB.

CFFTF (Called in FFT1) -

This is the complex forward FFT given by Eq. (B.1) and it computes the forward complex discrete Fourier transform (the Fourier analysis). Equivalently, CFFTF computes the Fourier coefficients of a complex periodic sequence. CFFTF returns the complex Fourier coefficients to FFT1 where these values are normalized and stored in an array.

CFFTF1 (Called in CFFTF) -

This subroutine calls mixed radix FFT's that correspond to the number and values of the prime factors of N. These algorithms, denoted by PASSF2, PASSF3, PASSF4 and PASSF5, correspond to the decomposition of a complex Fourier transform of radix p equal to 2, 3, 4 and 5 respectively. PASSF is a general mixed radix FFT for primes > 5. CFFTF1 uses the gridded input data passed from FFT1 along with $N=3^2 \cdot 4^2$ corresponding to calling the mixed radix FFT's PASSF3 and PASSF4 (each twice) to yield the computations of Eq. (B.1).

CFFTB (Called in FFT1) -

This is the complex backward FFT given by Eq. (B.2) and it computes the backward complex discrete Fourier transform (the Fourier synthesis).

Equivalently, CFFTB computes a complex periodic sequence from its Fourier coefficients. CFFTB returns the complex values to FFT1 where the real values are stored into an array as truncated input.

CFFTB1 -

This subroutine does exactly what CFFTF1 does but uses Fourier coefficients (passed from FFT1) instead of gridded data.

LEGEND (Called in SPRMNCS) -

LEGEND uses EPS from EPSILON along with JMAX and IMAX (defined in EPSILON) evaluated at a given Gaussian angle (36 in all) to yield ALEG, the normalized associated Legendre polynomial given by Eq. (2.9).

GQL (Called in SPRMNCS) -

This subroutine uses 36 G-L weights (symmetric about the equator) along with the Fourier complex coefficients, to perform the G-L quadrature of Eq. (2.21).

FM(MM,1) and FM(MM,2) are the Fourier complex coefficients for all m in the northern and southern hemispheres respectively. The symmetric and antisymmetric portions of the G-L quadrature accumulates contributions of the even and odd parity values of the Fourier complex coefficients over 36 Gaussian angles. The quantity $FM(MM,1)+FM(MM,2)$ is the sum of the even parity contributions weighted by a factor of 2. The factor of 2 comes from the fact that the 36 G-L weights are weights in the northern hemisphere, which are symmetric about the equator. Thus, multiplying the even parity functions by a factor of 2 yields the full global contributions to the spectral coefficients for the symmetrical portion of the quadrature. Similarly, the quantity $FM(MM,1)-FM(MM,2)$ is twice the sum of the odd parity contributions to the spectral coefficients for the antisymmetrical portion of the G-L quadrature of Eq. (2.21). MS is the maximum zonal wave number m_{max} , given in chapter 3. GQL is called 36 times, corresponding to the 36

Gaussian colatitudes and yields the global spectral complex coefficients (written to TAPE72).

At this point, AFGL is complete. An additional subroutine LEGSUM and additional calls to LEGEND and FFT1 (backward transform) perform a Legendre synthesis on the vorticity and divergence fields. This synthesis does not enter into the calculations of Eq. (2.21) and thus is not used.

APPENDIX B

Fast Fourier Transforms

The Fast Fourier Transform is a method of computing the finite complex Fourier transform (33).

$$\alpha_k = \frac{1}{N} \sum_{j=0}^{N-1} X_j \exp(-i 2\pi j k/N) \quad \text{for } k=0,1,\dots,N-1 \quad (2.22)$$

or the inverse transform

$$X_j = \sum_{k=0}^{N-1} \alpha_k \exp(i2\pi jk/N) \quad \text{for } j=0,1,\dots,N-1 \quad (2.23)$$

where α and X are complex-valued discrete Fourier Transform pairs

The key idea of the method, that of factoring N as n_1, n_2, \dots, n_m , then decomposing the transform into N/n_j transforms of size n_j for $j=1, 2, \dots, m$, was first proposed in 1942 by Damuelson and Lanczos (9). Since the labor of computing a single transform of dimension N is of the order N^2 , the decomposition gives a considerable savings when N is a prime, reducing computing to the order of $N(n_1+n_2+\dots+n_m)$.

A complex multiplication, requiring four real multiplications and two real additions, is a relatively slow operation on most computers (34). To a first approximation, the speed of an FFT algorithm is proportional to the number of complex multiplications used.

For N a power of 2, the Fourier transform of dimension 2 or 4 can be computed without multiplication, and that of dimension 8 requires only two real multiplications,

equivalent to one-half a complex multiplication. A transform of dimension 16, computed as two factors of 4, requires the equivalent of six complex multiplications. Combining these results and assuming that $N = 2^m$ is a power of the radix, the total (approximate) number of complex multiplications is as follows (34):

Radix	Number of Complex Multiplications
2	$mN/2 - (N-1)$
4	$3mN/8 - (N-1)$
8	$mN/3 - (N-1)$
16	$21mN/64 - (N-1)$

The savings for 16 over 8 is small, considering the complexity of the algorithm. Radix 8, with provision for an additional factor 4 or 2, is a good choice for an efficient FFT program for powers of 2. For the mixed radix FFT, transforms with factors of 4 are desired whenever possible, but also provide for factors of 2.

Consider the number of complex multiplications for a radix- p transform of $N = p^m$ complex data values, where p is an odd prime. While at first it might appear that an elementary transform of dimension p required $(p-1)^2$ complex multiplications, it can be shown (34) that $(p-1)^2$ real multiplications suffice, equivalent to $(p-1)^2/4$ complex multiplications. This result holds, in fact, for any odd value of p . Thus the transform steps for $N = p^m$ require the equivalent of (34)

$$\frac{mN (p-1)^2}{4p}$$

complex multiplications for a radix- p transform.

Using these transform methods, transforms from spectral space to grid space, and inverse transforms from grid space back to spectral space may be applied for faster, more efficient computations than evaluating the vector-coupled sums directly in spectral form.

APPENDIX C

Mass Fraction Distribution of Characteristic Soil for Direct Course High Explosive Dust Cloud

In order to conduct numerical predictions of dust clouds, an initial particle-size, mass-size, number size or other "quantity-size" distribution must be chosen as an initial condition for modeling particle transport. For the Direct Course validation, a mass-size distribution was required to make the comparison of predicted mass-size histograms to aircraft measured data. Chris Zimmerman from ASD/ENSSS computed an eighth order polynomial curve fit to the mass fraction per micrometer of diameter associated with characteristic dust particles of a given size diameter for the White Sands Missile Range test site soil. The curve fit is based on data extracted from an Air Force Weapons Laboratory Technical Report (22) which evaluated soil characteristics of White Sands Missile Range. The results are summarized in Table C-1, and the polynomial coefficients along with a plot showing the polynomial curve fit to (square) data points are given in Fig. C-1.

The procedure to compute Table C-1 and Figure C-1 begins by first computing averages of the percentage of mass passing through various sieve sizes as given in Table 4, p. 20-24 of reference (22). These average mass percentages appear in column four of Table C-1.

Next, diameter ranges associated with each sieve diameter are found. The midpoint between two adjacent sieve diameters is used as the break point. Thus for sieve diameters of 4.76, 2.0 and 0.84 millimeters (mm), the diameter $3.38=(4.76+2.0)/2$ and diameter $1.42=(2.0+0.84)/2$ are used as break points. The diameter range, $\Delta d(d)$, associated with the 2.0 millimeter sieve size is found such that $\Delta d(d)=3.38-1.42=1.96$ mm. Diameter ranges are given in column three of Table C-1. Mass fractions, $\Delta M(d)$, associated with

each sieve size are computed in a manner similar to the diameter range. These values are shown in column five of Table C-1. Mass fractions per micrometer are derived from columns five and three and are given in column six of Table C-1.

The last step is to plot natural logarithms of column six against column two of Table C-1. An eighth order polynomial curve fit to the data is made and shown as the curve in Figure C-1. The fit uses coefficients numerically derived from Fig. C-1 and associates mass fraction per micrometer of particle diameter for a given particle diameter d . Eq. (4.5) yields the results of this relation as

$$\begin{aligned} \ln(\Delta M(d) / \Delta d) = & -2.7973914 - 3.3879049 x + 6.1365564 x^2 - 5.5195742 x^3 \\ & + 2.3597698 x^4 - 5.333146 x^5 + .0655594 x^6 \\ & - .0041489 x^7 + .0001059 x^8 \end{aligned} \quad (C.1)$$

where $x = \ln(d)$

d = particle diameter (micrometers)

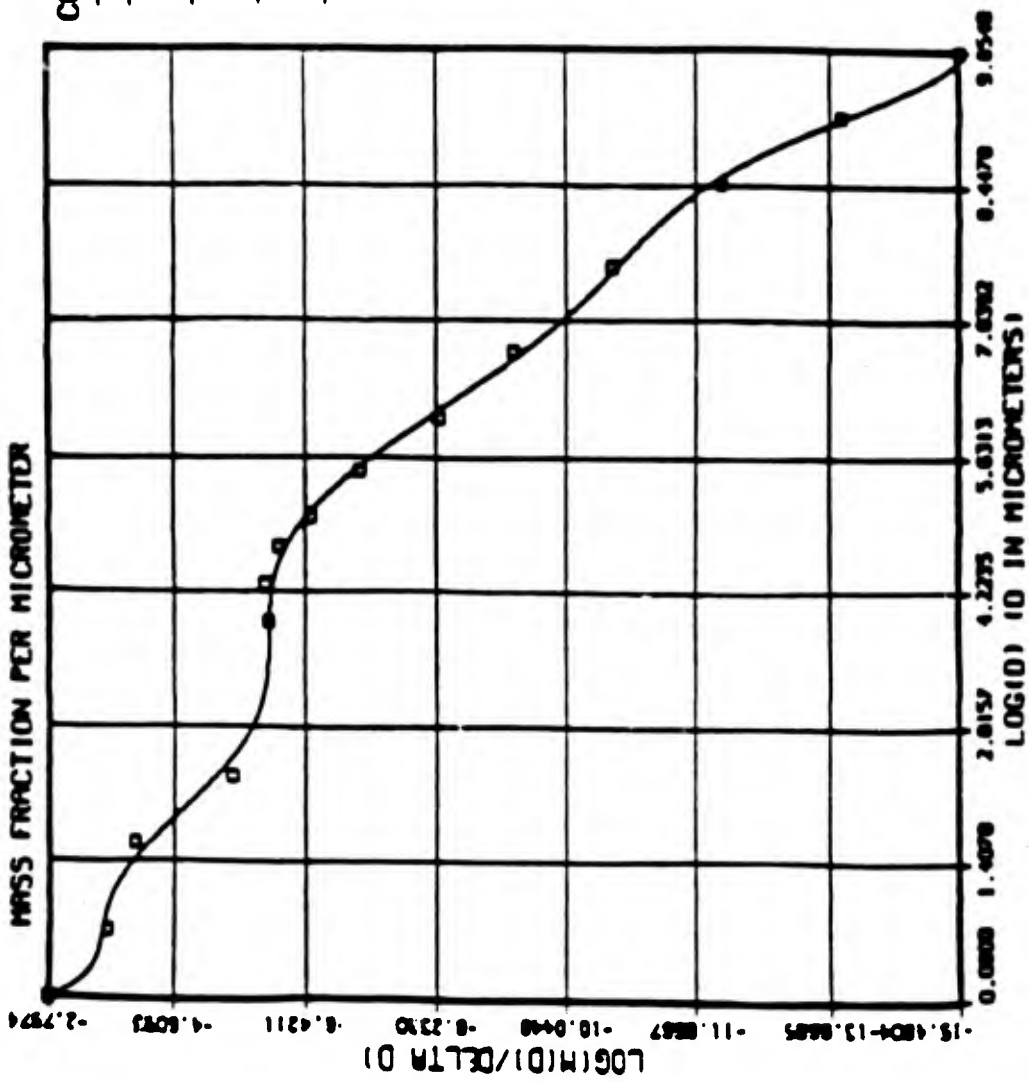
$\Delta M(d) / \Delta d$ = mass fraction per micron

Column two of Table C-1 shows that all particles are less than 20,000 microns in diameter. Therefore, the mass fraction per micrometer of diameter integrated over the full particle range should yield a normalization of one. Then,

$$\int_0^{20\text{mm}} [\Delta M(d)/\Delta d] dx = 1 \quad (C.2)$$

Numerical integration of Eq. (C.2) uses a trapezoidal method having 10 micron discrete intervals. Computed exponential mass fractions per micrometer of diameter are derived from Eq. (C.1) and used in the numerical integration. This integration yields a normalization of 1.01 and is considered satisfactory for use in the computation of Direct

Course mass histograms.



COEFFICIENTS
 -2.7973914 $\times 10^0$
 -3.3879049 $\times 10^0$
 6.1365564 $\times 10^0$
 -5.5195742 $\times 10^0$
 2.3597698 $\times 10^{-1}$
 -5.3331457 $\times 10^{-2}$
 6.5559436 $\times 10^{-3}$
 -4.1489321 $\times 10^{-4}$
 1.0590973 $\times 10^{-4}$

Figure C-1

Table C-1. Direct Course Mass Fraction Distribution

Sieve Size	Sieve Diameter d (microns)	Diameter Range at d, $\Delta d(d)$	Percent Mass* Passed	Fraction at d $\Delta M(d)$	$\frac{\Delta M(d)}{\Delta d(d)}$
3/4	19050.0	10.71E3	100.0	.002	1.867E-7
3/8	9530.0	7.14E3	99.6	.007	9.804E-7
#4	4760.0	3.77E3	98.7	.019	5.039E-6
#10	2000.0	1.96E3	95.94	.044	2.24E-5
#20	840.0	790.0	89.8	.072	9.114E-5
#40	420.0	300.0	81.58	.077	2.567E-4
#60	240.0	130.0	74.36	.101	7.769E-4
#100	150.0	70.0	61.5	.106	1.514E-3
#140	110.0	40.0	53.12	.093	2.325E-3
#200	74.0	28.0	42.94	.079	2.821E-3
0.05	50.0	32.0	37.2	.086	2.689E-3
0.01	10.0	22.5	25.74	.100	4.444E-3
0.005	5.0	4.0	17.32	.070	.0175
0.002	2.0	2.0	11.7	.052	.026
0.001	1.0	1.5	6.98	.093	.062

*Based on average of those given in Table 4, p. 20-24 of AFWL-TR-83-97

APPENDIX D

Users' Guide for AFGL

From Appendix A, the input to AFGL has been described. TAPE71 is the input tape and contains global gridded wind data for 73 latitude circles, each circle containing 144 longitude points (for 12 pressure level sets).

Typically, these points have units of knots, but meters/second, miles/hour, etc. can be used in AFGL. Conversions to desired units must be accomplished before inputting AFGL.

After the desired units have been converted (if necessary), the 12 sets of binary gridded winds must be in a local file called TAPE71 in order to run AFGL on the Cyber.

Once TAPE71 and AFGL are local files, the following control directives are required to run AFGL:

```
FTN,I=AFGL,L=0,OPT=2
```

The Cyber takes approximately 16 CP seconds to compile. Once it has compiled, type

```
LDSET,PRESET=ZERO
```

```
LGO
```

The run time for the set of directives is approximately 65 CP seconds and outputs the spectral coefficients to TAPE72 as a local file.

Bibliography

1. Baer, Ferdinand and G.W. Platzman. "A Procedure for Numerical Integration of the Spectral Vorticity Equation," Journal of Meteorology, 18 (3):393-401 (June 1961).
2. Baer, F. and F.N. Alyea. "Effects of Spectral Truncation on General Circulation and Long Range Prediction," Journal of Atmospheric Sciences, 28 (4):457-480 (May 1971).
3. Belousov, S.L. Tables of Normalized Associated Legendre Polynomials. Pergamon Press, New York, 1962.
4. Bolin, B. "An Improved Barotropic Model and Some Aspects of Using the Balance Equation for Three-Dimensional Flow," Tellus, 8 (1):61-75 (February 1956).
5. Bourke, W. "A Multi-Level Spectral Model. I. Formulation and Hemispheric Integrations," Monthly Weather Review, 102: 687-701 (October 1974).
6. Bourke, W., Bryant McAvaney, Kamal Puri and Robert Thurling. "Global Modeling of Atmospheric Flow by Spectral Methods," Methods in Computational Physics, 17. Academic Press 1977.
7. Bridgman, Charles J. and Winfield S. Bigelow. "A New Fallout Prediction Model," Health Physics, 43 (2): 205-218 (August 1982).
8. Cressman, G.P. "Barotropic Divergence and Very Long Atmospheric Waves," Monthly Weather Review, 86 (8): 293-297 (August 1958).
9. Danielson, G.C. and C. Lanczos. "Some Improvements in Practical Fourier Analysis and Their Application to X-Ray Scattering from Liquids," Journal of Franklin Institute, 233: 365-380 and 435-452 (April 1942).
10. Davies, C.N. "Definitive Equations for the Fluid Resistance of Spheres," Proceedings of the Physical Society of London, 57: 259-276 (July 1945).
11. Eliassen, E., B. Machenhauer and E. Rasmussen. On a Numerical Method for Integration of the Hydrodynamical Equation with a Spectral Representation of the Horizontal Fields. Copenhagen University, Institute for Theoretical Meteorology. Report Number 2. Copenhagen, Denmark, 1970.
12. Ellsaesser, Hugh W. "Expansion of Hemispheric Meteorological Data in Antisymmetric Surface Spherical Harmonic (Laplace) Series," Journal of Applied Meteorology, 3: 263-276 (June 1966).
13. Flattery, Thomas W. Major USAF. Spectral Models for Global Analysis and Forecasting, Paper Included in "Automated Weather Support, Proceedings of Sixth AWS Technical Exchange Conference," AWS Technical Report 292, U.S. Naval Academy, Annapolis, MD (April 1971).

14. Glasstone, Samuel and Philip J. Dolan. The Effects of Nuclear Weapons. Third Edition. Washington D.C.: U.S. Government Printing Office, 1977.
15. Haltner, George J. and R.J. Williams. Numerical Prediction and Dynamic Meteorology. Second Edition. John Wiley and Sons, 1980.
16. Hopkins, Arthur T. A Two Step Method to Treat Variable Winds in Fallout Smearing Codes, NTIS Doc. AD 115514, M.S. Thesis, Sch. Eng., Air Force Institute of Technology, Wright-Patterson AFB, OH, 1982.
17. Hopkins, Arthur T. Development and Validation of a New Fallout Transport Method Using Variable Spectral Winds, NTIS Doc. AD A151871, Ph.D. Dissertation, Sch. Eng., Air Force Institute of Technology, Wright-Patterson AFB, OH, 1984.
18. Hopkins, Arthur T. Unpublished Fallout Model developed while assigned to ASD/ENSSS, Wright-Patterson AFB, OH, July 1985.
19. Knollenberg, John D. and Robert G. Knollenberg. Results of the Direct Course Aircraft In-Situ Sampling of the HE Dust Cloud. DNA 001-83-C-0282. Defense Nuclear Agency, Washington, D.C., 1984.
20. McDonald, J.E. "An Aid to Computation of Terminal Fall Velocities of Spheres," Journal of Meteorology, 17: 463-465 (August 1960).
21. Meriless, P.E. "The Equations of Motion in Spectral Form," Journal of Atmospheric Sciences, 25: 736-743 (September 1968).
22. Miller, Edward L. and Robert J. Majka. Soil Characterization and Evaluation at White Sands Missile Range, New Mexico, NTIS Doc. AD-A134820, Air Force Weapons Laboratory, 1983.
23. National Oceanic and Atmospheric Administration. U.S. Standard Atmosphere, 1976. National Aeronautics and Space Administration and U.S. Air Force, Washington, D.C., 1976.
24. Norment, Hillyer G. DELFI: Department of Defense Fallout Prediction System, Volume I-Fundamentals, NTIS Doc. ADA088367, Defense Nuclear Agency, Washington, D.C., 1979.
25. Orszag, Steven A. "Transform Method for the Calculation of Vector-Coupled Sums: Application to the Spectral Form of the Vorticity Equation," Journal of the Atmospheric Sciences, 27: 890-895 (September 1970).
26. Pugh, George E. and R. J. Galliano. An Analytic Model of Close-In Deposition of Fallout for Use in Operational Type Studies, NTIS Doc. AD 261752, Weapon Systems Evaluation Group Memorandum RM10. Washington, D.C., 1959.
27. Robert, André J. "The Integration of a Low Order Spectral of the Primitive Meteorological Equations," Journal of the Meteorological Society of Japan, Tokyo, 44 (5): 237-245 (October 1966).

28. Robert, André J. "Integration of a Spectral Barotropic Model from Global 500-MB Charts," Monthly Weather Review, 96 (2): 83-85 (February 1969).
29. Schneider, Bruce and Raymond Mondragon. Fabrication and Construction of Support Structure for Direct Course, NTIS Doc. AD-AD-B091325, Defense Nuclear Agency, Washington, D.C., 1984.
30. Schneider, David P. Determination of Lateral Spread of Nuclear Fallout Patterns, AFIT/GNE/PH/86M-12, M.S. Thesis, Sch. Eng., Air Force Institute of Technology, Wright-Patterson AFB, OH, 1986.
31. Sela, Joseph G. "Spectral Modeling at the National Meteorological Center," Monthly Review, 108 (9): 1279-1292 (September 1980).
32. Sela, Joseph G. The NMC Spectral Model. NOAA Technical Report NWS 30, U.S. Department of Commerce, National Oceanic and Atmospheric Administration, National Weather Service, Silver Springs, MD (May 1982).
33. Singleton, Richard C. "A Method for Computing the Fast Fourier Transform with Auxiliary Memory and Limited High-Speed Storage," IEEE Transactions on Audio and Electroacoustics, AV-15 (2): 91-97 (June 1967).
34. Singleton, Richard C. "An Algorithm for Computing the Mixed Radix Fast Fourier Transform," IEEE Transactions on Audio and Electroacoustics, AV-17 (2): 93-103 (June 1969).

VITA

Darrell Palmer was born [REDACTED]. He completed high school in [REDACTED] and entered Ohio State University. In [REDACTED] he enlisted in the Air Force and spent three years at Clark AB, Philippines, working electronic warfare on the F-4 Phantom. In [REDACTED], he began the Nuclear Engineering program at Texas A & M under AECP and graduated [REDACTED] with a B.S. in Nuclear Engineering. After OTS commissioning, he arrived at Wright-Patterson AFB where he has been working nuclear survivability. [REDACTED] he began taking nuclear engineering courses part-time at AFIT.

Permanent Address: [REDACTED]
[REDACTED]

UNCLASSIFIED

SECURITY CLASSIFICATION OF THIS PAGE

A177654

REPORT DOCUMENTATION PAGE

1a. REPORT SECURITY CLASSIFICATION UNCLASSIFIED		1b. RESTRICTIVE MARKINGS	
2a. SECURITY CLASSIFICATION AUTHORITY		3. DISTRIBUTION/AVAILABILITY OF REPORT Approved for public release; distribution unlimited	
2b. DECLASSIFICATION/DOWNGRADING SCHEDULE		5. MONITORING ORGANIZATION REPORT NUMBER(S)	
4. PERFORMING ORGANIZATION REPORT NUMBER(S) AFIT/GNE/ENP/86M-14		7a. NAME OF MONITORING ORGANIZATION	
6a. NAME OF PERFORMING ORGANIZATION School of Engineering	6b. OFFICE SYMBOL (If applicable) AFIT/ENP	7b. ADDRESS (City, State and ZIP Code)	
6c. ADDRESS (City, State and ZIP Code) Air Force Institute of Technology Wright-Patterson AFB, Ohio 45433		9. PROCUREMENT INSTRUMENT IDENTIFICATION NUMBER	
8a. NAME OF FUNDING/SPONSORING ORGANIZATION	8b. OFFICE SYMBOL (If applicable)	10. SOURCE OF FUNDING NOS.	
8c. ADDRESS (City, State and ZIP Code)		PROGRAM ELEMENT NO.	PROJECT NO.
11. TITLE (Include Security Classification) See box 19		TASK NO.	WORK UNIT NO.
12. PERSONAL AUTHOR(S) Palmer, Darrell Lee Lt USAF			
13a. TYPE OF REPORT MS Thesis	13b. TIME COVERED FROM _____ TO _____	14. DATE OF REPORT (Yr., Mo., Day) 1986 September	15. PAGE COUNT 127
16. SUPPLEMENTARY NOTATION			
17. COSATI CODES		18. SUBJECT TERMS (Continue on reverse if necessary and identify by block number)	
FIELD	GROUP	SUB. GR.	Fallout, Spectral Methods, Direct Course, Spatial distribution
18	08		
19. ABSTRACT (Continue on reverse if necessary and identify by block number)			
Title: SPECTRAL METHODS FOR GLOBAL ATMOSPHERIC FLOW APPLIED TO THE MODIFIED AFIT FALLOUT PREDICTION MODEL			
Thesis Chairman: Charles J. Bridgman			
Approved for public release: IAW AFR 190-17. Lynn E. WOLAVER 8 Dec 86 Down for Research and Professional Development, Air Force Institute of Technology (AFIT), Wright-Patterson AFB OH 45433			
20. DISTRIBUTION/AVAILABILITY OF ABSTRACT UNCLASSIFIED/UNLIMITED <input checked="" type="checkbox"/> SAME AS RPT. <input type="checkbox"/> DTIC USERS <input type="checkbox"/>		21. ABSTRACT SECURITY CLASSIFICATION UNCLASSIFIED	
22a. NAME OF RESPONSIBLE INDIVIDUAL Charles J. Bridgman		22b. TELEPHONE NUMBER (Include Area Code) (513) 255-4498	22c. OFFICE SYMBOL AFIT/ENP

1
thesis

This investigation predicted the airborne spatial distribution of a high explosive generated dust cloud. A comparison of predicted cloud center positions to experimental data collected from an aircraft flying through the dust cloud center at various times and altitudes was also studied.

The analysis was accomplished using a model received from the Air Force Geophysics Laboratory (model called AFGL) which produces global complex spectral coefficients. Spectral coefficients were applied as inputs into a modified AFIT fallout prediction model (called REDRAM) to predict dust mass/m³ of air per μ m of dust diameter which resulted from a single continuous horizontal pass through the cloud at a fixed time and altitude. The results validated the spectral wind fallout model by showing general agreement of predicted values to that of experimental results. The significance of the validation shows that spectral methods can realistically predict particle transport using a spectral wind fallout model.

↑